UNIVERSITÄT
BAYREUTH

Synthesis & characterization of narrowly dispersed colloidal objects: bridging polymeric to inorganic materials with distinct optical properties

Dissertation

zur Erlangung des akademischen Grades einer
Doktorin der Naturwissenschaften
Dr. rer. nat.

an der
Universität Bayreuth
Fakultät für Biologie, Chemie & Geowissenschaften

vorgelegt von
Tanja Feller
geboren in Hof (Saale)

Bayreuth 2023

Die vorliegende Arbeit wurde in der Zeit von Dezember 2017 bis September 2022 in Bayreuth am Lehrstuhl Physikalische Chemie I unter der Betreuung von Herrn Professor Dr. Markus Retsch angefertigt.

Vollständiger Abdruck der von der Fakultät für Biologie, Chemie und Geowissenschaften der Universität Bayreuth genehmigten Dissertation zu Erlangung des akademischen Grades einer Doktorin der Naturwissenschaften (Dr. rer. nat.).

Dissertation eingereicht am: 20.02.2023

Zulassung durch die Promotionskommission: 08.03.2023

Wissenschaftliches Kolloquium: 19.07.2023

Amtierender Dekan: Prof. Dr. Benedikt Westermann

Prüfungsausschuss:

Prof. Dr. Markus Retsch (Gutachter)
Prof. Dr. Seema Agarwal (Gutachter)
Prof. Dr. Anna Schenk (Vorsitz)
Prof. Dr. Josef Breu

Die vorliegende Arbeit ist als Monographie verfasst.

Teile der Arbeit sind bereits in folgender Publikation erschienen:

Tanja Feller, Sabine Rosenfeldt, Markus Retsch, „Carbothermal synthesis of micron-sized, uniform, spherical silicon carbide (SiC) particles", *Zeitschrift für anorganische und allgemeine Chemie*, doi: 10.1002/zaac.202100209, **2021**.

Diese Publikation ist als Quelle[1] angegeben.

Teile der Arbeit werden veröffentlicht werden:

Dominik Benke, **Tanja Feller**, Marcel Krüsmann, Anna Lechner, Friederike Ganster, Matthias Karg, Markus Retsch, „Prolate spheroidal polystyrene nanoparticles: matrix assisted synthesis, interface properties, and scattering analysis", *eingereicht bei Soft Matter*.

Zusätzliche Publikationen, die nicht in dieser Arbeit enthalten sind:

1. Anna M. Lechner, **Tanja Feller**, Qimeng Song, Bernd A.F. Kopera, Lukas Heindl, Markus Drechsler, Sabine Rosenfeldt, Markus Retsch, „Scalable synthesis of smooth PS@TiO$_2$ core-shell and TiO$_2$ hollow spheres in the (sub) micron size range: understanding synthesis and calcination parameters", *Colloid and Polymer Science*, doi: 10.1007/s00396-020-04626-3, **2020**.

2. Marius Schöttle, Thomas Tran, **Tanja Feller**, Markus Retsch, „Time-temperature integrating optical sensors based on gradient colloidal crystals", *Advanced Materials*, doi: 10.1002/adma.202101948, **2021**.

Für meine Familie.

Abbreviations

a.u.	Arbitrary units
AA	Acrylic acid
AIBA	2,2-Azobis-(2-methyl-propionamidin)-dihydrochlorid
AIBN	2,2-Azobis(2-methylpropionitrile)
ATR-FTIR	Attenuated total reflection Fourier transform infrared spectroscopy
BSE	Backscattered electrons
c	Concentration
cm	Centimeter
c_p	Specific heat capacity
D	Diameter
DLS	Dynamic light scattering
EAF4	Electrical asymmetrical flow field flow fractionation
EDS	Energy dispersive X-ray spectroscopy
EtOH	Ethanol
FFF	Field flow fractionation
g	Gram
h	Hour
HCl	Hydrochloric acid
IR	Infrared
J	Joule
K	Kelvin
KCl	Potassium chloride

KPS	Potassium persulfate
L	Liter
min	Minute
mL	Milliliter
mm	Millimeter
MMA	Methyl methacrylate
mol	Mole
MTC	[2-(Methacryloyloxy)ethyl]trimethylammonium chloride
N	Newton
NaOH	Sodium hydroxide
NaSS	3-styrenesulfonic acid sodium salt hydrate
NH$_3$	Ammonia
nm	Nanometer
PDMS	Poly(dimethylsiloxane)
PMMA	Poly(methyl methacrylate)
PNIPAM	Poly(*N*-isopropylacrylamide)
PS	Polystyrene
PSS	Polystyrene sulfonate
PTMS	Phenyltrimethoxysilane
PVA	Poly(vinyl alcohol)
PVP	Polyvinylpyrrolidone
rcf	Relative centrifugal force
RI	Refractive index
rpm	Revolutions per minute
SAXS	Small angle X-ray scattering
SE	Secondary electrons

SEM	Scanning electron microscopy
SiC	Silicon carbide
Si$_3$N$_4$	Silicon nitride
SiO$_2$	Silicon dioxide
STA	Simultanous thermal analysis
TEM	Transmission electron microscopy
TEOS	Tetraethylorthosilicate
TiO$_2$	Titanium dioxide
UV-Vis	Ultraviolet-visible spectroscopy
V	Volume
W	Watt
WDS	Wavelength dispersive X-ray spectroscopy
XRD	X-ray diffraction

Abstract

Cooling is an essential technology for many domestic and industrial applications. However, conventional cooling technologies require additional external energy input. In contrast, passive radiative daytime cooling provides cooling only by radiative heat exchange with cold outer space. In this technology, an object emits radiation in the earths atmospheric window between 8-13 μm and reflects any other radiation, especially in the solar region. This technique holds great potential for environmentally friendly practical applications in energy-efficient green buildings and smart personal thermal management systems. A wide range of functional materials and sophisticated structures have been demonstrated as thermal radiators. Although some materials are well discussed and theoretically investigated, further improvements are needed to allow for scalable and more efficient material concepts.

The scope of this thesis is the preparation and characterization of polymer particle building blocks and micro-structured dielectric ceramic materials for potential passive cooling applications.

Particles are often used in passive cooling composite materials to enhance scattering and reflection in the solar range. This can be achieved by changing the particle shape and structure or adjusting fundamental material properties. Distinct particle size distributions and the surface charge are paramount for further processing, for example, particle assembly, towards radiative cooling applications. These properties can be analyzed with field flow fractionation (FFF). Besides highly monodisperse poly(methyl methacrylate)/(n-butyl acrylate) spheres, ellipsoidal polystyrene particles with different aspect ratios were investigated by this technique. FFF allowed determining the particle size distribution, which was able to resolve subtle changes in the particle size and revealed particle agglomerates caused by the dispersion processing. Furthermore, the zeta potential of polystyrene/silica core-shell particles was evaluated with FFF and compared with a conventional analysis device. Finally, the stability of hollow silica spheres was visualized by analyzing redispersed particles, which were treated with varying ultrasonication methods. Field flow fractionation is a powerful technique to characterize dispersions owing to its capability to resolve the entire particle distribution function.

The optical properties in the IR region can be tuned by using inorganic dielectric materials, which exhibit strong absorption in the atmospheric window. More precisely, silicon dioxide and silicon carbide have suitable optical properties in the mid-infrared range, which renders them promising materials for ambient temperature thermal emitters.

Bottom-up synthesis routes followed by different calcination methods were used to fabricate silicon carbide particles. The materials were analyzed with optical, chemical, thermal, and spectroscopic methods. Two techniques, the magnesiothermic reduction and the carbothermal reaction were investigated for the conversion from silica to silicon carbide particles. The influence of reaction parameters in the calcination step, like the temperature, the gaseous atmosphere, or the size and composition of the precursor particles, were studied. Particularly, grained mixtures of silica particles with reactant materials (carbon or magnesium), silica-carbon core-shell particles, and silica precursor particles with covalently bonded carbon were synthesized and used for the transformation to silicon carbide. It was found that besides stoichiometry, the main crucial parameters for the successful conversion from silica to silicon carbide with the preservation of the spherical structure of the particles are the interface between silicon and carbon species, and especially the gaseous atmosphere. Both calcination methods favored side reactions when nitrogen was used as inert gas instead of argon. Spectroscopic analysis of the particles themselves and assembled as monolayers on polydimethylsiloxane was conducted and confirmed the potential for radiative cooling applications.

In addition to individual particles, more complex 3D structures out of dielectric ceramic materials can also affect the optical properties. On the one hand, inverse opals are especially interesting due to their periodic mesostructure, which causes a photonic stopband. Polymer particles were assembled into colloidal crystals and infiltrated with liquid preceramic precursors to form inverse opal structures in a hard templating process. Systems based on the same precursors and calcination routes as in the particle section were tested. Amorphous silicon carbide/silica inverse opals were produced with magnesiothermic reduction. It was observed that even with adjustments in the assembly and the heating process, the formation of polycrystalline silicon carbide inverse opals was unsuccessful with the carbothermic reaction. On the other hand, fibers do not have long-range order giving rise to scattering. The fabrication process for fiber-based ceramics with solution blow spinning was briefly outlined and tested with an airbrush and a 3D-printed microchannel setup.

These results show convenient protocols for fabricating SiC particles and inverse structures starting from silica materials in the submicron size range. Both trans-

formation techniques, magnesiothermic and carbothermic, are advantageous for different material structures. This can be used for future works that deal with particle composite materials for radiative cooling applications or as a basis to produce other systems, e.g., fibers, for direct and large-scale processes.

Zusammenfassung

Kühlungstechnologien sind essenziell für viele häusliche und industrielle Anwendungen. Allerdings benötigen konventionelle Kühlungstechnologien eine zusätzliche externe Energieeinspeisung. Im Gegensatz dazu erfolgt die Kühlung mit passiver radiativer Kühlung am Tag nur durch Wärmeaustausch in Form von Strahlung mit dem kalten Weltraum. Hierbei emittiert ein Objekt Strahlung im Atmosphärenfenster der Erde zwischen 8-13 Mikrometer und reflektiert jede andere Strahlung, insbesondere im Bereich des Sonnenlichts. Diese Technik hat großes Potential für umweltfreundliche praktische Anwendungen in energieeffizienten grünen Gebäuden und smarte Wärmemanagementsysteme für Personen. Eine Vielzahl von funktionalen Materialien und komplexen Strukturen wurden schon als thermische Strahler vorgestellt. Obwohl einige Materialien oft erörtert und theoretisch erforscht worden sind, werden zusätzliche Verbesserungen benötigt, um skalierbare und effizientere Materialkonzepte zu ermöglichen.

Die Aufgabenstellung dieser Doktorarbeit ist die Herstellung und Charakterisierung von Polymerpartikeln, die als Bausteine für weitere Strukturen verwendet werden können, und mikrostrukturierten dielektrischen keramischen Materialien für potenzielle Anwendungen in der Passivkühlung.

Partikel werden häufig für die Passivkühlung in Verbundwerkstoffen verwendet, um die Streueigenschaften und die Reflektion im Bereich des Sonnenlichts zu erhöhen. Dies kann durch die Variation der Partikelform und -struktur oder durch Einstellung von grundlegenden Materialeigenschaften erfolgen. Enge Partikelgrößenverteilungen und Oberflächenladungen sind von großer Bedeutung für die Weiterverarbeitung, z.B. bei der Partikelanordnung, für Anwendungen für radiative Kühlung. Diese Eigenschaften können mit der Feld-Fluss-Fraktionierung (FFF) analysiert werden. Neben höchst monodispersen Polymethylmethacrylat/n-butylacrylat Kugeln, wurden auch elliptische Polystyrolpartikel mit unterschiedlichen Aspektverhältnissen mit dieser Methode untersucht. FFF ermöglichte die Bestimmung der Partikelgrößenverteilung, mit der feine Änderungen in der Partikelgröße aufgelöst, und durch die Dispersionsverarbeitung verursachte Partikelagglomerate aufdeckt werden konnten. Zusätzlich wurde das Zeta-Potential von Polystyrol/Silika Kern-Schale

Partikeln mit der FFF bestimmt und mit einem üblichen Analysegerät verglichen. Schließlich wurde die Stabilität von Silika Hohlkugeln durch die Analyse von redispergierten Partikeln, die mit unterschiedlichen Ultraschallmethoden behandelt worden sind, dargestellt. Die Feld-Fluss-Fraktionierung ist eine leistungsstarke Technik zur Charakterisierung von Dispersionen, da sie in der Lage ist, die gesamte Partikelverteilungsfunktion aufzulösen.

Die optischen Eigenschaften im IR-Bereich können durch die Verwendung von anorganischen, dielektrischen Materialien, die eine starke Absorption im Atmosphärenfenster aufweisen, angepasst werden. Genauer gesagt Siliziumdioxid und Siliziumkarbid besitzen geeignete optische Eigenschaften im mittleren IR-Bereich, was sie zu aussichtsreichen Materialien als thermische Emitter bei Umgebungstemperaturen macht.

„Botttom-up" Syntheserouten mit anschließenden Kalzinierungsmethoden wurden verwendet, um Siliziumkarbidpartikel herzustellen. Die Materialien wurden mit optischen, chemischen, thermischen und spektroskopischen Methoden untersucht. Zwei Methoden, die magnesiothermische Reduktion und eine karbothermische Reaktion, wurden getestet, um Silika- zu SiC-Partikel umzuwandeln. Der Einfluss von verschiedenen Reaktionsparametern im Kalzinierungsschritt, wie die Temperatur, die Gasatmosphäre oder die Größe und Zusammensetzung der Precursorpartikel wurden untersucht. Insbesondere granulierte Mischungen von Silikapartikeln mit den Reaktionspartnern (Kohlenstoff oder Magnesium), Silika-Kohlenstoff Kern-Schale Partikel und Silika Precursorpartikel mit kovalent gebundenem Kohlenstoff wurden hergestellt und für die Umwandlung zu Siliziumkarbid verwendet. Es wurde herausgefunden, dass neben der Stöchiometrie, die Grenzfläche zwischen Silizium und Kohlenstoff und besonders die Gasatmosphäre als kritische Parameter für die erfolgreiche Umwandlung von Silika zu Siliziumkarbid, unter Erhalt der sphärischen Struktur der Partikel, gelten. Bei beiden Kalzinierungstechniken wurden Nebenreaktionen begünstigt, wenn Stickstoff anstelle von Argon als Inertgas verwendet worden ist. Spektroskopische Analysen von den Partikeln selbst und angeordnet als Monolagen auf Polydimethylsiloxan wurden durchgeführt und bestätigten das Potential für die Anwendung als radiativer Kühler.

Zusätzlich zu einzelnen Partikeln, können auch komplexere 3D Strukturen aus dielektrischen, keramischen Materialien die optischen Eigenschaften beeinflussen. Auf der einen Seite sind inverse Opale hierfür besonders interessant, da ihre periodische Mesostruktur die Ausbildung eines photonischen Stopbands bewirkt. Hierfür wurden Polymerpartikel in kolloidalen Kristallen angeordnet und mit flüssigen präkeramischen Grundstoffen infiltriert, um inverse Opale in einem „hard-template"

Prozess herzustellen. Die Systeme mit den gleichen Ausgangsmaterialien und Kalzinierungsrouten, die bereits für die Partikel verwendet worden sind, wurden hier ebenfalls getestet. Mit der magnesiothermischen Reduktion konnten amorphe Siliziumkarbid/Siliziumdioxid inverse Opale hergestellt werden. Bei der Verwendung der carbothermischen Reaktion wurde beobachtet, dass selbst mit Anpassungen im Anordungs- und Heizprozess, die Herstellung von inversen Opalen aus polykristallinen Siliziumkarbid nicht erfolgreich war. Auf der anderen Seite besitzen Faserstrukturen keine weitreichende Ordnung, was zu einer Verstärkung von Streuung führt. Der Herstellungsprozess für faserbasierte Keramiken mit „solution blow spinning" wurde kurz umrissen und mit einer Airbrush Pistole sowie einem 3D gedrucktem Mikrokanal Aufbau getestet.

Insgesamt zeigen diese Ergebnisse geeignete Protokolle für die Herstellung von SiC Partikeln und inversen Opalstrukturen ausgehend von Siliziumdioxid im Größenbereich kleiner als einem Mikrometer. Beide Umwandlungsmethoden, magnesiothermisch und carbothermisch, sind vorteilhaft für jeweils unterschiedliche Materialstrukturen. Diese können für zukünftige Arbeiten, die Komposit Materialien mit Partikeln für radiative Kühlung behandeln oder als eine Basis zum Aufbau von anderen Materialsystemen, wie z.B. Fasern, für direkte und großflächige Anwendungen, verwendet werden.

Contents

Introduction

1

A massive amount of global energy consumption belongs to environmental and industrial thermal management. Due to the urban heat island effect, the temperatures are higher in cities than in the rural countryside. Tall buildings trap the solar radiation and green spaces are often reduced or completely missing. Additionally, the increased use of manmade materials like concrete or glass fronts also plays an essential role in heat production in big cities. This effect can lead to an increased air temperature between 5 °C and 15 °C,[2] which has remarkable consequences for nature and the health of the people living there.

With the additional climate change, the global power consumption to cool down industrial and residential buildings with active air conditioners (AC) will increase further. 20 % of the total electricity usage of buildings is assigned to cooling technologies.[3] Meanwhile, this massive usage of ACs will lead again to more waste heat and CO_2 emissions, creating a harmful circle. Improving the efficiency of established cooling techniques will not be sufficient in relating to environmental changes since the main problems of thermal discharge and the required power input are still not solved. Additionally, most refrigerants in ACs contain chlorofluorocarbons (CFCs) or hydrofluorocarbons (HFCs), which damage the ozone layer or are extremely potent greenhouse gases.[4] Refrigerant leaks from poorly maintained or improperly disposed equipment hence are considered environmentally hazardous. Economic and demographic changes as well as increasing prosperity expand these issues over the whole world and emphasize the requirement for an alternative, new cooling technology.

Passive radiative cooling systems can operate without external energy input and thus are potential energy-saving applications for the future. This concept can be applied to energy-efficient buildings and enhanced solar cells, water harvesting, or geoengineering strategies in general. In nature, some insects show remarkable ways to keep themselves cool by structuring their chitin filaments,[5] hairs,[6] or butterfly wings.[7] Although nature provides these sources of inspiration for materials design, controlling the functionality of thermal emitters with the best combination of materials and photonic or geometric features is crucial for the development of this new technology. Another critical point is that mainly photonic structures

are favored in nature. These are incredibly complicated in design and hard to mimic for large-scale applications and commercialization.[8] Interesting materials for radiative cooling like silicon carbide are already investigated in simulations but could not be experimentally implemented due to manufacturing problems. For example, biomimetic palm-like structures[7] can only be fabricated in a simple form via sophisticated electron-beam lithography or analyzed submicron to micron-sized spherical and ellipsoidal particles[9] were not experimentally fabricated yet.
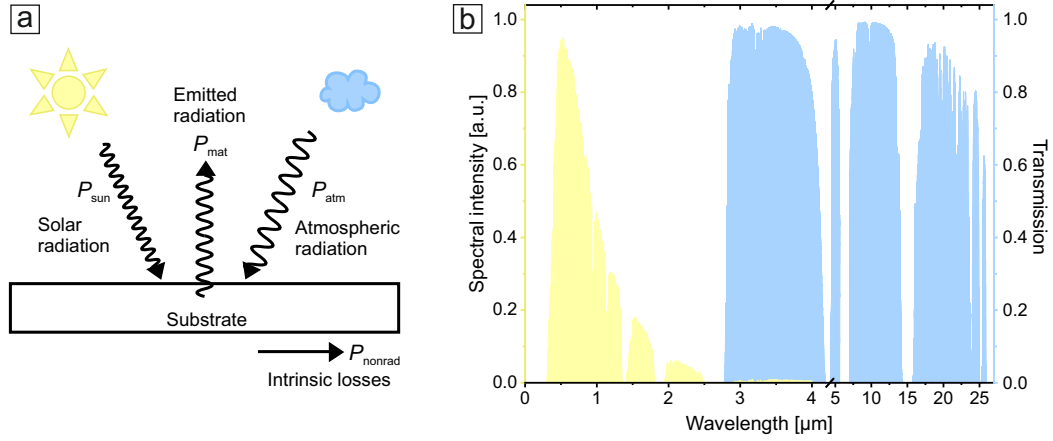
1.1 Radiative cooling

Radiative cooling occurs when a body loses heat by thermal radiation. In general, a net photon heat flow from a hot to a cold object carries both energy and entropy[10] away from the hot object, leading to radiative cooling.[11] This passive process does not need any energy input. One basic example is the human body: a significant amount of its heat can be emitted via thermal radiation due to the colder ambient environment. The concept of cooling down objects on earth relies on the transparency window of the earth's atmosphere in the mid-IR wavelength between 8-13 μm. The spectral peak of thermal radiation from an object at ambient temperature interleaves with the earth's sky window. Hence the heat can be radiated through the atmosphere to the cold outer space. The demonstration of the nighttime radiative cooling, where a black emitter can become colder than the ambient temperature, was already published in the 1970s by Catalanotti[12] and Bartoli et al.[13]

However, the cooling demand in modern life usually peaks during the day. According to that, performing radiative cooling under direct sunlight is very important. Black emitters used for the nighttime experiments will be heated up by the sunlight and thus are no longer suitable. Kirchhoff's law of thermal radiation describes that the wavelength-specific radiative absorption equals the emission of a material body at thermal equilibrium. Therefore, it is necessary that the materials for daytime cooling have a strong reflection in the UV/Vis range and strong absorption in the mid-IR, leading to minimal energy absorption and maximum energy emission, respectively.

Considering all heat exchange processes of a radiative cooler, the net cooling power P_{cool} can be described as[14,15]

$$P_{\text{cool}}(T) = P_{\text{rad}}(T) - P_{\text{nonrad}} \qquad (1.1)$$

Figure 1.1.: a. Schematic illustration of the considered energy exchange processes of a radiative cooler. b. AM1.5 solar spectrum (yellow) and the atmospheric transmittance spectrum (blue) for the location Bayreuth using MODTRAN®.[16]

$$P_{\mathrm{rad}} = P_{\mathrm{mat}}(T) - P_{\mathrm{atm}}(T_{\mathrm{amb}}) - P_{\mathrm{sun}}(T) \qquad (1.2)$$

where P_{mat} represents the power emitted by the material, P_{sun} the incident solar power absorbed by the cooler, P_{atm} the absorbed power due to atmospheric radiation, and P_{nonrad} the intrinsic losses because of convection and conduction. These energy exchange processes are schematically shown in Figure 1.1.a.

The solar radiation is typically modeled with the AM1.5 spectrum and the atmospheric transmission spectrum for an exact location can be modeled using MODTRAN® (see Figure 1.1.b).[16]

The energy radiated by the material can be calculated by the following equation:

$$P_{\mathrm{mat}} = 2\pi \int_0^{\pi/2} \sin\theta \cos\theta \int_0^\infty I_{\mathrm{b}}(\lambda, T_{\mathrm{mat}})\, \epsilon_{\mathrm{mat}}(\lambda, \theta)\, \mathrm{d}\lambda\, \mathrm{d}\theta \qquad (1.3)$$

with the spectral irradiance of a blackbody described by Planck's law I_{b}, which depends on the wavelength and temperature T_{mat}. The emissivity of the material ϵ_{mat}, which depends on the wavelength and the polar angle θ. θ denotes the angle between the direction of the solid angle and the normal direction of the surface.

$$P_{\mathrm{sun}} = \int_0^\infty I_{\mathrm{AM1.5}}(\lambda)\, \epsilon_{\mathrm{mat}}(\lambda, \theta_{\mathrm{sun}})\, \mathrm{d}\lambda \qquad (1.4)$$

is the incident solar power absorbed by the radiative cooler, where $I_{\mathrm{AM1.5}}$ describes the AM1.5 spectral distribution of solar radiation and the emissivity of the material, which depends on the angle of the incoming sunlight θ_{sun}.

The downwards radiation from the atmosphere can be calculated by following equation:

$$P_{\mathrm{atm}} = 2\pi \int_0^{\pi/2} \sin\theta \cos\theta \int_0^\infty I_{\mathrm{b}}(\lambda, T_{\mathrm{atm}})\, \epsilon_{\mathrm{atm}}(\lambda, \theta)\, \epsilon_{\mathrm{mat}}(\lambda, \theta)\, \mathrm{d}\lambda\, \mathrm{d}\theta \qquad (1.5)$$

where the the emissivity of the atmosphere $\epsilon_{\mathrm{atm}}(\lambda, \theta) = 1 - \tau_{\mathrm{atm}}(\lambda, 0)^{1/\cos\theta}$ with $\tau_{\mathrm{atm}}(\lambda, 0)$ being the transmission coefficient of the atmosphere in the zenith direction.

$$P_{\mathrm{nonrad}} = h_{\mathrm{nonrad}} \left(T_{\mathrm{atm}} - T_{\mathrm{mat}}\right) \qquad (1.6)$$

Intrinsic losses are dependent on h_{nonrad}, which is a comprehensive heat transfer coefficient, that describes conductive and convective heat exchange with the environment. The mean literature value[14,17–19] depending on different climatic conditions is $4.4\,Wm^{-2}K^{-1}$.

The equations show that the material's emissivity significantly influences the net cooling power.[20] In general, the emissivity profiles can be distinguished between three cases: First, the blackbody emitter, which has a constant emissivity over the entire mid-IR range. This radiative cooler can maintain his body at ambient temperature while maximizing the net cooling power. Second, a spectral selective emitter, which shows a distinct emissivity in the sky window ranging from 8 - 13 μm and zero emissivity elsewhere. Here, the material can theoretically cool down to $\sim -60\,°\mathrm{C}$. Radiative cooling to $40\,°\mathrm{C}$ below ambient temperature has experimentally been shown[21] using a selective emitter in a vacuum chamber for thermal insulation. And third an ideal emitter, where the emissivity is optimized for every angle and wavelength.[22] With perfect thermal insulation, the material could reach $-100\,°\mathrm{C}$ below ambient temperature. Consequently, the emissivity profile can be tuned depending on the desired working conditions and applications.

Another huge aspect of radiative cooling is the emissivity of the atmosphere. Water vapor in the air has strong absorptions in the IR region. Thus, the humidity, the temperature, the weather condition, and the overall climate of a location have a considerable influence on the performance of a radiative cooler.[23] This has to be kept in mind when comparing experiments in the literature. More recently, the thickness

optimization for passive cooling emitter materials in a back-reflector configuration was investigated.[24] Overall, not only the material itself and its' structure but also the thickness have a significant influence on daytime radiative cooling.

In recent years, several publications examined various materials, like polymers,[25–28] multilayer thin films,[29–31] metamaterials,[32–35] and bioinspired materials[6,36,37] for a vast amount of different applications in the field of radiative cooling, like clothing,[38–41] architecture,[42–44] solar cells,[45–47] and fluid cooling panels.[48–50]
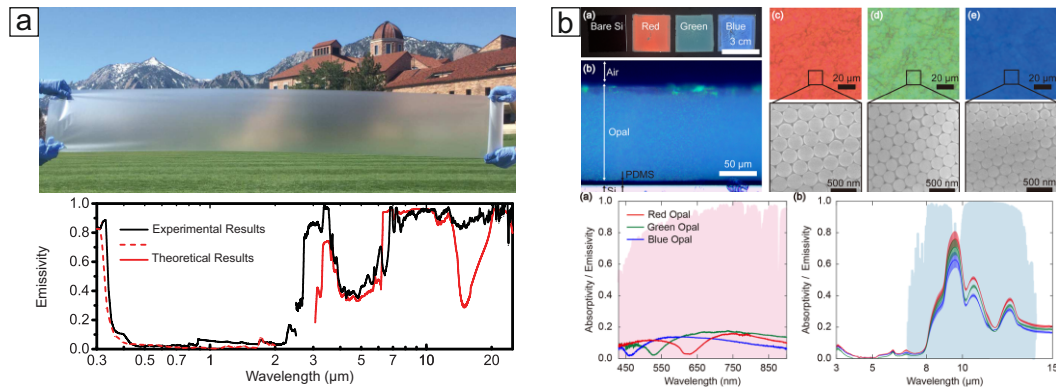
Figure 1.2.: Examples of published particle-based materials for passive radiative cooling. a. TPX-based hybrid metamaterial with randomly distributed SiO$_2$ microsphere inclusions for large-scale radiative cooling. The measured emissivity/absorptivity (black curve) and the theoretical results for the same metamaterial structure (red curves) over the total UV/Vis and IR range are plotted for comparison. From „Scalable-manufactured randomized glass-polymer hybrid metamaterial for daytime radiative cooling", by Zhai, Y.; Ma, Y.; David, S. N.; Zhao, D.; Lou, R.; Tan, G.; Yang, R.; Yin, X. *Science* **2017**, *355*, 1062-1066. Reprinted with permission from AAAS. b. Bragg reflective colorization of silica opals, self-assembled on a PDMS/p-doped crystalline silicon wafer. Experimentally measured absorptivity/emissivity of bluish, greenish, and reddish opals in the visible and mid-IR regions. Reprinted with permission from „Colloidal photonic assemblies for colorful radiative cooling", by Kim, H. H.; Im, E.; Lee, S. *Langmuir* **2020**, *36*, 6589-6596. Copyright 2020 American Chemical Society.

Substantial research efforts have also been made in particle systems for radiative cooling. Atiganyanun et al.[51] investigated the optimum particle size and packing density of silica paint for strong scattering in the solar range by determining the photon transport mean free path. With SiO$_2$ particles of 2 μm and a thick layer of $\sim$ 700 μm, they were able to obtain sub-ambient temperatures. The main driving force for this material class was the exclusion of solar radiance uptake. The infrared emissivity, in this case, was provided by the fundamental properties of SiO$_2$ microbeads. Kim et al.[52] used much smaller particles and arranged them in an ordered fashion resulting in colorful photonic crystals. The IR properties of the sub-micron SiO$_2$ particles demonstrated a more distinct emission in comparison to

the amorphous paints mentioned before. An even broader emissivity was utilized by Zhai et al.,[53] who used 8 μm SiO$_2$ beads in a polymethylpentene (TPX) matrix. At this particle size, higher-order modes of Fröhlich resonances are excited, which cover a considerably broad spectrum in the IR range. Since the particles were embedded in TPX, the necessary solar reflection was only achieved by an Ag back coating of the composite film. Another group[54] also loaded a TPX matrix with an Ag reflective coating with different volume fractions of silica and CaMoO$_4$. One of the examples of combining broadband particle emissivity and order was published by Jaramillo-Fernandez et al.[55] An ordered colloidal monolayer of 8 μm SiO$_2$ beads on soda-lime glass was sufficient to reduce the heat-up of a silicon substrate by 14 °C. The combined interaction of higher-order mode Fröhlich resonances, surface phonon polariton (SPhP) excitation at elevated temperatures, and grating coupling improved the IR emissivity.

SiC particles are less intensively investigated. Whereas nanostructured SiC is an exciting material for surface phonon polariton engineering, dispersed SiC particles are not very common for passive cooling applications. The material is more used in planar (Bragg) stack configurations of gas-phase deposited thin film structures, for instance, as proposed by Raphaeli et al.[56] The ultra-broadband photonic structure showed cooling in the presence of convective and conductive heat exchange and nonideal atmospheric conditions. Gentle et al.[57] used mixtures of SiC and SiO$_2$ particles in their early PE-based composite material. A double layer approach with a TiO$_2$ refractive layer and an emission layer consisting of SiC and SiO$_2$ was established by Bao et al.[58] in 2017. They simulated an optimum for a radiative cooler with a radius of 0.5 μm for the titania particles and a radius smaller than 300 nm for the silica and SiC particles.

In summary, each approach features its unique advantages and drawbacks. Particles in the sub-μm range are more beneficial for broadband emissivity. Order is additionally useful for grating coupling. However, this has to be optimized in competition with disordered materials' scattering properties, which mitigate solar radiance uptake. In addition to these findings, several publications characterized the influence of particle loading on the optical properties and cooling performance. As expected, higher particle loadings increase scattering in the solar range and emissivity in the infrared range.[59] Since the overall performance also depends on film formation properties, particle distribution inside the matrix, film thickness, etc. there is no general optimum composition reported so far.

In dielectric particles like SiO$_2$, SiC or TiO$_2$, SPhP modes can be excited.[60] This leads to absorption and emission in the mid-IR to the far-IR range for radiative

cooling. The particles' size and shape can impact the resonance of the SPhP mode and thus need to be controlled for an optimum photonic composite structure. This phenomenon is discussed in more detail in the following section.

1.2 Surface phonon polaritons

In solid-state physics, a phonon is described as the collective excitation of a lattice vibration in condensed matter. They can be further distinguished between acoustic phonon modes and optical phonon modes (see Figure 1.3). Acoustic modes are coherent movements of atoms in the lattice. This is the basis for the thermal conductivity of a material. Optic phonos are out-of-phase movements of atoms in the lattice. Note that here, the term *optic* is not depending on the optical activity of the phonons, more precisely, the interaction of phonons with photons. Optical phonon modes can only exist when the material shows electric polarisation, for instance, in ionic crystals with different atoms, where adjacent ions have opposed charges. The wavelength of these modes typically lies in the UV/Vis/IR range (THz).
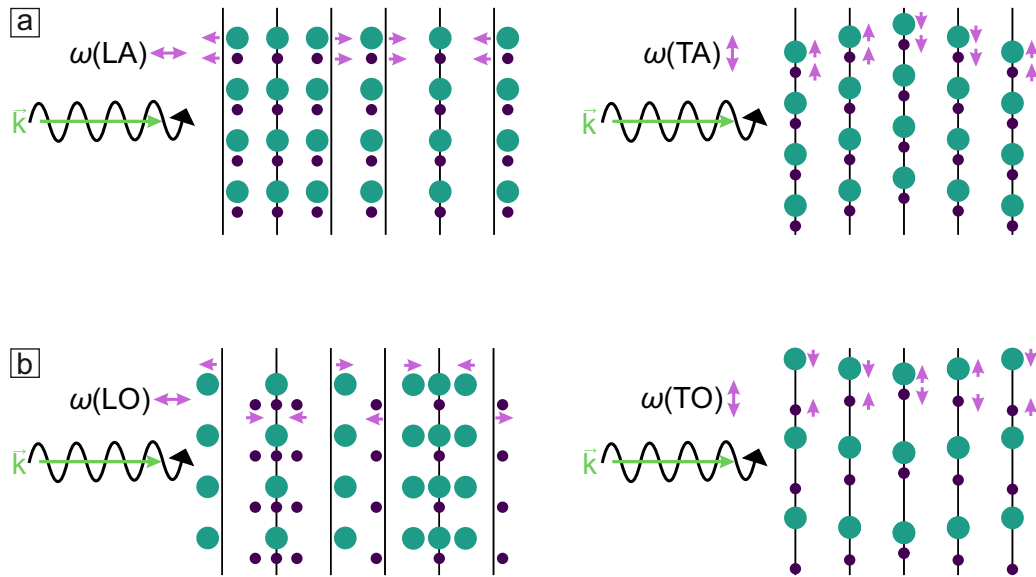
Figure 1.3.: Schematic illustration of longitudinal and transversal acoustic phonon modes (a) and optical phonon modes (b) in an atom lattice.

SPhP are a result of optical phonons interacting with long-wavelength incident fields from the mid-IR (e.g. hexagonal BN[61] and SiC[62]) to the THz range (e.g. GaAs[63]).[64] The surface excitation is mediated by the atomic vibrations through

the dielectric material. Depending on the real and imaginary part of their optical constants (n and k), they can be further divided into two categories.

When the real part of the permittivity is negative between the longitudinal optical (LO) and transverse optical (TO) phonon frequencies, it is called a phononic or polar dielectric material.[65] The frequency-dependent dielectric function can be approximated as a Lorentz oscillator:

$$\varepsilon(\omega) = \varepsilon_\infty \left(1 + \frac{\omega_{LO}^2 - \omega_{TO}^2}{\omega_{TO}^2 - \omega^2 - i\omega\gamma} \right) \tag{1.7}$$

where ε_∞ is the high-frequency permittivity of the material, ω is the incident frequency, γ is the damping constant. The TO and LO phonon frequencies are described as the pole at ω_{TO}, and a zero-point crossing at ω_{LO}. The spectral range between LO and TO is referred to as the Reststrahlen Band.[64] This is represented in Figure 1.4, where the TO and LO phonon energies with respect to the Reststrahlen band of a 4H-SiC substrate are shown. Due to the evanescent character of the plane wave in the material, both localized and propagating SPhP modes can be provided in nanostructures and on the surface of these polar dielectric crystals. This is analogous to localized surface plasmons and surface plasmon polaritons in metals. Another similarity to plasmons is, that the SPhP oscillation can also be influenced and enhanced by structural engineering. The first efforts to realize localized SPhP resonances were published in 2002 by Hillenbrand et al.[66] and Greffet et al.[67] In general, the resonance can be tuned by grating the structures[68] or changing the size and periodicity[9] of the material. If the Reststrahlen band lies within the sky window, the material is suited for radiative cooling - in combination with other material properties. The phonon polariton resonance in phononic materials can easily be induced, and the damping rate is low so that sharper absorption bands can be obtained. It has been shown[69] that SPhP can be excited not only in crystalline polar materials but also in amorphous materials, like SiO_2. Here, the emissivity is not only controlled by their Reststrahlen band but also by the materials' intrinsic absorption.

In a dielectric material, where the real part of the permittivity is positive within the UV, and mid-IR wavelength range, the excitation of SPhP is not possible. However, these materials can be used as thermal emitters due to their intrinsic absorption. Furthermore, Mie resonances[70] for both electric and magnetic modes can be induced by any high refractive index dielectric particles. Those modes confine the electric field inside a particle, and as a consequence, the energy of the incident electromagnetic wave is efficiently absorbed. If the particle diameter lies in the same
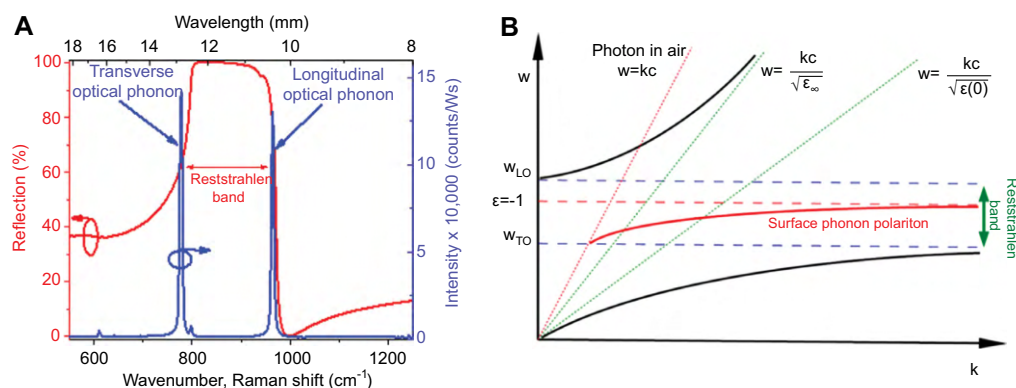
Figure 1.4.: FT-IR Reflection (red curve) and Raman (blue curve) spectra collected from a semi-insulating 4H-silicon carbide wafer. The Reststrahlen band lies in between the TO phonon and the LO phonon. Adapted with permission from „Low-loss, infrared and terahertz nanophotonics using surface phonon polaritons", by Caldwell, J. D.; Lindsay, L.; Giannini, V.; Vurgaftman, I.; Reinecke, T. L.; Maier, S. A.; Glembocki, O. J. *Nanophotonics* **2015**, *4*, 44-68.

range as the wavelength of the light, electromagnetic waves are elastically scattered on spherical objects and higher-order Mie resonance modes can be excited. These modes can spectrally overlap, making it particularly interesting for non-selective emitters that should possess broadband absorption.

SiO_2 particles have been extensively used for passive cooling applications. Silica is readily available and easy to handle and process. It is particularly suitable for thermal emission in the first sky-window range (8-13 μm) owing to its molecular absorption resonance and its possibility to support surface phonon polaritons within two Reststrahlenbands (~ 8 – 9.3 μm, ~ 21 μm).[55] Furthermore, SiC nano- and microparticles are interesting for the design of selective emitting materials in the infrared range since their optical properties can be strongly altered based on the particle geometry. Rockstuhl et al.[9] showed the tuning of the SiC resonance on spherical and elliptical particles, and Mutschke et al.[71] investigated the influence of polytypes and shapes. However, experimental fabrication of defined SiC particles is still difficult, and absorption in the visible part of the spectrum can offset the infrared gain. Consequently, SiC particles are typically used in combination with SiO_2 or TiO_2 to address the optimum optical properties.

1.3 Synthesis techniques

This thesis used colloids from different materials as reactants or colloidal building blocks. Monodisperse silica particles were synthesized by a Stöber synthesis,[72]

which is an example of a sol-gel process. This synthesis had to be adjusted for other silane precursors due to steric hindrances or different solubilities in the reaction mixture. Polymer particles were either synthesized with emulsifier-free emulsion polymerization or dispersion polymerization according to the wanted size range of the particles. Additionally, the charge of the surface of th particles can be varied by using different co-monomers. To convert silica to silicon carbide, two thermal fabrication techniques were used. This chapter outlines the theory and the basic mechanisms of these mentioned syntheses and polymerizations.
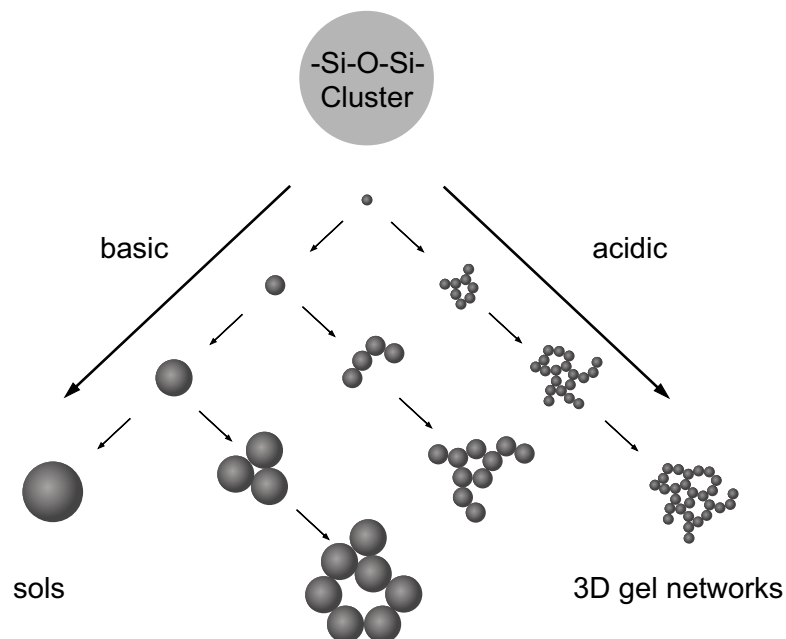
1.3.1 Inorganic silica particles

For the fabrication of metal oxides, mainly for silicon and titanium, a typical fabrication technique is the sol-gel process. In this bottom-up approach, molecular precursors are converted to amorphous network structures. All reaction parameters and the precursors themselves have a certain influence on the structure of the sol-gel materials. A stable suspension of colloidal particles in a liquid is called *sol*. When a three-dimensional continuous solid network is formed due to the formation of covalent bonds between the sol particles, it is described as *gel*. This gel network is surrounded and supported by a continuous liquid phase.[73]

The basic principle is a wet-chemical technique. The precursors - typical metal alkoxides and metal chlorides - are converted to small seed molecules with hydrolysis and polycondensation reactions and form the solid phase. According to the chemical conditions in the system, different outcomes are favored (see Figure 1.5). In base-catalyzed sols, the individual particles grow and form suspensions of sub-micrometer spherical colloids. On the other hand, in acidic conditions, the particles aggregate prior to their growth and form a continuous network of low-density polymers due to higher interparticle forces.

Different materials from different stages of the sol-gel reactions are produced for a wide application range, for example in electronics,[74] medicine,[75] optics,[76] or chromatography.[77] The precursor sol can be deposited on a substrate by dip- or spin-coating for film formation. Wet gels can either be cast into the desired shape to form dense ceramics, or the solvent can be evaporated to produce aerogels. Furthermore, it is a standard method for the fabrication of micro- and nanospheres.

The following explanation of the chemical principle behind the sol-gel technique will be given for silica-based materials. Typical precursors are aqueous solutions of silicates and silicon alkoxides, like tetramethyl orthosilicate (TMOS) or tetraethyl orthosilicate (TEOS). The silanol (Si-OH) and alkoxy (Si-OR) groups have to

Figure 1.5.: Schematic building of silica particle clusters to sols or 3D gel networks.

be transformed to siloxane compounds (Si-O-Si) by condensation reactions. In comparison to typical organic polymerizations, the reactive Si-OH groups must be created by hydrolysis prior to the polycondensation. The mechanism of the reaction has to be considered separately for the acid and base catalyzed route and can be seen in Figure 1.6.

Under acidic conditions, the oxygen atom of $\equiv$Si-OR is protonated in a fast first step. In addition to that, the electron density is withdrawn from the central silicon atom, which makes it more electrophilic and suitable for an attack by water. A silanol group is formed after eliminating an alcohol and the deprotonation of the attacking water molecule. The condensation reaction is then started by two partially hydrolyzed $\equiv$Si-OH species, forming a siloxane bond with the elimination of water or alcohol. In basic systems, the hydrolyzation starts with a S_N2-type mechanism by a nucleophilic attack of an OH$^-$ group to the silicon atom of $\equiv$Si-OR. The following condensation is started by a deprotonated $\equiv$Si-OR$^-$ species and the Si-O-Si bond is formed by elimination of RO$^-$. In both cases, hydrolysis and condensation reactions go on simultaneously, also leading to different reactant possibilities. Monomeric species with one siloxane bond can react with oligomeric species or even bigger Si-O structures. Each of these reaction types has its own kinetic parameters and thus, a variety of linear, branched, and cage structures are formed. The synthesis can be controlled by adjusting parameters, like the water concentration, the pH value, or the temperature, to produce the desired silica structure.

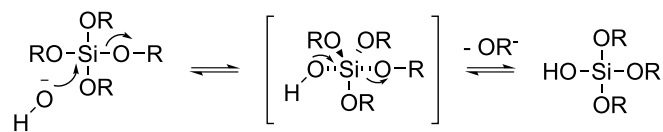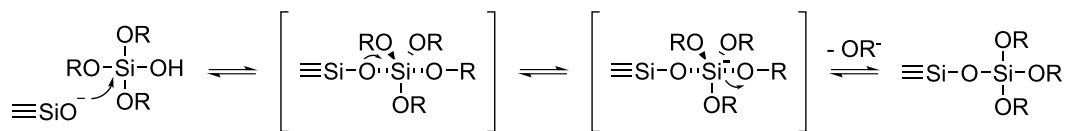a) Acid catalyzed

Hydrolysis
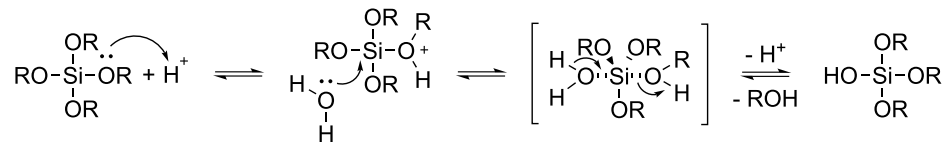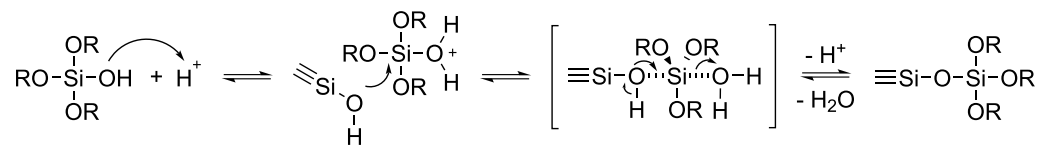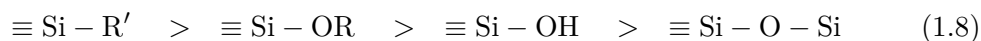

Condensation

b) Base catalyzed

Hydrolysis

Condensation

Figure 1.6.: Acidic and base catalyzed route of the hydrolysis and condensation reactions to build silica networks.

The inductive effect of the subsituents attached to the silicon atom also has an important influence on the reaction rates. The following equation shows the decreasing electron density at the silicon atom of reaction intermediates as hydrolysis and condensation proceeds.[73]

$$\equiv \mathrm{Si} - \mathrm{R}' \quad > \quad \equiv \mathrm{Si} - \mathrm{OR} \quad > \quad \equiv \mathrm{Si} - \mathrm{OH} \quad > \quad \equiv \mathrm{Si} - \mathrm{O} - \mathrm{Si} \qquad (1.8)$$

Hydrolysis is increased by electron providing subsituents in acidic media and decreased in basic media and vice versa, due to the stabilization of reaction intermediates.[78,79] The absolute rate constants are not too decisive, but instead the relative rates of hydrolysis and condensation among each other. As already mentioned in the beginning, this results in different reaction outcomes under acidic and basic conditions. In acidic media the reaction results in polymer-like gels with small pores, due to the hydrolyzation of all species at an early stage and the formation of small oligomeric species with Si-OH groups, where further reactions at the terminal Si atoms are favored, during the condensation. In basic media particle formation with a high porosity (colloidal gel) is more likely. Here, hydrolysis is the determining step, because a continuous source of monomers is required for particle growth. Hydrolyzed species are immediatly consumed by reaction with existing clusters, due to faster condensation rates.

The well-known synthesis of spherical and monodisperse silica particles was invented by Stöber[72] and later refined by Bogush[80] and Giesche[81]. Here, the silica precursor TEOS is hydrolyzed in the presence of ammonia as a catalyst in a one-step process. The size distribution is controlled during synthesis by either the concentration of the reactants or the temperature and commonly results in colloidal silica with diameters from 50-2000 nm and small polydispersity. With higher concentrations of water and ammonia, larger particles are formed but accompanied by a broadening of the size distribution.[82] Otherwise, higher concentrations of the TEOS precursor lead to smaller particles due to more nucleation seeds. The particles can also be modified by additional compounds to the reaction mixture, for example, to synthesize mesoporous silica. Here, surfactants like cetyltrimethylammonium bromide (CTAB)[83] or glycerol[84] are added. The surfactant micelles are incorporated into the growing silica network, forming particles with narrow channels. After calcination and thus removal of the organic material, mesoporous voids are obtained throughout the particle. Moreover, core-shell particles and thus silica hollow spheres can be produced based on the Stöber process. A general method to coat metal (oxide) or polystyrene particles was described by Graf et al.[85] After the functionalization with the amphiphilic polymer poly(vinylpyrrolidone) (PVP), the particles can be

coated with a smooth and homogeneous silica shell with variable thickness in a seeded growth process.

Acidic silica sols or other metal oxide precursors are often used to infiltrate a sacrificial three-dimensional colloidal crystal matrix to produce inverse opal structures with highly ordered interconnected pores. These structures are of great interest for optical and photonic applications[86,87] or as colorants[88] and sensors.[89] One crucial point is the infiltration of the sol-gel precursor into the target materials, where the liquids enter the interstitial spaces by capillary forces. This process can be assisted by applying suction or a vacuum to remove air bubbles. Additionally, the wettability of the colloidal crystal plays an important role.[90]

1.3.2 Fabrication routes to silicon carbide

Silicon carbide (SiC) is an advanced ceramic common in space but extremely rare on earth. In nature, it occurs only in negligible amounts in meteorites,[91] carborundum, or kimberlite. The material shows remarkable properties like extreme hardness, high thermal conductivity, low thermal expansion, and excellent chemical inertness. The industrial application[92] ranges from the use as abrasive, for example, in sandblasting techniques or high-performance brake discs in automobiles to additives in fire-resistant materials or heating elements to modern electronic applications like semiconductors,[93] sensors,[94] field-effect transistors,[95] or supercapacitors.[96] Due to the high and diverse demand, most SiC is synthetic. The general reaction is shown in the following equation:

$$SiO_2 + 3\,C \longrightarrow SiC + 2\,CO \tag{1.9}$$

Combining silica sand and carbon at high temperatures between 1600 °C and 2500 °C *via* the Acheson process[97] is the simplest commercial process to produce silicon carbide. However, the material formed with this method varies in purity, which is disadvantageous, especially for the semiconductor industry. With the Lely method[98] high-quality SiC single crystals can be fabricated by sublimation of SiC powder in argon gas at 2500 °C. Routes to SiC ceramics can also be achieved with the conversion of polymer precursors, such as polysiloxanes[99,100] or polycarbosilanes[101,102], at high temperatures. In the latter case, silicon and carbon are already covalently bonded in the polymer backbone. More recently, nanostructured SiC gained attention, as the optical and electrical properties can be tuned by variating the size and shape of the material.

SiC particles can be fabricated by top-down and bottom-up methods, which address distinct particle sizes depending on the method.[103] Top-down techniques include laser ablation,[45,104] etching (acid, plasma, voltage),[105–107] and milling.[108] Ablation and etching mainly produce SiC particles in a sub 100 nm size range, whereas milling yields (sub)micron-sized beads. In the case of bottom-up techniques, SiC powders can either be produced by a direct carbothermal reaction of silica and a carbon source at high temperatures above 1000 °C, or by a magnesiothermic reduction[109] at lower temperatures (ca. 800 °C) with magnesium as a reducing agent.

$$SiO_2 + 2\,Mg \longrightarrow Si + 2\,MgO \tag{1.10}$$

$$Si + C \longrightarrow SiC \tag{1.11}$$

Both of these techniques have their advantages and disadvantages. The production of SiC particles with either of these methods opens the possibility of adjusting particle shape, size, and morphology when the precursor silica can be produced by sol-gel processes.[110] For example, Raman et al.[111] synthesized SiC from TEOS, methyltriethoxysilane, or mixtures of both and with different carbon sources like phenolic resin, ethylcellulose, or starch. The obtained gels were heated to 1550 °C in an argon atmosphere. All products from different precursors were found to be β-SiC with crystallite sizes from 9 to 53 nm. SiC structures from a carbonaceous silicon xerogel starting from TEOS and saccharose were prepared by Zheng et al.[112] These β-SiC particles have sizes from 100 nm to 1000 nm and a surface area up to 141 $m^2\,g^{-1}$. None of these mentioned synthesis routes led to well-defined spherical morphologies. The powder-like materials consist either of polydisperse small particles with a large size distribution or are non-defined in the meso- and micron scale. Only a few studies have been reported about spherical SiC particles. In the group of Liu et al.[113] nanoparticles with average sizes from 10 to 200 nm were synthesized by fluidized bed chemical vapor deposition using hexamethyldisilane (HMDS) as a single precursor. This method was designed to achieve the continuous formation of particles in a scalable reactor environment. Hatakeyama et al.[114] and Seog et al.[115] prepared spherical silicon carbide by acid- or base-catalyzed condensation of phenyltrimethoxysilane (PTMS) and TEOS in water.

Primarily, the magnesiothermic reduction has solely been used to synthesize silicon nanostructures from silica precursors.[116] With new interests in research areas like lithium-ion batteries, the method was also applied to produce Si/C composites and SiC materials. However, the reaction mechanism to these totally different crystal phases is not yet fully understood. Ahn et al.[117] proposed that SiC is formed at

the interface between silica and carbon when silicon intermediates encounter carbon through diffusion. Additionally, the outcoming material is influenced by the contact areas of the reactant materials, the reaction temperature, gaseous atmosphere, the heating rate and the stochiometry of the mixtures, which makes the magnesiothermic reduction a very sensitive and challenging synthesis.

Composite materials are typically synthesized with a mesoporous silica matrix, such as SBA-15, infiltrated with a carbonaceous material like sucrose.[118] Resorcinol-formaldehyde/silica composite aerogels were successfully converted to silicon carbide with average sizes of around 10 nm at reduced temperatures by Chen et al.[119] Nguyen et al.[120] did not mix their silica/cellulose nanocrystal precursor with the Mg turnings, but instead placed them on the opposite ends of the reaction boat. The distance between the magnesium vapor source and the silica substrate can also produce different outcome materials. In 2010, Shi et al.[121] fabricated a crystalline ordered hierarchical macro-mesoporous (OHM) SiC material at 700 °C via magnesiothermic reduction. Small SiO_2 particles up to 214 nm, rods and fibers were successfully transformed into SiC by Dasog et al.[122] with the solid-state reaction of the sol-gel derived precursor. Additionally, a first attempt was made to produce SiC hollow spheres with magnesiothermic reduction.[123] The carbon-coated silica HS were mixed with Mg and salt to enhance the diffusion process and to absorb heat spikes during the process, destroying the microstructure.

More than 250 polymorphs of silicon carbide are known, including various amorphous phases[124]. The three major SiC polytypes are shown in Figure 1.7.
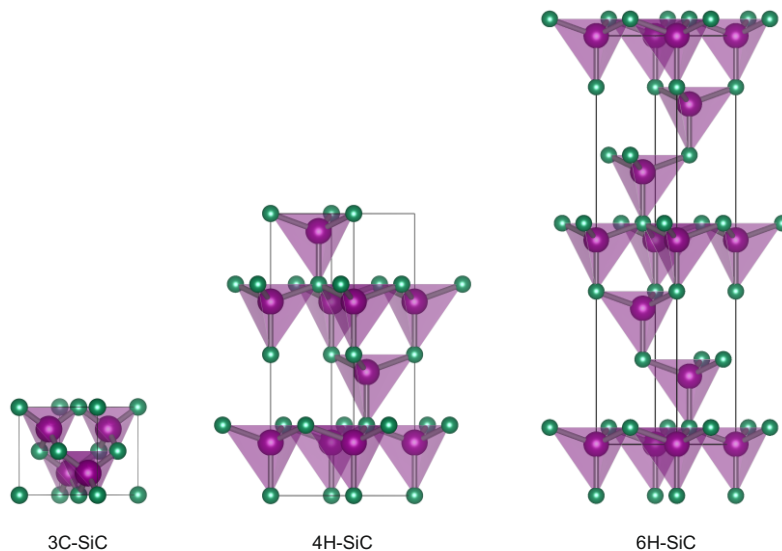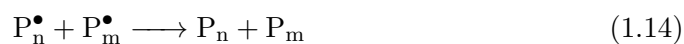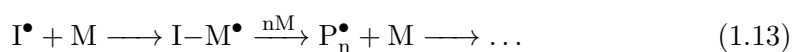

Figure 1.7.: The three most common crystallic phases of silicon carbide: (β)3C-SiC, 4H-SiC and (α)6H-SiC.[125]

The hexagonal alpha SiC is the most common polymorph and is formed at temperatures above 1700 °C. Below this temperature, the beta modification with a zinc blende crystal structure is favored. The crystallinity of the material is an important factor for the application area. Amorphous SiC is an attractive material for photovoltaic devices due to the temperature stability and dopability[126] or for developing new electroluminescent substances.[127] On the other hand, crystalline forms offer a large bandgap, high thermal conductivity, and a high electron drift velocity, which makes them of particular interest in the semiconductor industry.[128]

1.3.3 Polymer particles

A standard method for the synthesis of latex particles is the emulsion polymerization. This type of polymerization is counted as radical polymerization, which proceeds via the chain growth of monomers. The four main reaction stages are: generation of the radical initiator (1.12), propagation via radical addition of monomers (1.13), chain transfer and termination by disproportionation (1.14) and chain termination by radical-radical recombination (1.15).

$$I-I \longrightarrow 2\,I^{\bullet} \tag{1.12}$$

$$I^{\bullet} + M \longrightarrow I-M^{\bullet} \xrightarrow{nM} P_n^{\bullet} + M \longrightarrow \ldots \tag{1.13}$$

$$P_n^{\bullet} + P_m^{\bullet} \longrightarrow P_n + P_m \tag{1.14}$$

$$P_n^{\bullet} + P_m^{\bullet} \longrightarrow P_n-P_m \tag{1.15}$$

with the initiator I, the monomer M and polymer chains P with n or m monomeric units. At first, a radical species is generated in the initiation process *via* thermal decomposition, photolysis or redox reactions. At an early stage of the reaction and after a certain degree of conversion, the viscosity increases, which leads to diffusion hindering of free radicals, and thus an increase in molecular weight.

Compared to free radical polymerization, the emulsion polymerization has the following advantages: the reaction velocity is high and the polymer can reach high molecular masses. Due to the aqueous medium, the viscosity of the reaction mixture stays low during the process. There are two variants of emulsion polymerization, where the main difference is the stabilization of the reactants. In the conventional method, the monomer and the polymer are located in micelles stabilized by surfactants. In contrast, in the emulsifier-free process, the monomer forms large droplets and the resulting polymer is electrostatically stabilized by charged groups of the

initiator and the co-monomer. The latter was first introduced by Goodwin et al.[129] and refined for positive[130] and negative[131] particles. The synthesis steps of an emulsifier free emulsion polymerization are schematically shown for positively charged particles in Figure 1.8.a.

The hydrophobic monomer is distributed in large monomer droplets in the solvent. The polymerization starts when the water soluble initiator is thermally decomposed into two charged radicals. The radical species react with monomer units in the aqueous phase until a critical chain length. Then, the oligomer becomes too hydrophobic and forms small primary particles. The coagulation of these primary particles leads to a mature particle nucleus, which is colloidally stable and thus can hold a sufficient amount of monomer in his hydrophobic interior. This reaction step is the main characteristic for a homogeneous nucleation process.[132] As the reaction proceeds, the particles are stabilized by charged groups of initiator or co-monomer at the particle water interface. Further monomer diffuses into the particles until the consumption of the reactants.[133–135] Furthermore, the steric stability can be increased by adding PVP and the positively charged co-monomer MTC for the cationic particles and AA or PSS for negatively charged particles.

The absence of a surfactant in the dispersion has additional positive effects when the particles are used for further processes. When forming colloidal crystals, the attractive and repulsive forces during self-assembly can be significantly influenced by additional surface-active agents. For larger particle diameters from 700 nm up to 2 μm, the dispersion polymerization is more suitable. The mechanism of this reaction has been discussed by Barrett and Arshady.[136,137] A schematic illustration of the dispersion polymerization is shown in Figure 1.8.b. Here, both the monomer and the initiator are soluble in the solvent. After the initiator is thermally decomposed in two radical species and nitrogen, the polymerization starts and oligomers are formed. When a critical polymer chain length is reached, the oligomers coagulate into nuclei, becoming insoluble. By adding more monomer, the particles grow in size. The stabilization of the particles is achieved by adding a charged co-monomer, which is incorporated in the particle surface and increases the electrostatic repulsion. Finally, the reaction stops when all of the reactants are converted.

1.4 Colloidal structures

Particles consisting of different materials with various particle dimensions and surface functionalization can be assembled in two or three dimensions to form amorphous or crystalline superstructures. Dependent on the particle building blocks, these
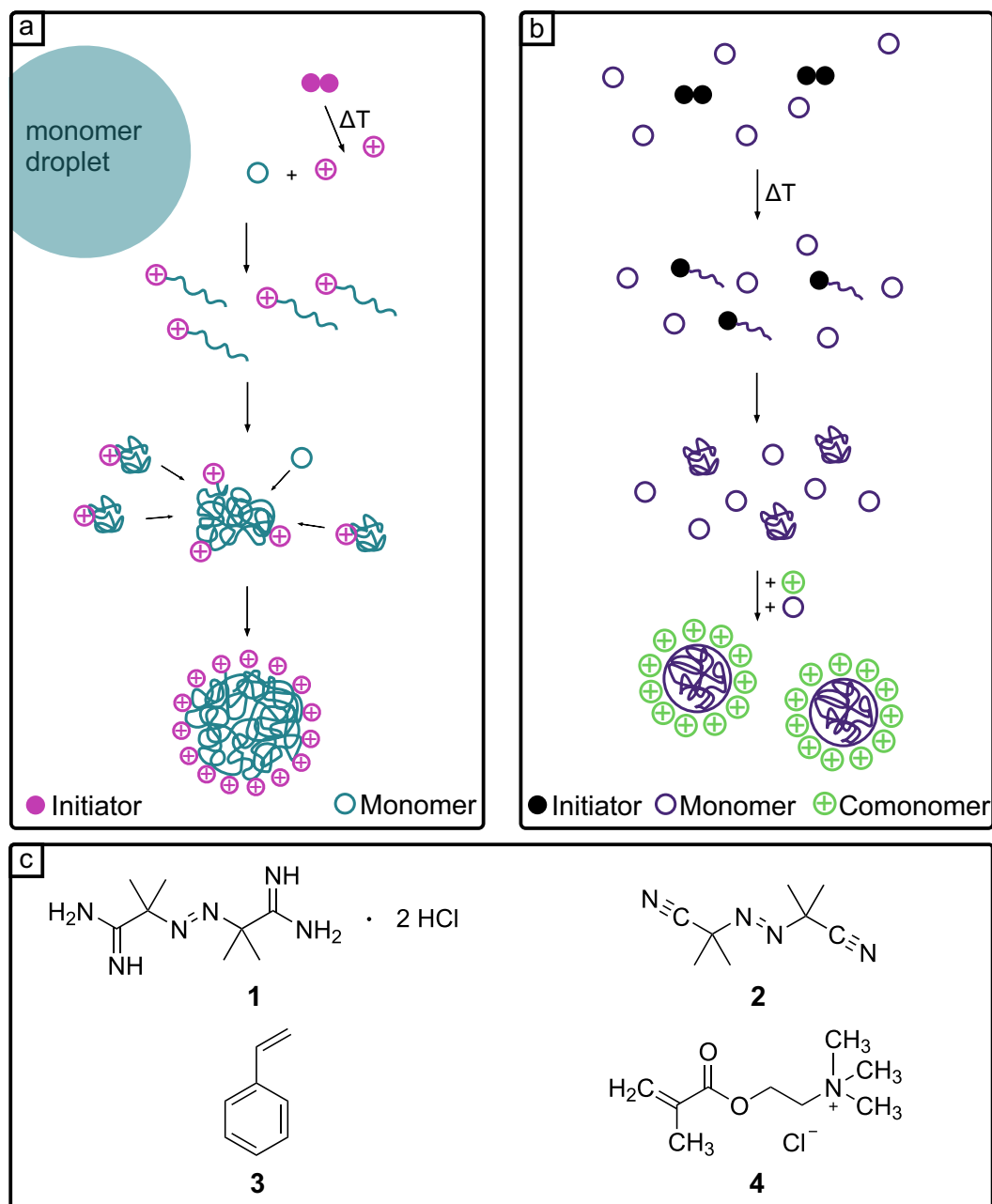
Figure 1.8.: Schematic illustration of an emulsifier free emulsion polymerization (a) and a dispersion polymerization (b). In (c) the chemical structures of the initiators AIBA **1** and AIBN **2**, the monomer styrene **3** and the positively charged co-monomer MTC **4** are illustrated.

colloidal structures can be used in material science,[138] energy migration,[139] or (bio)sensing.[89] The structures can be easily fabricated over big length scales and do not need extensive procedures or expensive equipment. Furthermore, these assemblies are used in hard-templating processes. A precursor can be filled into the pores or absorbed at its surface by impregnation or chemical vapor deposition. The rigid structure determines the size and the morphology of the sample after the removal of the template.[140]

Complex assembly forces can act on the colloidal particles during their organization process. Attractive interparticle forces, repulsive forces from interactions between particles or particles with extended interfaces, and external forces must be in a certain balance to form ordered structures. The most relevant forces are described in the following paragraphs.

Attractive forces. An example of attractive forces between particles at a liquid interface are capillary forces, which result from the surface tension of the liquid pulling the particles together. Furthermore, this depends on the wettability of the colloidal object with the medium and the particle shape. Van der Waals (vdW) forces also depend on the size and shape of the particle and are described by the Hamaker formalism. In comparison to intermolecular vdW forces, colloidal vdW interactions act over larger distances, because the force is proportional to $1/d^2$, for two spheres with the radius $R \gg d$.

Repulsive forces. They can be described by dipolar interactions from ionic groups at the particle surface. This leads, for example, to an asymmetric charge dissociation at air-water or oil-water interfaces.[141] Coulomb interactions between charged particles lead to electrostatic repulsion, which scales with $e^{-\kappa\chi}$, where κ is the inverse Debye length. A detailed explanation of colloidal stabilization is summarized in the DLVO theory.[142] By changing the pH of the dispersion medium or by the addition of salt, the ionic strength and thus the Debye length can be adjusted, and the electrostatic repulsion can be influenced. Steric stabilization can also play a role when the colloidal particles are stabilized with a solvated polymer corona. Due to an emerging osmotic pressure, the particles do not aggregate when the polymer chains are overlapping.[143]

External forces. Particles can be manipulated by barrier compression methods like in the Langmuir-Blodgett technique or with drag forces such as air flow[144], which leads to particle aggregation at a liquid interface. The Brownian motion is a kinetic energy that must be overcome in any assembly process to produce thermodynamically stable structures.[145] Natural gravitational forces increase with the particle size and its density difference with the dispersion medium and lead to

sedimentation. With the use of a centrifuge, the particle sedimentation can be speed up to form colloidal crystals.[146]

There are various 2D assembly methods like dip-coating,[147] floating,[148] or spin-coating[149] to form colloidal monolayers on solid substrates and methods for 3D assembly such as sessile drop,[150] spray deposition,[151] or filtration[152] to get colloidal crystals. The techniques, which were used in this thesis, will be further described in the following and are illustrated in Figure 1.9.
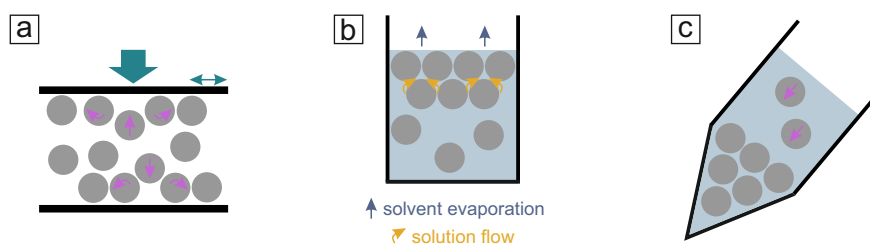
Figure 1.9.: Schematic illustration of the colloidal assembly techniques used in this thesis. a. Monolayer fabrication with an unidirectional rubbing method reported by Park et al.[153], b. Evaporation-induced particle assembly process by Guo et al.[154], c. 3D assembly with a centrifugation assissted method.

The preparation of a large-area monolayer of spherical particles from around 170 nm to 5 μm can be performed with an unidirectional rubbing method according to Park et al.[153] This technique is quick, inexpensive, and requires only a dry powder of the particles and two flat poly(dimethylsiloxane) (PDMS) substrates. The dry powder is placed between these two PDMS substrates and rubbed in random directions until a hexagonally close-packed monolayer is formed. Thereby, the particle-substrate adhesion should be stronger than the particle-particle interaction to separate particle aggregations in the powder. Also, a certain amount of shear force has to be used. The smaller the particles, the larger the shear stress has to be applied in order to transfer momentum to the particles. Large particles need a higher rubbing speed and a smaller external pressure, as they must roll across longer distances with greater tangential force.[153]

One method to prepare highly ordered colloidal particle assemblies was the evaporation-induced self-assembly process proposed by Guo et al.[154] Thereby, a particle dispersion is placed into small beakers. The colloids are pushed towards the meniscus due to water evaporation at the air-water interface. A layer of particles with a few arrays is formed. Then, the suspension flow will start to replace the solvent evaporation force and will drive the colloids into the vacancies between the particles. The formed close-packed structure has a (111)-like plane parallel to the air-water interface. The disadvantage of this method is the relatively long preparation time ($\sim$ several days) because of the slow evaporation of the solvent. A faster assembly process can be

achieved by centrifugation. Here, the particle dispersion is centrifuged in tubes or spot plates. It is essential to control the sedimentation and separation (polydisperse or binary samples) behavior in the system. At high centrifugal forces (e.g. $F = 12000\,g$), the sedimentation occurs very fast, and the system remains in a glassy state. The formation of periodic crystalline structures is mainly achieved at small centrifugal forces ($F = 120\,g$). However, the assignment to only one crystal plane (hkl) is difficult and not precise due to different domains and gradient formation from the bottom to the top layer.[155]

Overall, depending on the method chosen for assembly, the 3D arrays can contain stacking defects, dislocations, and cracks.[156] Typical single-crystal domains extend around tens of micrometers in colloidal crystals with 200 - 500 nm spheres.[86] For photonic applications, the crystals have to be "defect-free" over large areas, whereas for other applications, such as catalysis or energy storage, they do not require perfect periodicity.

1.5 Characterization techniques for particles and composites

This chapter describes the main characterization methods used in this thesis. Simultaneous thermal analysis (STA) was used to get an insight into the thermal processes when producing silicon carbide materials. The field flow fractionation (FFF) with light scattering was tested for different particle materials and shapes. For the visualization of the synthesized particles and inverse opals, scanning electron microscopy (SEM) was the main characterization method. And finally, the optical information, which is essential for radiative cooling materials, was measured with UV/Vis and IR spectroscopy.

1.5.1 Simultaneous thermal analysis

STA is a combined method of differential scanning calorimetry (DSC) and thermogravimetry (TGA). This has the advantage that the events of both measurements can be accurately correlated with each other due to the same test conditions (e.g. same sample, thermal contact to the sample crucible and sensor, same test parameters). On the other hand, compromises in the instrumental design reduce the sensitivity of the measurements in comparison to individual analysis. Both methods are briefly discussed in the following section.

DSC can determine the energy and precisely the energy flow into or out of a material. A variety of materials can be analyzed, for example, polymers and composites or inorganic materials, like clay and minerals. When energy flows into or out of a material, it is usually a response to a temperature change. By heating and cooling the material in a controlled manner, the DSC measures the corresponding energy as a function of the temperature. The heat flow can be described as the product of the heat capacity of the sample and the scan rate:

$$\frac{\mathrm{d}q}{\mathrm{d}t} = mc_p\frac{\mathrm{d}T}{\mathrm{d}t} \tag{1.16}$$

Temperature induced transitions can be sensitively measured with DSC, among the most important transitions are the glass transition (T_g), re-crystallization, and melting. The specific heat capacity c_p is defined as the necessary amount of energy that is needed to heat one gram of the material one degree Celsius. c_p measured by DSC is an absolute quantity. Three scans have to be conducted with identical measurement conditions. An empty pan baseline run is subtracted from the sample measurement data between isotherms, and the height of the remaining curve is compared to a standard material like sapphire.[157]

When both, the sample and the reference pan, are heated in the same furnace, it is described as heat-flux DSC. The encapsulated sample and the empty reference crucible are placed on two separate temperature sensors. If a transition occurs within the sample in the heating process, the temperature will be different compared to the reference. For instance, an endothermic transition demands more energy in the sample, which leads to a negative temperature difference to the reference.[158] The temperature difference is proportional to the heat flow:

$$\Delta T \sim \frac{\mathrm{d}q}{\mathrm{d}t} \tag{1.17}$$

A specific cell constant k is experimentally determined with a calibration of standard materials (primarily metals or salts). This is necessary for the conversion of the temperature difference to a power signal.

$$k\Delta T = \frac{\mathrm{d}q}{\mathrm{d}t} \tag{1.18}$$

TGA is used to measure differences in mass dependent on temperature or time. With this method, physical phenomena like phase transitions and ab- or desorption

can be analyzed just as chemical properties, e.g. thermal decomposition or solid-gas reactions (oxidation, reduction). These can be influenced by the atmospheric environment or the used time-temperature method. Thermal analysis can be used to determine the composition of materials quantitively. A typical TGA curve of a polymer consists of the vaporization of highly volatile compounds (solvents, monomers), the polymer decomposition, and the burning to soot and residues (ash, filling material).[159]

With the combination of two analysis methods, it is necessary to know what material properties should be highlighted. Special crucibles out of platinum/rhenium with high thermal conductivity are advantageous for high-temperature DSC measurements, whereas standard alumina pans are sufficient for thermal degradation analysis. A typical measurement with a heating rate of $20\,\mathrm{K\,min^{-1}}$ in air atmosphere is depicted in Figure 1.10.
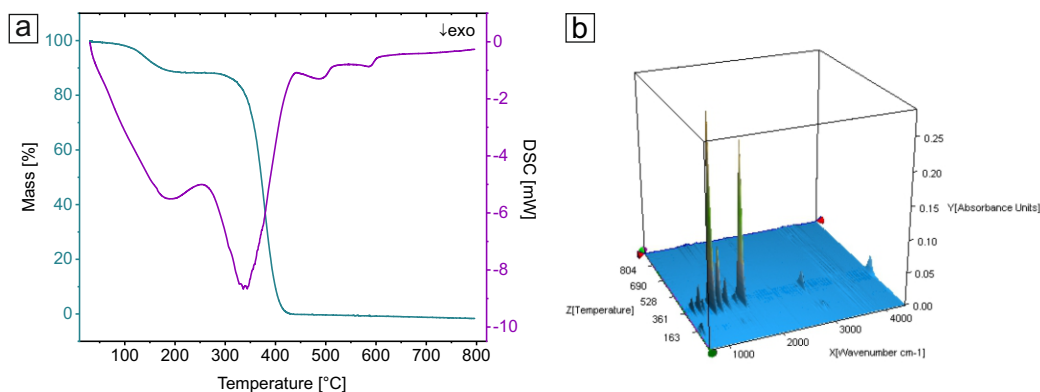
Figure 1.10.: a. STA analysis of PMMA with preceding dissolution in toluene. b. The corresponding IR analysis of the gaseous species, which are produced during the decomposition of the sample.

The analyzed sample was a piece of PMMA, which was dissolved in toluene and dried beforehand. The mass signal shows two steps in degradation. The first one can be associated with the vapor deposition of incorporated water or toluene, and the second one represents the decomposition of PMMA. In the DSC signal the corresponding exothermic transitions are visible. Additionally, the gaseous species can be analyzed with a supplementary FT-IR device (see Figure 1.10.b). The IR spectra can be correlated with the mass losses in the heating segment. In this case, toluene and MMA were identified. This clearly shows the benefits of this measuring technique: the direct correlation of the simultaneous measurements and the unambiguous assignment of decomposition and desorption events based on the additional spectroscopic analysis.

1.5.2 Field flow fractionation

Field flow fractionation (FFF) is a highly customizable fractionating technique for colloidal objects, where separation is achieved through the interaction of the sample with an external physical field.[160] In comparison to other chromatographic techniques, with FFF the sample does not interact with a stationary phase and avoids undesired enthalpic interactions with column materials. The range of particle sizes and molecular masses is from 1 nm to 1000 μm and $10^3 - 10^{21}$ Da, respectively. The most common FFF techniques can be distinguished by the applied external field perpendicular to the solvent flow: Flow-, Centrifugal-, Thermal-, Gravitational- and Electrical-FFF. When several techniques are combined, complex systems with heterogeneous mixtures or broad size distributions can be measured. Applications for FFF are widespread in nanotechnology (pigments, inorganic particles), polymer science (molecular mass, microgel analysis), environmental science (pollen, water analysis), or biotechnology (proteins, cell components).

The technique was first published and invented by J. Calvin Giddings[161,162] and coworkers. They developed a theory that describes the general retention parameters and can be applied to all FFF methods. The separation takes place in a narrow ribbon-like channel with a laminar flow inside the channel. The parabolic flow velocity profile $\nu(x)$ across the channel can be described as

$$\nu(x) = 6\langle\nu\rangle \left[\left(\frac{l}{w}\right) - \left(\frac{l}{w}\right)^2 \right] \tag{1.19}$$

with the average velocity of the carrier liquid $\langle\nu\rangle$, the channel thickness w, and the distance from the accumulation wall l ($l = 0$ at the accumulation wall). This equation can be derived by integration of the Navier-Stokes equation for fluid flow with constant viscosity between two parallel plates. The external field drives the particles towards the accumulation wall at the channel bottom. In return, the particles' natural diffusion (Brownian motion) provides an opposing motion. In an equilibrium state, the particle concentration c can be described as the exponential function of the elevation x

$$c = c_0 e^{\frac{-x}{l}} \tag{1.20}$$

with l represents the average distance of the particles from the accumulation wall. This can be further expressed as

$$l = \frac{kT}{F} \tag{1.21}$$

where k is the Boltzmann constant, T the temperature, and F the force acting on the particles. Therefore, by varying the applied field strength the seperation can be controlled. The retention parameter R can be calculated from the void time t_0 devided by the retention time t_r:

$$R = \frac{t_0}{t_r} \tag{1.22}$$

In practice, three parameters can control the retention time of the molecule or the particle in the channel according to the following relation:

$$t_r \approx Dw^2 \frac{\dot{V}_x}{\dot{V}_{ch}} \tag{1.23}$$

with the particle diameter D, the channel thickness w, the cross flow $\dot{V}_x$, and the channel flow $\dot{V}_{ch}$.

The principle of FFF is schematically illustrated in Figure 1.11. A typical measurement run can be divided into three parts: injection, focusing, and elution. First, the sample is transported into the system by the channel flow. An additional focus flow pumps solvent in the opposite direction to avoid broadening of the sample. Then, the sample is focused at the channel start for a short time. This is used to clean or wash the sample and gain a higher recovery rate. Finally, the focus flow is turned off, and the solvent is only delivered from the main channel pump. The analytes are separated in a dynamic equilibrium between diffusion and the cross field flow. Differences in the diffusion coefficient due to slight variations in the particle size result in different elution times owing to the parabolic flow profile. Depending on the particle size, the particles can diffuse differently away from the channel wall and hence are subject to different flow speeds.[163]

The detection of the eluents is mostly realized via the refractive index (RI), the UV signal, or multiangle light scattering (MALS). The latter is important for the determination of the particle radii or, in more detail, the radius of gyration R_g. In the experimental setup, the laser light is scattered at the particle and detected at 21 different scattering angles. The intensity of the scattered light is proportional to the molar mass. Also, the larger the particles, the more light is scattered in the forward direction. The starting point of the data analysis is the light scattering equation
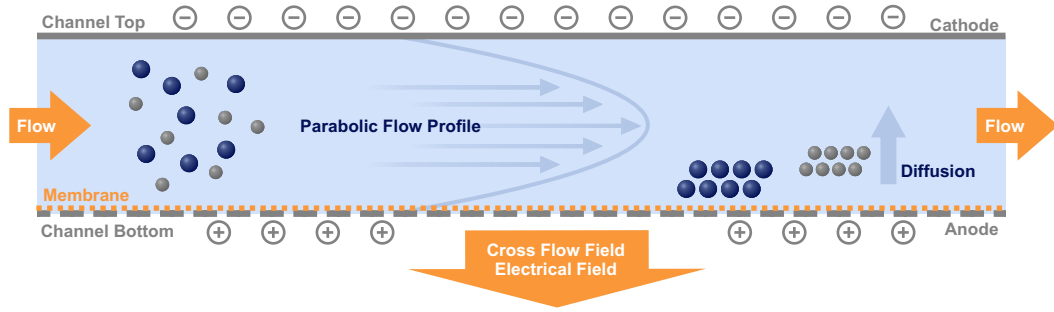
Figure 1.11.: Schematic illustration of the field flow fractionation principle. For the special EAF4 an electrical field can be applied to the channel for seperation according to the electrophoretic mobility (particle charge). This can be used for calculating the Zeta-Potential of the analyzed sample.

$$\frac{R(\theta)}{Kc} = MP(\theta) \tag{1.24}$$

with the Rayleigh ratio

$$R(\theta) = \frac{I(\theta)}{I_0}\frac{r^2}{V},$$

the contrast factor

$$K = \frac{\left(2\pi n_0 \frac{\delta n}{\delta c}\right)^2}{\lambda^4 N_A},$$

the form factor $P(\theta)$, and the molar mass of the sample M. The parameters are: the distance between the light source and the detector r, the scattering volume V, the refractive index of the solvent n_0, the refractive index increment $\frac{\delta n}{\delta c}$, the wavelength of the laser in vacuum λ, and the Avogadro's number N_A.

The angle dependency of the scattering intensity is described by the form factor $P(\theta)$. The different molecule or particle forms lead to different scattering functions and thus, a statement of the geometry of the sample can be inferred. R_g can be calculated by plotting $R(\theta)/Kc$ against $\sin^2(\theta/2)$. This is called the Debye-Plot, which is physically correct for all particles in the Rayleigh-Debye-Gans scattering range. The slope at x=0 represents $\langle R_g^2 \rangle$ and the y-axis intercept results M. For very small particles, the reciprocal Zimm-Plot is a more suitable fit model. Finally, the hydrodynamic radius R_h can be calculated when the geometry of the particle under consideration is known. For instance, for a solid sphere the relation $R_g/R_h = 0.775$ and for a hollow sphere $R_g/R_h = 1.0$ is valid[164]. The hydrodynamic radius can also be measured with an additional online flow dynamic light scattering (DLS) device. The intensity fluctuations caused by the Brownian motion of the particles can be

analyzed over time with an autocorrelation function $G(\tau)$. With the Stokes-Einstein equation[165,166]

$$D_h = \frac{kT}{3\pi\eta D,} \tag{1.25}$$

where η is the viscosity of the solvent and D the diffusion coefficient, the hydrodynamic diameter D_h can be calculated.

For molar mass determination of polymers, the refractive index increment and the extinction coefficient has to be known. Therefor, the RI and UV detectors have to be calibrated with a solution where these material constants and the concentration are acquainted. The area under the output signal peak must be proportional to the total injected mass.
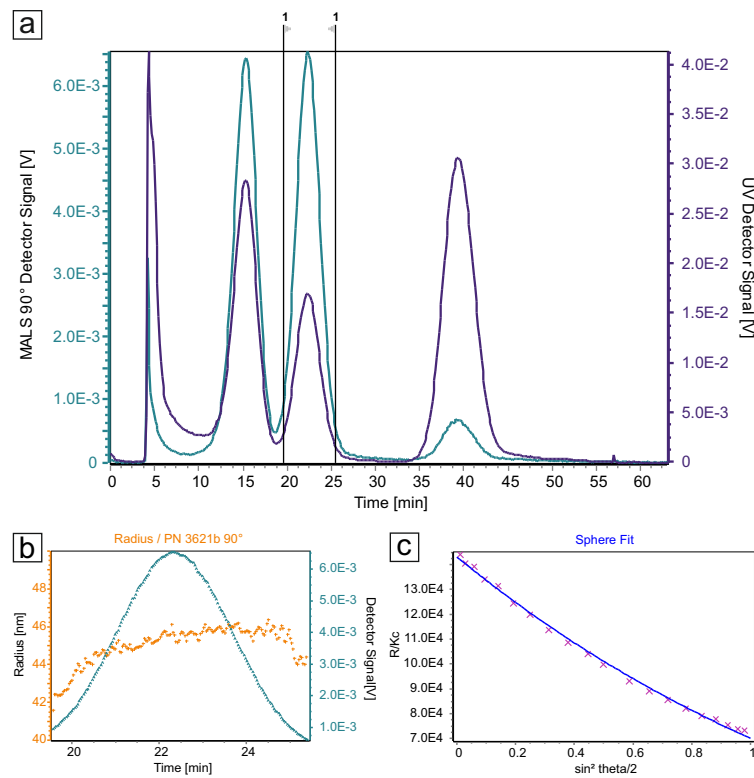
Figure 1.12.: a. Typical FFF elution spectra of a latex particle mixture. The UV- and the MALS 90° detector signal are shown. The first peak at around 5 min elution time represents the void peak, followed by three peaks of different sized particles. b. Particle radius distribution of the marked elution peak. c. The associated Debye plot with a sphere fit.

FFF analysis and evaluation of a standard latex particle mixture (L60 nm, L125 nm, and L350 nm) in water are shown in Figure 1.12. Four different separated peaks are visible in the elugram. The first void peak usually consists of sample

aggregates or solvent additives like salt and surfactants. The size of the distinct particle peaks can then be analyzed according to the above-mentioned theoretical scattering relations. A sphere fit was utilized to the Debye plot of the second elution peak (boundaries are marked in 1.12.a) and the consequent calculation of the radius (see Figure 1.12.b and c). Radii of 23 nm, 45 nm, and 148 nm were determined by the evaluation procedure provided by the manufacturer. After the conversion from R_g to R_h (30 nm, 58 nm, and 191 nm), the values match the given diameters from the standard latex mixture very well. However, an increasing mismatch can be noticed with increasing particle size due to the limitations of the fit model.

1.5.3 Scanning electron microscopy

SEM is an advanced technique to characterize the surface of the materials with high-resolution images and analyze the elemental composition. The basic principle of electron microscopy is comparable to traditional light microscopy. The main difference is, that the image of the sample is produced by scanning the surface with a focused electron beam. The electrons interact with the atoms of the examined material, producing signals with different intensities, which can be combined with the position of the beam to get an image. In comparison to light microscopy, the advantages of SEM are the high resolution in the order of nanometers and the enormous depth of field. Additionally, the image and the chemical composition analysis can be combined to get complex information from the sample.

Electron microscopes were initially developed to improve the resolution of microscopes. The resolution d is defined as the minimum distance between two object points, which can still be distinguished from each other. Ernst Abbe showed that the resolution of optical microscopes is limited by the wavelength of visible light[167] in the Abbe equation

$$d = \frac{\lambda}{2NA} = \frac{\lambda}{2n \sin \alpha} \tag{1.26}$$

with the wavelength of light λ and the numerical aperture NA. NA can be calculated by the refractive index n of the medium in which the lens is working and the maximal half-angle α of the cone of light that can enter or exit the lens. Based on the wave-particle duality, the wavelength of electrons can be described by the de Broglie equation[168]

$$\lambda = \frac{h}{mv} = \frac{h}{\sqrt{2meU}} \qquad (1.27)$$

with the Planck's constant h, the mass m, and the velocity v. The particle momentum in the denominator can also be calculated by extracting the root of the electron mass m, the charge of the electron e, and the electric potential U. As the electrons are accelerated through a potential drop U in electron microscopy, the wavelength of the electrons can be decreased by increasing the voltage. This knowledge led to a significant improvement in the resolution. However, in reality, the actual resolution does not reach the theoretical calculations, due to instrumental limiting factors, like lens aberrations or the electron spot size. Furthermore, the analyzed material can also affect the resolution.

The incident primary electron beam can interact in different ways with the surface layer of the sample, generating the scanning electron microscopy signals. Inelastic and elastic scattering occurs at the atoms when the accelerated electrons enter the material. Backscattered electrons (BSE) result from elastic scattering at the atom nucleus. They are deflected by a Rutherford scattering and thus move with parabolic trajectories. Thereby, the kinetic energy of the incident electron is preserved. Secondary electrons (SE) are generated by inelastic scattering of the primary electrons with electrons of the outer atomic shell. They can be further divided into three groups: SE1 are the direct product of the primary electron beam and the atomic electrons, SE2 result from BSE and atomic electrons, and SE3 are produced by the interaction of BSE with parts of the microscope. In this process, the electrons gradually lose their kinetic energy until they fade out in the sample. When the incident beam removes an electron from the inner atomic shell, a higher-energy electron fills the hole and releases energy in form of characteristic X-rays. With energy-dispersive X-ray spectroscopy (EDS) or wavelength-dispersive X-ray spectroscopy (WDS), the elements of the sample can be identified. The interaction volume, which describes how far the electron beam can penetrate into the specimen, has a droplet-like shape and is illustrated in Figure 1.13. This volume is affected by the atomic number of the component elements or the initial energy of the electrons: the interaction decreases with increasing atomic number and increases with higher acceleration voltages.[169]

The basic arrangement of the components of a SEM is depicted in Figure 1.14. Electrons can be generated with two types of cathode systems, either by thermal emission or with field-emission electron guns. Subsequently, the electrons are accelerated by a high potential between the cathode and anode, which typically lies between 100 V and 30 kV. Tungsten or LaB_6 filaments are appointed in thermal
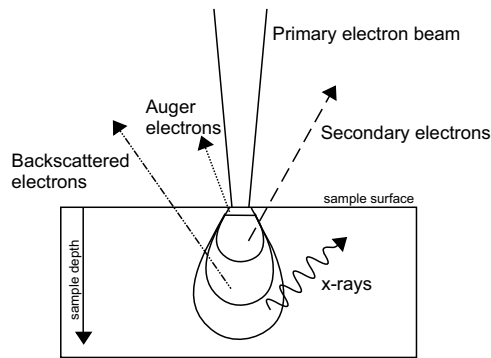
Figure 1.13.: Schematic illustration of the excitation volume resulting from the primary electron beam and the different types of signals generated from the interactions of the electron beam with the sample.

electron guns. Here, the electrons leave the cathode when they received sufficient thermal energy by electric heating. Field-emission guns produce an electron beam with a diameter of 5 to 10 nm and hence are used in high-resolution SEM. These systems have the advantage, that the emitter is not heated and therefore the electron beam has a narrow energy distribution leading to a better resolution. The electrons are generated through quantum tunneling from the tip of a tungsten single crystal by a positively biased extracting electrode. The energy of the electron beam can be adjusted by a second electrode. An additional special type are the Schottky emitters. Here, the tungsten single crystal is coated with ZrO and heated, resulting in a constant and larger beam current.
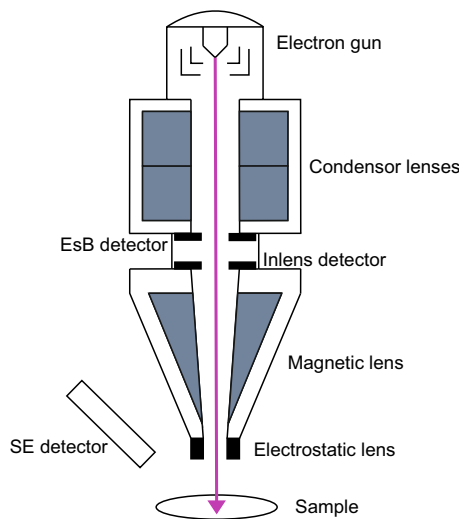

Figure 1.14.: Schematic illustration of a scanning electron microscope.

The accelerated electrons are then guided by electromagnetic lenses through the column towards the sample holder. First, condenser lenses adjust the beam current

and reduce the beam diameter, and finally, the objective lens focuses the electron beam on the sample. However, these lenses cause spherical and chromatic aberrations, which affect the final resolution. Electrons, which enter the magnetic lens field and are inhomogeneously bent, cause spherical aberration. Chromatic aberration is a lens defect originating from electrons with different energies and thus different wavelengths. The most noticeable aberration is astigmatism, resulting from inhomogeneous magnetic fields. This leads to stretching in perpendicular directions relative to a focus point. However, the astigmatism can be corrected with stigmators. The elliptical field distribution of an astigmatic lens can be compensated by quadrupole or octopole electromagnetic coils, which generate an oval instead of a circularly symmetrical field.[170]

The inlens detector is mostly used to detect SE, generated near the spot center. They usually have a low energy and carry the highest spatial resolution information. In combination with small working distances, the detector enables acquiring high-resolution pictures. The detector is located above the objective lens inside the beam path column. The SE2 detector, also called Everhardt-Thornley detector, is placed at the chamber wall, thus viewing the sample in an oblique angle. This is the most common detector because the images convey an impression of the surface topography, due to shading effects and the oblique position of the detector. The electrons are attracted towards the detector by applying a positive potential in the range of 300 V. Thus, high energetic BSEs are not influenced by this field and only those leaving the sample in the direction of the SE2 detector contribute to the signal. At small working distances, the detection efficiency will be reduced, as electrons are more likely attracted by the electrostatic field of the lens, leading to a reduction of the electron yield. The BSE detector is positioned directly under the pole piece. Here, the BSEs generate electron-hole pairs, leading to an electrical current flow representing the detector signal. The detector is separated into different segments, which can be used individually or combined. Depending on the working mode, the compositional or the topographical contrast of the sample can be emphasized. The collected electrons from all detectors reach a scintillator, where their kinetic energy is used to emit photons. These photons are guided to a photomultiplier that finally produces an electronic signal proportional to the number of the collected electrons.

With these various detection possibilities, the range of applications for SEM is quite high. Examples for SEM analysis are depicted in Figure 1.15. Inlens images can be used to determine the size of particles due to the sharp boundaries between the particle and the background. Multiple images can be automatically analyzed with the known image pixel size and an adjustable Matlab circle detection function (inset: green circles).[171] Thus, the particle size distribution of synthesis batches can
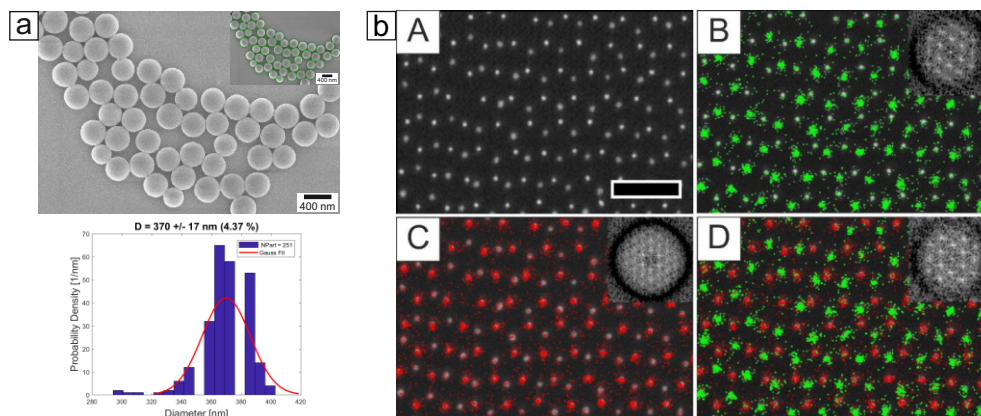
Figure 1.15.: a. SEM image of silica particles recorded with an inlens detector. Such images can be used for particle size evaluation with a Matlab circle detection function (inset: green circles). The resulting size distribution of multiple images with a gaussian fit and the calculated diameter is displayed below. b. SEM analysis (AsB detector) with EDX mapping of hexagonally packed layers of Au@Au-PNIPAM and Ag@Au-PNIPAM colloids forming honeycomb structures. Adapted with permission from „Binary plasmonic honeycomb structures: High-resolution EDX mapping and optical properties", by Honold, T.; Volk, K.; Retsch, M.; Karg, M. *Colloids and Surfaces A: Physicochemical and Engineering Aspects* **2016**, *510*, 198-204.

be easily examined and the quality of the sample can be determined. Information about the chemical composition of materials can be detected with a combination of BSE and EDS analysis (see Figure 1.15.b).[172] The recording of SEM images with an angle selective backscattered electron (AsB) detector, allows the distinction between different metal particle cores (gold and silver). Particles with gold cores appear brighter in the image than the silver particles due to the higher electron density. This is verified with the additional EDS mapping: Au (red dots) and Ag (green dots) emissions perfectly match the positions of the of the particles in the honeycomb structure.

1.5.4 Spectroscopic methods

For a detailed discussion of radiative cooling, it is necessary to get more insight into the spectral properties of the materials. IR spectroscopy shows material properties like the position of the Reststrahlenband, or gives information about the emissivity, because direct (specular), as well as diffuse absorbance or reflectance, can be measured. The same applies to the UV/Vis range. Thus, these methods can help to determine whether a material is a good radiative emitter or cooler.

Infrared spectroscopy. In this analysis method, infrared radiation interacts with matter by absorption, emission, or reflection. Depending on the application, functional groups can be identified for structural elucidation of chemicals, or well-known substances can be quantitatively determined. The IR segment of the electromagnetic spectrum can be further divided into three regions: the high-energy near-IR from approx. 12,500 - 4,000 cm^{-1}, where mostly overtones from OH- or NH-groups can be detected. The classic mid-IR from 4,000 - 400 cm^{-1}, where vibrations of atoms at their molecular bond are excited. And finally, the far-IR (400 - 10 cm^{-1}), where absorption leads to the rotation of the whole molecule or low-frequency vibrations. Generally, absorption of IR radiation leads to vibrational excitation of molecular bonds or rotational excitation of small molecules. The molecule has to be "IR active" for the electromagnetic interaction, which means a changeable or induced dipole moment is required.[173]

According to R. Mecke[174] the mechanical molecule bond vibrations can be divided in stretching and deformation vibrations. Symmetrical and antisymmetrical stretching occurs alongside the binding axis of two atoms or molecule parts by the elongation or compression of the bond. Deformation vibrations involve the change of the binding angle and can be distinguished between scissoring and rocking vibrations (in-plane) or wagging and twisting vibrations (out of plane). Excitations of normal modes from the ground state with a vibrational quantum number $\nu = 0$ to the first excited state with $\nu = 1$ lead to the most fundamental IR bands. An overtone band appears when the absorption of a photon directly leads to a transition from the ground state to the second excited state $\nu = 2$.

The most used IR measurement is the transmission method. According to the sample form (gaseous, liquid, solid), special techniques or measuring cells have to be applied. When measuring foils with parallel boundaries, the spectrum can be distorted due to interferences from multiple reflections. Solids are often embedded in an IR transparent matrix material like potassium bromide (KBr) and pressed into a disc. Strong absorbing samples can be measured in reflection mode. According to Fresnel's equations, the degree of reflection is dependent on the complex refractive index of the material. The attenuated total reflection (ATR) IR spectroscopy is another technique where solids or liquids can be examined directly without further preparation. The IR light is passed through an ATR crystal, which is in direct contact with the sample. The beam undergoes multiple internal reflections, and thereby evanescent waves are formed, interacting with the surface of the sample. Finally, the detector collects the attenuated light beam when it exits the crystal.

In comparison to dispersive devices, where the intensity is measured over a narrow range of wavelengths at a time, with modern spectrometers, the IR spectrum is calculated from the measured interferogram via Fourier transformation. This has the advantage, that spectral data over a wide spectral range can simultaneously be collected, and associated with that, the measuring time is decreased. Furthermore, a better signal-to-noise ratio is achieved due to a throughput advantage using circular apertures instead of thin slits.[175]

UV/Vis spectroscopy. This method is based on the absorption of visible and ultraviolet light of a sample in comparison to a reference or blank sample. Photons in this wavelength range have enough energy to cause excitations of electrons from the ground state to higher electronic energy levels. The energy difference of each pair corresponds to an absorption band. This can be described in the Planck's equation

$$E = h\nu = \frac{hc}{\lambda} \tag{1.28}$$

where E is the energy required to promote an electron from the ground to an excited state, h is the Planck's constant, ν the wavenumber, c the speed of light, and λ the wavelength. The less energy is needed to excite the electrons (the lower energy gap between the HOMO and LUMO), the longer the wavelength of the absorption band. These bands point to the molecular structure of the sample and shift in wavelength and intensity depending on the molecular interaction or environmental conditions. According to the Lambert-Beer law, the transmittance, and therefore the absorbance A, are directly proportional to the concentration of the sample c, the molar attenuation coefficient ϵ and the optical path length l:

$$A = \epsilon l c = \log_{10}\left(\frac{I_0}{I}\right) \tag{1.29}$$

This can also be expressed with the logarithm of the intensity of the incident light I_0 divided by the transmitted intensity I. This can be used to determine the concentration of the absorber in a solution with UV/Vis spectroscopy. Additionally, in reflection mode, it can be revealed how effectively a surface reflects the total amount of incident light. The total reflectance consists of the specular reflectance and the diffuse reflectance[176], which is of particular interest in particle analysis.

For both of these spectroscopic methods integrating spheres can be used for studying

reflectance properties or highly absorbing samples. This tool offers accurate quantitative characterization of reflectance and absorptance of materials. Ideally, the interior surface of the sphere has to be a Lambertian coating, where the radiance is constant in all directions. The spherical shape is necessary for the uniform distribution of light over the entire surface after the incidence.[177] Both transmittance and reflectance can be measured at specific ports on the side and bottom of the sphere. For instance, this could be used for the detection of the scattering contribution of particles in composite materials. Additionally, the general absorptance of the material can be calculated by the energy conservation principle $A = 1 - R - T$, with the absorptance A, the reflectance R, and the transmittance T.[178] The emissivity of an object is equal to its absorptivity at equilibrium for a given wavelength and temperature according to Kirchhoff's law of thermal radiation. The characterization of these properties over the whole UV/Vis and IR range especially helps to estimate wether a material is suitable for passive cooling applications.

Especially in particle systems, IR and UV/Vis spectroscopy can demonstrate even more specific properties due to the huge influence of the topography or compostion of the material on reflection and absorption in these spectral ranges. The reflection in the solar range can, for example, be increased by using titania particles in the material mixture.[179] However, these particles with a high refractive index tend to have high UV absorption. Low refractive index particles suffer from inefficient light scattering.[51] Cheng et al.[180] showed that the spectral emissivity decreases with increasing particle size, but increases with increasing particle volume fraction in the matrix. Furthermore, the emissivity of a material can be tuned by the surface roughness.[181] The particle arrangement can also be used in various ways: randomly packed (amorphous) particles were used to maximize the optical scattering,[51] whereas in an oxidized metallic particle monolayer the emission performance could be improved.[182]

Aim of this thesis

<div style="text-align: right; font-size: 3em; color: green;">2</div>

The experimental fabrication of silicon carbide particles and particle based systems for radiative cooling applications has not been widely reported yet. The focus of this thesis was the synthesis of such specific structured materials in the (sub)micron size range.

Well-defined spherical particles are crucial for applications based on SPhP or passive cooling. However, this shape is in contrast to the most known polymorphic structures of SiC. Commercial SiC powder or SiC particles fabricated by top-down methods consist either of polydisperse small particles with a large size distribution or a non-defined in the meso- and micron scale. A narrow size distribution is also paramount for fabricating functional nanophotonic structures, where the optical properties are governed by particle composition and particle distribution in the composite material. This thesis focuses on bottom-up approaches from silica particles by magnesiothermic reductions or carbothermal reactions, to gain more control over the quality of the precursor particles. Additionally, the influence of a wide range of reaction parameters was examined to gain an understanding of these transformation methods to silicon carbide materials.

Photonic crystals and their respective inverse structures are of great interest and of fundamental relevance for optical devices due to their photonic band gap. Furthermore, they offer tunable colors by the variation of the stop band based on diffraction at the ordered lattices. These properties combined with dielectric materials like silicon carbide could be adapted for radiative cooling and form a new fascinating approach to enhance cooling properties during daytime. Fiber materials are already used for personal radiative thermal management. Due to their scattering properties and their versatile fabrication methods, polymeric or ceramic fiber structures are also an interesting material class for radiative cooling applications.

Distinct particle properties, for example surface charge or particle size distributions, are needed for three-dimensional particle assembly or the characterization of particle additives in radiative cooling composite materials, respectively. Field flow fractionation offers this kind of analysis for particle dispersions, though is less used in the community for studies compared to other chromatographic methods. This work also

features the examination of three special particle systems, which were used to test the versatility of this analysis method.

The thesis is organized into three major parts. In **the first part** possible particle building blocks for radiative cooling composite materials are characterized with field flow fractionation. PMMA, ellipsoidal and PS@SiO_2 particles are analyzed with multiple detector variations to get informations about the size, scattering properties or the zeta potential. Furthermore, the stability of silica hollow spheres after redispersion with different ultrasonication methods is investigated via scattering analysis in FFF. Next, submicron sized spherical silicon carbide particles are fabricated in **the second part of the thesis**. Two fabrication methods - magnesiothermic reduction and carbothermic reaction - are investigated in terms of the shape and the chemical compositon of the resulting particles. The fabrication process is studied with STA, and the particles are examined with SEM and XRD. The optical properties of the particles itself and assembled ones on PMMA films are evaluated by UV/Vis and IR spectroscopy. The **third part of the thesis** focuses on the fabrication of three-dimensional ceramic structures, mainly inverse opals and fibers. Again, the calcination techniques and the resulting superstructures are investigated with optical, thermal, chemical and spectroscopic methods. In general, this work provides insights in the bottom-up synthesis of optically interesting SiC particles and inverse structures. The materials are further analyzed regarding their potential suitability as photonic structures for passive cooling applications.

Particle analysis with field flow fractionation

<div style="text-align: right;">

3

</div>

Field flow fractionation is a highly versatile chromatography method for analyzing particles and macromolecules without the need of a stationary phase. However, characterization with this technique is less common than the standard liquid chromatography methods like size exclusion chromatography (SEC) or high-performance liquid chromatography (HPLC). In the next section, different particle systems are depicted, exceeding separation measurements and focusing on complex and inhomogeneous samples. These materials are of special interest for radiative cooling composite materials, or as building blocks for sophisticated three-dimensional colloidal structures.

3.1 Method development

Although FFF is pretty adaptable, the used separation method has to be adjusted for every single application and sample morphology. Additionally, detectors and other specialized instrumentation have to be selected beforehand to increase the recovery rate of the sample.

A method screening with gentle conditions has to be implemented for an unknown sample. A good starting point are the following parameters: a detector flow of 0.5 mL min^{-1}, a cross flow of 1.0 mL min^{-1} and a linear decay of the cross flow in 20 min to zero. An optimization of the separation method is necessary if the main peak elutes when the cross flow is zero. In this scenario, subfractions can be hidden in the main peak. The cross flow profile can now be changed to a power gradient and the cross flow can be lowered, to shift the main peak into the cross flow decay. By doing so, the system peak at the beginning of the fractogram can get particularly high. This can be modulated by increasing the injection time or by increasing the cross flow. Hence, especially the cross flow is an interlocking parameter and has to be tailored for the samples.

3.2 Particles as gradient materials

Colloidal assembly structures have been widely investigated in sensing applications due to their periodic refractive index modulation.[183] Chemical[184] or environmental[185] triggers can cause changes in the colloidal ensemble, which leads to a shift in the optical stopband and thus a significant color change. More recently, colloidal structures for radiative cooling gained also more attention due to the requirement of colorful surfaces in some applications, like roofing materials or car coatings.[186] Most reports[44,51] focussed on improving the radiative cooling efficiency using white or neutral color to prevent solar absorption. An example for a colorful cooling material was proposed by Kim and coworkers[52] where different sized silica particle opals on PDMS-coated silicon wafers were tested. In the visible region the photonic crystals exhibit iridescent colors resulting from Bragg diffractions. However, in the mid-IR region the structural length scale of the particles becomes negligible, and the opals act as a thermal metamaterial.

Particle gradient materials could be of great interest in radiative cooling materials, as the optical properties, especially in the visible region, can be tuned by using different sized particles or particles with various glass transition temperatures. The optical stopband can be changed by adjusting the periodicity of the structure (change in bandgap), or by altering the refractive index contrast (change in intensity). Particle assembly processes, like monolayer formation or fabrication of colloidal crystals, are usually scalable and cost-effective, but require highly monodisperse samples. FFF is an easy and suitable method to characterize the full particle size distribution of synthesis batches.

PMMA/nBa particles were synthesized by M. Schöttle (Physical Chemistry I, University of Bayreuth). The special synthesis setup[183] allows the continuous production of polymer particles with a very narrow size distribution. Two syntheses were carried out and analyzed with FFF with Millipore water as eluent. Synthesis A and B were segmented into ten and 23 particle batches, respectively. The resulting normalized elution fractograms for the 90° MALS detector angle can be seen in Figure 3.1.a and b.

The elugrams for both syntheses show very distinct elution times for the different particle sizes, which differ in only a few nanometers in size. This highlights the advantage of FFF in measuring even the slightest divergences in the sample geometry. The second batch of gradient particles with more subfractions was measured with the same FFF method, and the differences are still visible without any method adjustments (see Figure 3.1.b). Additionally, the size evaluation with the FFF software is depicted in Table 3.1. For synthesis A R_g values from 71.6 nm to
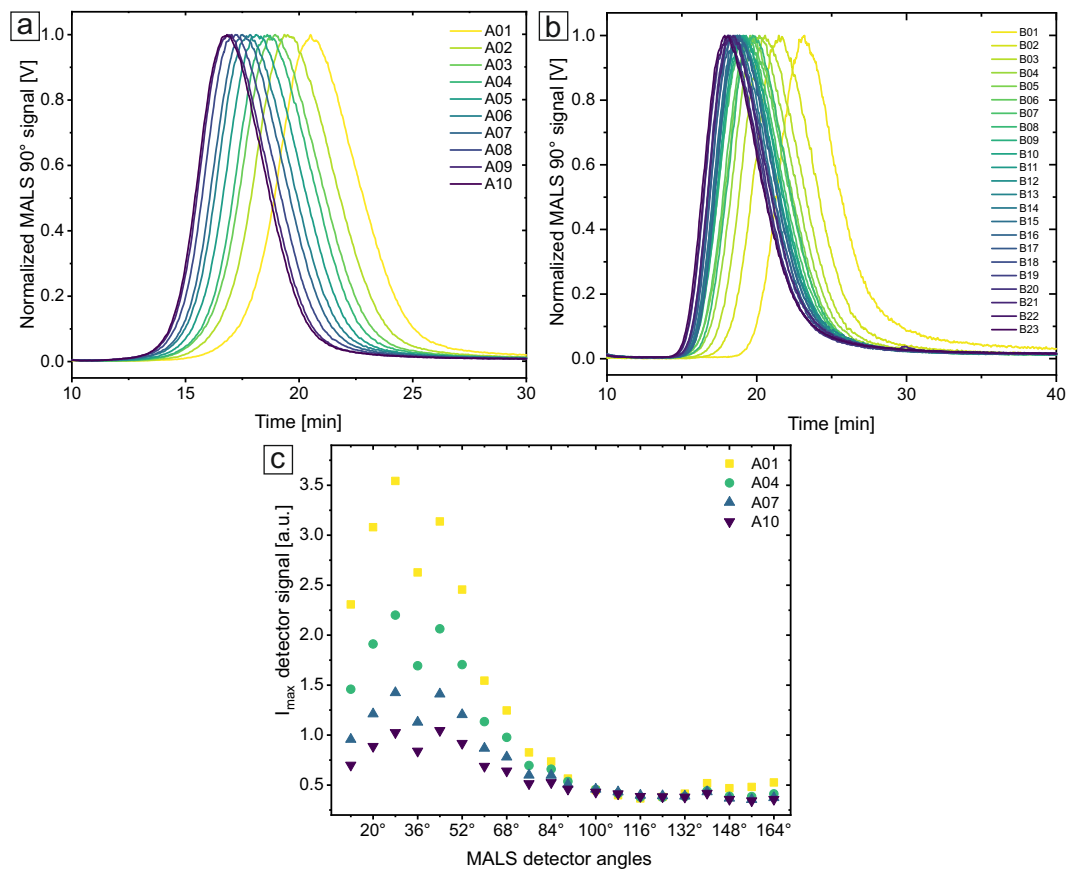
Figure 3.1.: Normalized elution peaks of very narrow distributed PMMA/nBa particles of synthesis A with ten batches (a) and synthesis B with 23 batches (b). c. The maxima of MALS detector signals from 12° to 164° of four samples of synthesis A. Bigger particles (A01) show enhanced forward scattering for smaller MALS detector angles.

100 nm were determined, which results in diameters from 184.8 nm to 258 nm using the relation $R_g/R_{geo} = 0.775$. Synthesis B lies in the same size range from $R_g = 80.5$ nm to $R_g = 111.7$ nm (D = 207.8 nm to 288.2 nm). It can be seen that the absolute size values can indeed be segregated for both syntheses batches. Certainly, some values for the radius of gyration in batch B are very close. For example, B07 with $R_g = 102.8$ nm and B08 with $R_g = 102.4$ nm. The decreasing particle size also matches the shorter elution times of the samples with higher indices. However, it should be noted that the maxima of the elution peaks are not shifted in a linear way, due to the exponential decay of the cross flow in the measuring method. In general, the particle size determination based on FFF can be made with both, the relative elution time and the scattering data of MALS (absolute values). Furthermore, it should be noted that each FFF fraction always yields the full particle size distribution. This is a unique benefit compared to other scattering techniques, which only result in averages, or imaging techniques, like SEM, where the evaluation suffers from bad statistics.

Another interesting measurement feature can be seen when plotting the maximum intensities of the MALS detector signals from multiple angles - the enhanced forward scattering of big particles at small scattering angles is visible (see Figure 3.1.c). Four representative samples of synthesis A (A01, A04, A07, A10) were chosen to show this trend. The maximum intensity at 28° decreases by about 71 % comparing A01 and A10.

Table 3.1.: Particle radii and diameters determined by FFF.

	MALS FFF		
Sample	R_g	R_{geo}	D
	nm	*nm*	*nm*
A01	100	129	258
A02	97.2	125.4	250.8
A03	93.7	120.9	241.8
A04	90.6	116.9	233.8
A05	87	112.3	224.6
A06	83.2	107.4	214.8
A07	79.2	102.2	204.4
A08	75.2	97	194
A09	73	94.2	188.4
A10	71.6	92.4	184.8
B01	111.7	144.1	288.2
B02	109.3	141	282
B03	107.8	139.1	278.2
B04	106.8	137.8	275.6
B05	106	136.8	273.6
B06	105.5	136.1	2722
B07	102.8	132.6	265.2
B08	102.4	132.1	264.2
B09	100.7	129.9	259.8
B10	99.8	128.8	257.6
B11	98.5	127.1	254.2
B12	96.8	124.9	249.8
B13	96.2	124.1	248.2
B14	92.9	119.9	239.8
B15	90.3	116.5	233
B16	89.2	115.1	230.2
B17	86.7	111.9	223.8
B18	85.5	110.3	220.6
B19	83.1	107.2	214.4
B20	82.2	106.1	212.2
B21	81	104.5	209
B22	80.7	104.1	208.2
B23	80.5	103.9	207.8

3.3 Ellipsoidal particles

Asymmetric colloidal particles attracted increased attention because of their promising applications in biotechnology[187], nanotechnology[188] or electronics.[189] The use of non-spherical polymer particles for drug delivery[190] shows the importance of shape-specific micro- or nanoparticle separation techniques. Recently, Jacucci et al.[191] found that anisotropic silica colloids with high aspect ratios outperform the scattering efficiency of their isotropic (spherical) counterparts. Reports with biological[192] or numerical systems[193] already demonstrated the possibility of improved scattering efficiency by using anisotropic building blocks. This phenomenon could also be exploited for radiative cooling materials. The studied ellipsoidal polystyrene particles were synthesized by D. Benke (Physical Chemistry I, University of Bayreuth). Negatively charged PS particles with an original diameter of 326 nm were embedded in a PVA film and uniaxially stretched to three different aspect ratios. The corresponding SEM images are depicted in Figure 3.2.
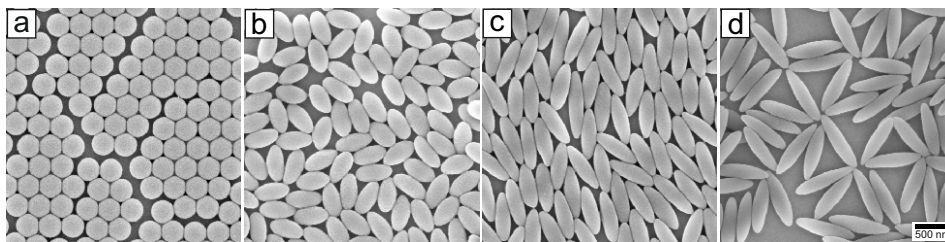

Figure 3.2.: Representative SEM images of the original, spherical PS particles (a) and the corresponding stretched, ellipsoidal particles with aspect ratios of 2:1 (b), 3:1 (c) and 4:1 (d).

First, the influence of the processing conditions was analyzed with FFF, since they probably have an impact on the surface chemistry and the particle stability. The following three samples were measured: the original PS spheres in dispersion; particles, which were mixed with PVA, doctor bladed into a foil and then directly recovered from the foil without heating; and particles, which were embedded in the PVA foil, heated for 1 h at 150 ° C and subsequently recovered from the foil. Note that all three samples are still in their original spherical shape. The resulting elugrams of the FFF analysis with a normalized UV signal can be seen in Figure 3.3.a.

As expected, the original PS spheres show only one individual peak. Interestingly, a second fraction at higher elution times is visible for the other two samples. The main peak of the doctor bladed sample takes 62 %, whereas the second fraction takes 28 % of the area beneath the curve. For the heated sample comparable values
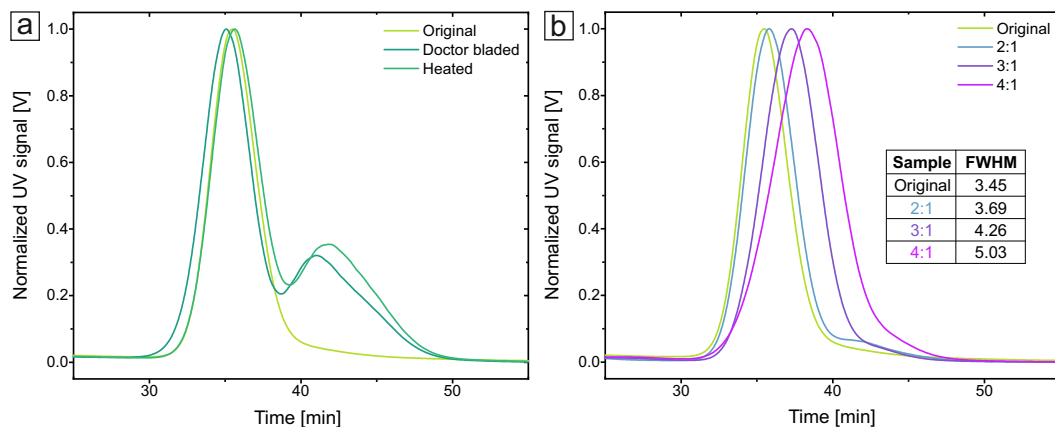
Figure 3.3.: a. Normalized UV signal of the original spheric PS particles, doctor bladed particles and heated particles. For the latter two a second elution peak occurs. b. Elution peaks of the original spheric particles and stretched particles with a ratio of 2:1, 3:1 and 4:1. The FWHM values are shown in the inset table.

were calculated (61 % and 29 %). Thus, around 1/3 of the analyzed material is shifted to higher elution times, indicating a bigger size. Evaluating the peaks by the software to get the corresponding particle size, the main and the second peak of the doctor bladed sample lead to $R_g = 124$ nm (D = 320 nm) and $R_g = 179$ nm (D = 462 nm), respectively. For the heated sample, the values are comparable with $R_g = 127$ nm (D = 328 nm) and $R_g = 170$ nm (D = 439 nm). The original particles have a radius of gyration of 126 nm according to MALS evaluation, which results in a geometric diameter of 325 nm. Hence, the particle diameters of the main peak match the particle size of the original particles according to SEM evaluation (see Table 3.2). The additional fraction is 1.4 times and 1.3 times the size of the main peak for the doctor bladed and the heated sample, respectively. The processing conditions, especially the heating step, apparently lead to the formation of small clusters. However, assuming two particles stick together, the evaluated diameters are too small. This can be explained by using the sphere fit model: particle clusters are no longer spherical, but rather rod-like.

Even after an extensive washing procedure, particles are still not fully redispersed in an individual fashion. The cluster formation can be explained by the relatively high particle concentration in the film (4 % w/w particles in 20 % w/w PVA solution) and thus high possible interparticle contact. This problem could be prevented by decreasing the particle weight fraction and therefore increasing the particle-particle distance in the film. However, the scalability was supposed to be considered in this fabrication method. The mentioned particle/polymer ratio was determined to be the optimum between the cluster formation and the upscaling process.

The elugrams for the stretched ellipsoidal particles are depicted in Figure 3.3.b. Here, the second peak is almost not visible, indicating that most of the possible particle clusters have become separated again during the stretching and cleaning process. The particles with the highest aspect ratio (4:1) also show the broadest peak. This can be explained by the anisotropy of the particles. It is known that non-spherical particles show different retention behaviors in FFF measurements.[194] In normal mode FFF, the elution time is directly related to the radius of the particles. If the cross flow is strong enough to suppress the diffusion, the particles will flow on the channel wall. As a result, particle structures, which enable a closer location to the wall, will elute later.[195] The elution time of the synthesized ellipsoidal particles increases with higher aspect ratios, indicating a normal mode elution. However, non of these models perfectly describe rod-like particle migration due to their unique hydrodynamic interaction with the channel wall and the local average orientation of the particles. Chun et al.[196] proposed two theoretical models for calculating the rod lengths from the hydrodynamic volumes of the particles. First, by calculating the effective translational diffusivity of a rod-like particle averaged over all orientations, or second, by equating a friction coefficient for a sphere and a rod-like particle averaged over all angles. More recently, an improved theoretical model for ellipsoidal particles[197] was proposed but still showed a discrepancy to experimental data. The researchers concluded, that not only the shape but also the surface charge plays an important role in future modulations. Therefore, it is of great interest to synthesize anisotropic particles with high reproducibility and an in-depth surface charge analysis.

In addition to MALS and UV detector signals shown in Figure 3.3.a and b, an online flow DLS measurement was conducted (see Figure 3.4). The peaks resemble the elution peaks of the above mentioned FFF signals. The z-average of the spherical particles (a-c) is constant at ∼374 nm at the main peak and increases up to around 500 nm with the second fraction due to particle clusters. However, the cluster size hardly doubles compared to the individual spheres indicating that only small particle aggregates, such as dubletts, have been formed. Such clusters will not be of an isotropic spherical shape, thus the z-average value could contain errors. This is in good accordance to previous findings in the MALS evaluation. For the ellipsoidal particles (d-f) the size is also increasing at higher elution times, which can indicate an underlying cluster fraction. Interestingly, the z-average value forms a u-shaped dip over the peak with higher aspect ratios. This can be explained by the elongated particle structure: the diffusion process with decreasing cross flow is not yet fully understood and the particles can freely rotate in the DLS measuring cell. It seems that the main particle fraction is around 300 nm, which represents the diameter of
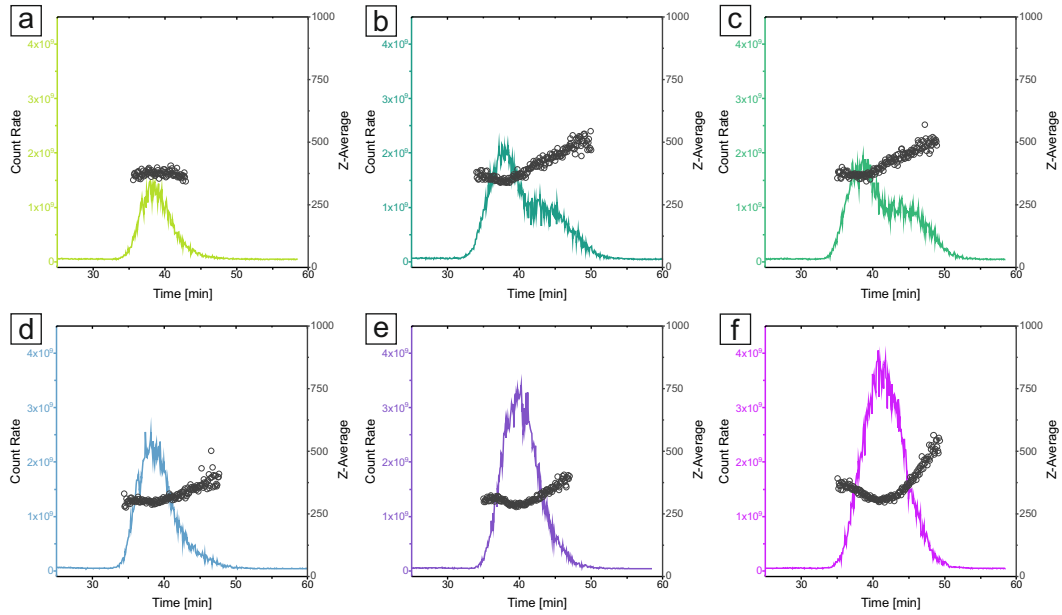
Figure 3.4.: Online DLS measurements for all ellipsoidal related particle samples: the original PS spheres (a), the doctor bladed particle sample (b), the doctor bladed and heated particle sample (c), the stretched particles with an aspect ratio of 2:1 (d), 3:1 (e) and 4:1 (f). The z-average is displayed over the elution peaks.

the original non-stretched particles. This phenomenon can be further investigated in future experiments. For better DLS results, higher concentrations are needed to prevent data scattering[198] and in correlation with that, the FFF measurement method has to be adjusted, too. The evaluated sizes of the particles from SEM, FFF, and DLS are shown in Table 3.2.

To further classify the experimental FFF results, theoretical R_g values for ellipsoidal particles can be calculated according to literature. Detailed formulae for the radii of gyration of ellipsoids and (prolate and oblate) spheroids were summarized by John Satterly.[199] These equations are stated for the rotation about one specific axis. However, in the FFF channel and measurement cells it is more likely, that the ellipsoidal particles rotate in all possible directions. Therefore, the general equation for ellipsoids with semiaxes a, b, and c was selected.[200]

$$R_g^2 = \frac{a^2 + b^2 + c^2}{5} \tag{3.1}$$

The width and length of the elongated particles from the analysis of SEM image were used to calculate a theoretical R_g value, which is shown in Table 3.2. The width was used for both, semiaxes a and b, and the length for semiaxis c.

Table 3.2.: Particle diameters and radii determined by SEM, FFF and online DLS measurements.

| Sample | SEM | | | Online DLS FFF | MALS FFF |
| | Width | Length | R_g(calculated) | D (z-average) | R_g |
	nm	*nm*	*nm*	*nm*	*nm*
1:1	326	326	-	374	126
2:1	254 ± 10	556 ± 22	148	329	172
3:1	230 ± 11	711 ± 35	175	321	149
4:1	211 ± 12	901 ± 47	212	371	140

These calculated R_g values are increasing with higher aspect ratio. In contrast, the radius of gyration is decreasing with higher aspect ratios according to the MALS evaluation with a sphere fit model. This was also already noted in the evaluation of the clusters from the processing conditions. However, comparing the calculated R_g values with the z-average values from DLS, the radius differs in 16.5 nm, 14.5 nm, and 26.5 nm for the sample with an aspect ratio of 2:1, 3:1, and 4:1, respectively. In this case, the average diameter resembles the theoretical one in a good way.

In summary, it can be said that the DLS size evaluation of the ellipsoids approximately resembles the diameter of the original PS spheres. The MALS evaluation delivers R_g, which usually gives smaller values than the hydrodynamic diameter from DLS. For the original, spherical particles R_g matches the diameter from the SEM evaluation almost perfectly. Nevertheless, R_g values for the ellipsoidal particles are too small in comparison to the SEM data due to the utilized sphere fit in the evaluation. The FFF software does not provide a fit model for elongated particles. For more reasonable results a self-made calibration could be made in the future. Otherwise, the stretching of the particles could be monitored by the broadening of the elution peaks and the increased elution time.

3.4 Silica hollow spheres

Silica is widely used for radiative cooling materials, for example, in photonic approaches[18] or polymer-particle hybrid systems.[53] Hollow spheres can provide a large refractive index contrast between the silica shell and the air-filled core, which leads to strong scattering.

Silica hollow spheres were synthesized with polystyrene template particles (D = 262 nm). These particles were coated with silica to obtain core-shell particles with a modified Stöber process. Three different shell thicknesses (15nm, 25 nm, and 35 nm) were realized by adjusting the amount of the TEOS precursor. These PS@SiO$_2$ core-shell particles were analyzed with FFF. The UV detector signal slightly shifts to higher elution times with increasing shell thicknesses (see Figure 3.6.a). The resulting radii from the evaluation of MALS detector signals were compared with the diameter evaluation with SEM (see Table 3.3).

Table 3.3.: Particle diameters determined by EAF4 and SEM.

Sample	EAF4			SEM
	R$_g$	R$_{geo}$	D	D
	nm	*nm*	*nm*	*nm*
PS@SiO$_2$ **A**	120	155	310	293 ± 8
PS@SiO$_2$ **B**	125	161	322	319 ± 6
PS@SiO$_2$ **C**	130	169	338	345 ± 8

There is only a marginal deviation of up to 6 % between the results of FFF and SEM evaluation (5.8 %, 1.1 % and 2.0 % for particle batch **A**, **B** and **C**, respectively). This highlights once more the excellent differentiation between spherical particles in the same size range.

It is possible to measure the zeta potential with the EAF4 by applying an electric field across the FFF channel. The conductivity of the liquid is automatically measured at any time during the analysis to calculate the electrical field strength E.

$$E = \frac{I}{A\kappa} \tag{3.2}$$

with the applied current I, the channel area A, and the conductivity κ. The constant current is defined in the method selection. To calculate the electrophoretic mobility from retention time differences, the sample has to be measured at least two times with different currents. Therefore, a reference measurement without an electric field and measurements with 0.5 mA, 1 mA, and 1.5 mA were performed. The elution graphs for every measurement can be seen in Figure 3.5.
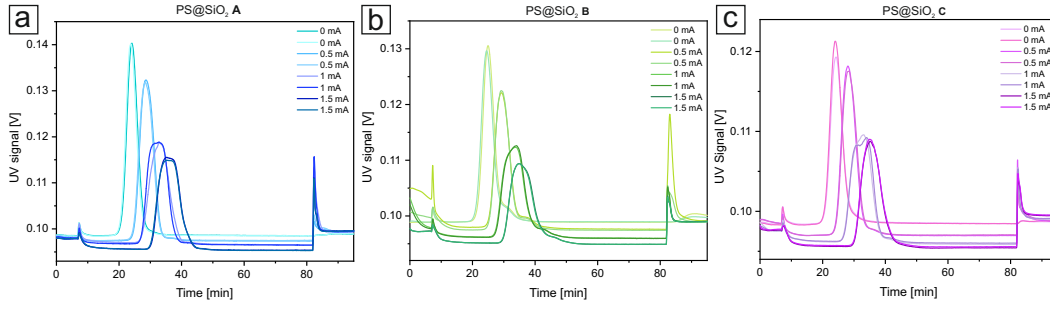
Figure 3.5.: UV signals of all PS@SiO$_2$ core-shell particles with increasing electric current applied to the FFF channel. With higher current the particles stick to the channel membrane and thus the elution time also increases.

The drift velocity and total drift velocity can be calculated for each measurement with the ratio of the cross and detector flow by following equations:

$$\nu = \nu_{\mathrm{c}} + \nu_{\mathrm{em}} \tag{3.3}$$

$$\nu_{\mathrm{c}} = \frac{F_{\mathrm{c}}}{A} \tag{3.4}$$

$$\nu_{\mathrm{em}} = \left[e^{\frac{t_{\mathrm{i}}}{t_0} \ln\left(1 + \frac{fF_{\mathrm{c}}}{F_{\mathrm{det}}}\right)} - \left(1 + \frac{fF_{\mathrm{c}}}{F_{\mathrm{det}}}\right) \right] \frac{F_{\mathrm{det}}}{Af} \tag{3.5}$$

with the total drift velocity ν, the drift velocity induced by the cross flow ν_{c}, the drift velocity induced by the electrical field ν_{em}, the cross flow rate F_{c}, the retention time with an applied current t_{i}, the retention time of a reference measurement without an applied current t_0, the focussing parameter f, and the detector flow rate F_{det}. The electric field strength is then plotted against the total drift velocity for each measurement and a linear fit is applied (see Figure 3.6.b). The slope represents the electrophoretic mobility.

Finally, the zeta potential ζ can be calculated according to following equation:

$$\zeta = \frac{3}{2} \frac{\eta \mu_{\mathrm{em}}}{\varepsilon_0 \varepsilon_{\mathrm{r}} f(\kappa a)} \cdot 1000 \; [\mathrm{mV}] \tag{3.6}$$

with the viscosity of the carrier liquid at 25 °C, the vacuum permittivity ε_0, the relative permittivity of water at 25 °C ε_{r}, and the „Henry's function" $f(\kappa a)$. In the Smulochowski approximation, which is standard for nanoparticles, the value for the Henry's function equals to 1.5.
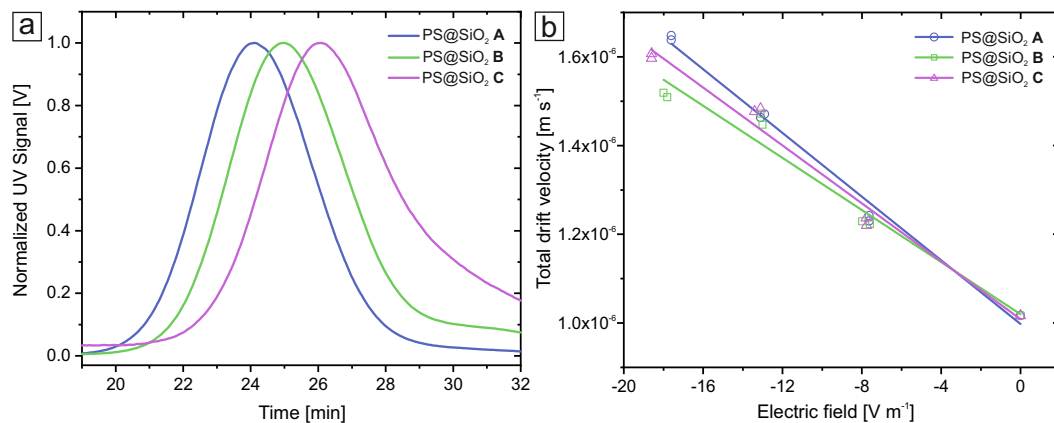
Figure 3.6.: a. Normalized UV signals of the three different sized core-shell particles. Bigger particles are shifted to higher elution times. b. The electric field strength plotted against the total drift velocity for each measurement. The slope of the fitted straight line represents the electrophoretic mobility μ_{em}.

The PS@SiO$_2$ core-shell particles were analyzed in a 1 mM KNO$_3$ solution with a concentration of 0.01 wt.% with the EAF4. These results were compared with a standard ζ-potential measuring setup (Litesizer™500, Anton Paar) and are listed in Table 3.4.

Table 3.4.: Comparison of the electrophoretic mobility μ_{em} and the zeta potential measured with the EAF4 and the Litesizer. All measurements were carried out in a 1 mM KNO$_3$ solution with 0.01 wt.% sample concentration.

| Sample | EAF4 | | Litesizer™ 500 | |
| | μ_{em} | Zeta potential | μ_{em} | Zeta potential |
	$\mu m\,cm\,V^{-1}\,s^{-1}$	$m\,V$	$\mu m\,cm\,V^{-1}\,s^{-1}$	$m\,V$
PS particles			$+1.53 \pm 0.01$	$+19.62 \pm 0.09$
PS@SiO$_2$ **A**	-3.59 ± 0.14	-46.07 ± 1.79	-3.70 ± 0.01	-47.44 ± 0.10
PS@SiO$_2$ **B**	-2.94 ± 0.21	-37.60 ± 2.69	-4.30 ± 0.02	-55.18 ± 0.28
PS@SiO$_2$ **C**	-3.26 ± 0.16	-41.81 ± 2.05	-4.35 ± 0.01	-55.82 ± 0.16

First of all, the original positively charged PS particles have a negative zeta potential after the coating with silica due to hydroxy groups on the surface. The zeta potential is generally an indicator of the stability of colloidal dispersions: the higher the value, the better the electric stability of the particles.[201] With values around 20 mV, like the original positive particles, the stability is incipient, thus the particles still tend to aggregate or flocculate. The core-shell particles almost all have zeta potentials greater than -40 mV, therefore having good stability.[202] For the particle batch **A**

the results for both methods are equivalent, whereas the core-shell particles **B** and **C** show smaller electrophoretic mobilities in EAF4 than with the standard measurement setup. Electrostatic particle-membrane interactions could be a possible explanation for the discrepancy. In general, adding salt should lower the electrostatic interactions in EAF4 measurements. However, it was also noticed that attractive vdW forces gain more importance inside the FFF channel with higher salt concentrations.[203] Unspecific adsorption phenomena between particle and membrane can occur, which influences the retention time and thus the zeta potential evaluation with EAF4 according to equation 3.5. Overall, it is a good additional implementation for the FFF system, and the zeta potential of complicated samples, e.g. antibodies, viruses, charged liposomes, or metal nanoparticles, can be analyzed. Nevertheless, standard zeta analysis has the advantage of shorter measurement times and easier handling.

Afterwards, the polystyrene core was removed by calcination at 450 °C in air to finally produce SiO_2 hollow spheres (HS). The HS were analyzed with TEM and SAXS to confirm the different shell thicknesses (see Figure 3.7 and 3.8).
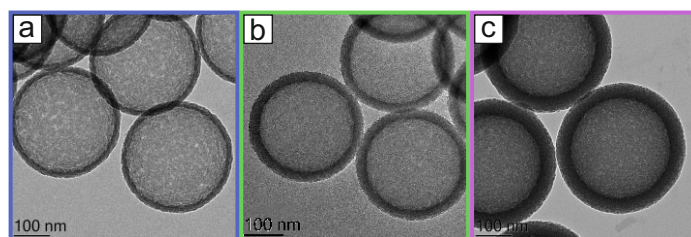

Figure 3.7.: Representative TEM images of the hollow spheres with a shell thickness of 16 nm (a), 26 nm (b) and 42 nm (c).

The evaluation with ImageJ of the TEM images resulted in 16 nm, 26 nm, and 42 nm shell thickness for HS batch **A**, **B** and **C**, respectively. Fitting the SAXS measurements gave similar results with 15 nm, 27 nm, and 39 nm shell diameter. Furthermore, the SAXS data also confirms the narrow size distribution of each sample, which can be inferred from the form factor oscillations shown in Figure 3.8.

The redispersion of hollow spheres is a prerequisite for further processing. An open question in the community is how much the hollow structures are compromised by an ultrasonic treatment commonly used for redispersing. The stability and the fraction of intact hollow spheres are among the most important criteria for the application in innovative materials which have decreased electrical or heat conductivities.[204] So far the standard procedure used for redispersion is a sonication bath operating at 80 kHz. Here, particularly challenging conditions using a sonication tip were tested,
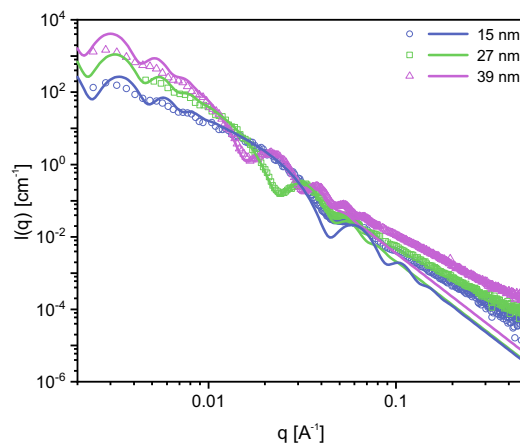
Figure 3.8.: SAXS measurement data (symbols) and the corresponding fit (straight line).

too. Dispersions of HS **A**, **B** and **C** with a concentration of 0.01 wt.% in millipore water were prepared and redispersed in an ultrasonication bath with 80 kHz for two days. Afterwards, the samples were treated with an ultrasonication finger (20 kHz, 50% power, 20% cycle) for 1 min or 6 min. The stability was tested by different redispersion techniques with mild to harsh conditions and subsequent analysis with FFF and online DLS.

The FFF data shows a significant shift to shorter elution times below 15 min for all samples compared to the core-shell particles (see Figure 3.9), where the elution peak maximum was around 25 min. This is probably due to the reduced density of the hollow spheres, which are filled with water.[205] The diffusion of the sample from the membrane is faster than with solid spheres. The shape of the peak also changes from a gaussian shape to an asymmetric form with higher ultrasonication power and longer ultrasonication times. The thin shell of HS **A** gets destroyed more quickly in the redispersion process. Hence, more particle fragments are in the dispersion, which can explain the higher signal at shorter elution times. Interestingly, the UV signal itself increases with higher ultrasonication power and also with a higher shell thickness of the silica HS.

These findings are in good agreement with the DLS data. Here, the correlation function decreases at shorter times for more harsh redispersion methods for all samples. Though only batch **A** with 6 min US treatment also shows a deviation in the shape of the correlation function. This is another hint that ultrasonication has a greater influence on particles with thin shell thicknesses. An evaluation of a specific size distribution was not reasonable due to low sample concentrations (as already mentioned for the ellipsoidal particles) and thus high signal noise.
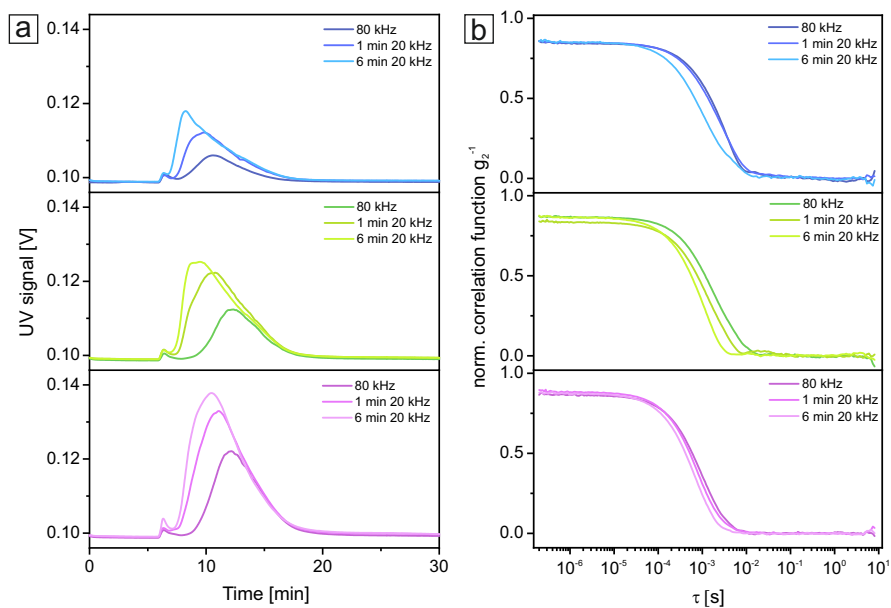
Figure 3.9.: a. UV signal of the hollow spheres **A** (blue), **B** (green) and **C** (pink) with varied ultrasonication treatments. b. Normalized correlation function of the same samples of the online DLS measurement.

To get more insight into this system the FFF MALS data was evaluated and is displayed in Table 3.5. The obtained values for R_g are up to 3.8 times higher compared to the original particle diameter and the diameter of the CS particles at around 300 nm (see Table 3.3). The sizes are decreasing with harsher ultrasonic treatment. Additionally, with increasing shell thickness, the R_g values are overall smaller. This can only be explained by the formation of particle clusters of three to five particles in the calcination or redispersion process. SEM images were made to evaluate the possible damage of the ultrasonication treatment to the hollow spheres (see Figure 3.10). Only for batch **A** particle fragments are visible with both 1 min and 6 min treatment time with the US finger. At harsh conditions, at least some

Table 3.5.: Determined radii of gyration of the analysis of MALS FFF measurement data.

Sample	80 kHz R_g nm	1 min 20 kHz R_g nm	6 min 20 kHz R_g nm
HS **A**	458	455	377
HS **B**	448	388	263
HS **C**	369	279	254

fragments were found in batch **B**. No damage to the hollow spheres was found in sample **C** with the thickest silica shell.

These findings explain the FFF measurement data. Due to the particle clusters the elution time of the hollow sphere samples is strongly decreased compared to the CS particles. The elution no longer takes place in normal mode but rather in steric mode, where large objects elute faster than predicted. Harsher ultrasonication treatment hence destroys the particle clusters. This is in good agreement with the decreasing R_g values and the change of the autocorrelation function of the DLS measurements. The SEM images (see Figure 3.10) show that the hollow spheres with a thin shell are more affected by the treatment and thus damaged than HS with a thicker shell.
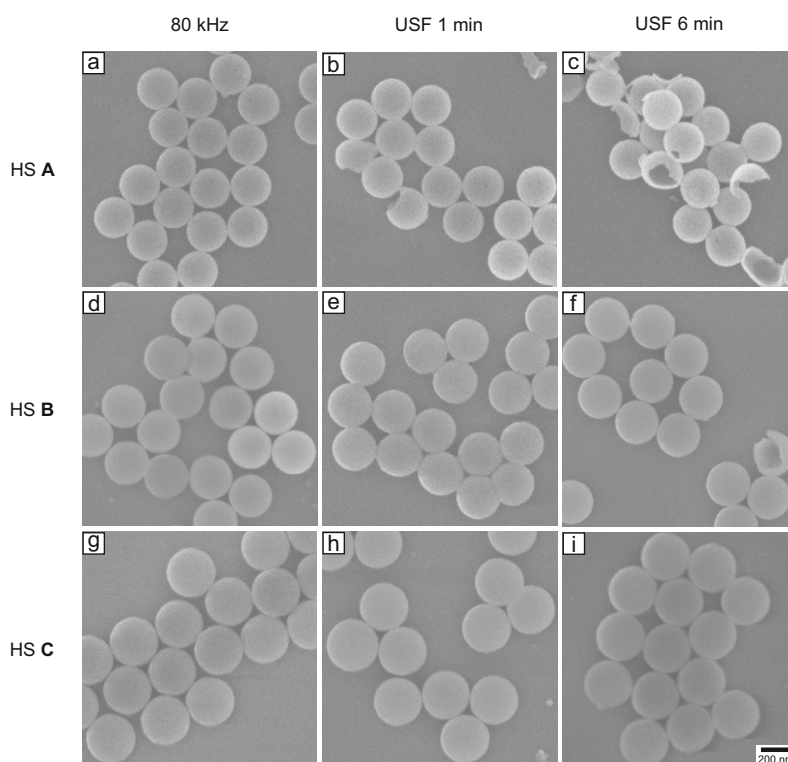
Figure 3.10.: SEM images with high magnification of the silica HS after the ultrasonication treatment with different conditions. Batch **A** (a, b, c), **B** (d, e, f) and **C** (g, h, i) with 80 kHz, 20 kHz ultrasonication finger for 1 min and 20 kHz ultrasonication finger for 6 min in the respective rows and columns.

However, this also indicates that the hollow spheres must be relatively stable, as with the ultrasonic treatment rather the clusters are dispersed than the particles themselves are damaged. Unfortunately, this cannot be quantified with these data. The particles were not fully redispersed after two days in the ultrasonication bath at 80 kHz. This could have been caused by a sintering process during calcination or

particle aggregation during the freeze-drying process. Another shortcoming could have been the usage of plastic centrifuge tubes as vessels for the particle samples in the ultrasonication bath. Compared to glassware, the polymer material can inhibit power transfer into the particle dispersion.

The results show that FFF is a suitable method to analyze and quantify the stability of hollow spheres. The issues with cluster formation could be solved by using low particle dispersion concentrations for freeze-drying or small amounts of the particles in the calcination crucibles. Then the experiments can be repeated, confirming that the treatment with the ultrasonic bath is mild enough to retain the hollow spheres. Up to now, it only can be said that the extent of damage decreases with increasing shell thickness of the hollow spheres.

In conclusion, it was shown that the FFF is a powerful alternative to classic chromatography methods and also capable to analyze (anisotropic) particle samples from a different viewpoint. Three different model systems were investigated and showed promising results for further research. The evaluation of very slight diameter variations in gradient particle samples was successful. Processing parameters for the ellipsoidal particle fabrication were analyzed and accordingly adjusted. It was also possible to differentiate stretching aspect ratios by evaluating the elution peak. Finally, the zeta potential of core-shell particles was measured with FFF and compared to a standard device. A possible method was also presented to validate the fractions of intact and destroyed silica hollow spheres.

Particles

<div style="text-align: right">4</div>

4.1 Synthesis of silicon carbide particles

This section describes the synthesis of silicon carbide particles. An overview of the four synthesis routes is given in Figure 4.1.
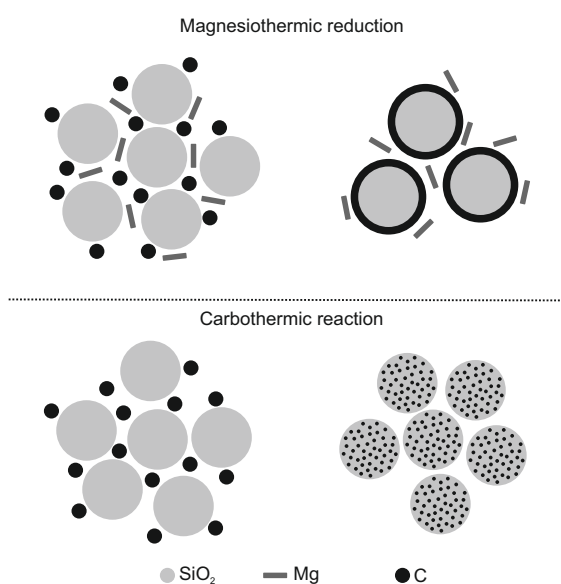

Figure 4.1.: Schematic overview of all investigated synthesis routes to SiC particles.

First, grained mixtures of SiO_2 particles, carbon powder, and magnesium chips, and second, silica-carbon core-shell (CS) particles with magnesium chips were used to prepare SiC particles by magnesiothermic reduction. The carbothermic route was carried out with a mechanical mixture of silica particles and carbon powder or silica precursor particles, where the carbon is evenly and covalently bonded to the spheres.

4.1.1 Magnesiothermic reduction

At first, simple mixtures of the reactants silica, carbon, and magnesium were tested to produce SiC particles according to Dasog et al.[122] The SiO_2 particles with a

diameter of $D = 408 \pm 20\,\text{nm}$ were synthesized beforehand by an adapted Stöber[72] process. These particles were grained with a stoichiometric amount of carbon powder and magnesium chips and placed in an open alumina boat in a tube furnace. After the magnesiothermic reduction at $600\,^\circ\text{C}$, $700\,^\circ\text{C}$ and $800\,^\circ\text{C}$ in Ar atmosphere, the structure was analyzed with SEM (Figure 4.2).
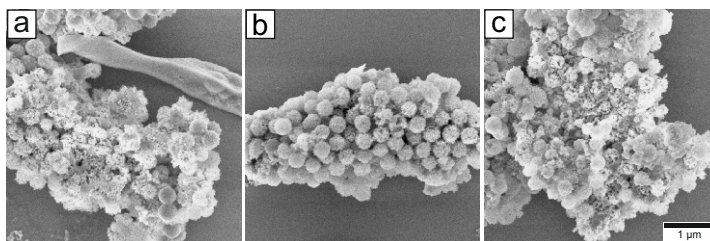
Figure 4.2.: Representative SEM images of the particle samples after the magnesiothermic reduction at $600\,^\circ\text{C}$ (a), $700\,^\circ\text{C}$ (b) and $800\,^\circ\text{C}$ (c).

At all tested temperatures, the shape is rather intact, but the spheres get very porous. Furthermore, some new material is formed in the spaces between the particles, and they are no longer loosely distributed but arranged in clusters. At $600\,^\circ\text{C}$ additional whiskers have formed, which can be seen in Figure 4.2 a. The formation of whiskers in such reactions is reported in the literature. For example Xi et al.[206] converted $SiCl_4$ and 2-ethoxyethanol to SiC nanostructures with Mg at $600\,^\circ\text{C}$ or Zhang et al.[207] produced SiC nanoribbons at high temperatures above $1250\,^\circ\text{C}$ in a reaction of silicon and carbon powder. Overall, the morphology of the synthesized material was not satisfying, intending to form uniform, spherical SiC particles. Nonetheless, XRD measurements were performed to get more insight into the structural composition of the samples (Figure 4.3).

The main signals at $2\theta = 28.5^\circ, 47.4^\circ, 56.2^\circ, 69.3^\circ$ and 76.6° can all be assigned to silicon[208] for all three temperatures. In the sample, which was converted at $700\,^\circ\text{C}$, some additional MgO peaks[209] at $2\theta = 36.9^\circ, 43.0^\circ, 74.9^\circ$ and 78.8° are visible. This can be explained by a non-sufficient cleaning step. Additionally, it seems that the signals have an increased intensity for higher temperatures, indicating more crystalline structures and higher conversion of the reagents.

Temperature, gas flow, pressure, and stoichiometry are very crucial parameters in this reaction. Ahn et al.[117] investigated the selectivity between silicon and silicon carbide of the magnesiothermic reduction in SiO_2/C composites. They found out that the Si/C interface plays an important role which material is synthesized. According to that, the mechanical mixtures of grained silica particles, Mg turnings, and carbon powder have probably not enough points of contact to successfully
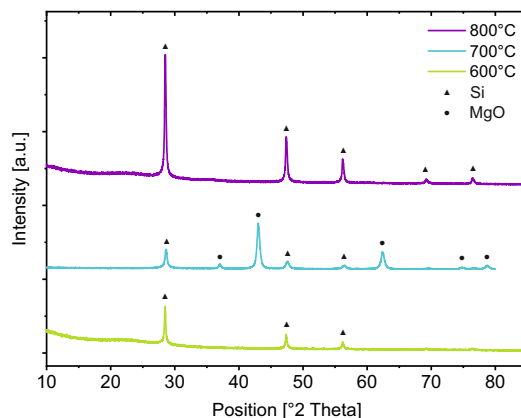
Figure 4.3.: XRD spectra of the particles after magnesiothermic reduction at 600 °C, 700 °C and 800 °C. The peaks are identified as silicon and MgO residues.

convert the reactants to SiC. To increase the Si/C interface, core-shell particles were synthesized in the next step.

The first batch of core-shell particles SiO_2@C **A** with a particle diameter D = 198 ±22 nm (σ= 11.28 %) was synthesized according to Fuertes et al.[210] The originally produced organic resorcinol-formaldehyde shell was converted to carbon in a pyrolysis step and is around 30 nm thick. The SEM images and the particle powder before and after the pyrolysis, where a color change from brown to black can be seen, are depicted in Figure 4.4.

The second batch SiO_2@C **B** with a bigger particle diameter D = 370 ± 17 nm (σ= 4.37 %) was synthesized according to Guan et al.[211] Here, the carbon source was also a resorcinol-formaldehyde resin, which was later pyrolyzed. The produced carbon shell was around 40 nm thick and is depicted in Figure 4.5.

To get a more detailed insight into the thermal conversion process, the magnesiothermic heating steps were conducted in the STA, allowing the analysis of the DSC and the mass loss signals. The small CS particles SiO_2@C **A** were mixed with Mg
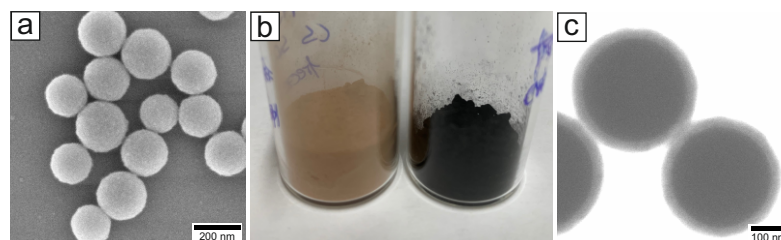
Figure 4.4.: a. Representative SEM image of the CS particles SiO_2@C **A**. b. Photograph of the CS particles before (left) and after pyrolysis (right) c. STEM image of the particles, where the carbon shell can be seen.
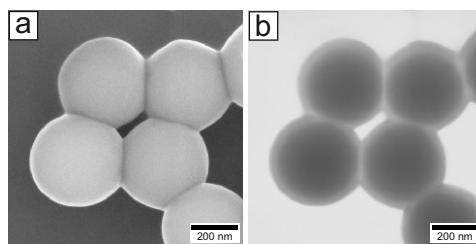
Figure 4.5.: SEM (a) and STEM image (b) of the same CS particles SiO$_2$@C **B**. In the STEM image the carbon shell can clearly be seen.

turnings in a 1:1 weight ratio and heated up to 600 °C, 700 °C, 800 °C and 900 °C with a heating rate of 5.5 K min^{-1} in alumina pans with a lid in nitrogen atmosphere. It should be noted that in the combined STA measurement, the accuracy of the DSC signal suffers when using Al$_2$O$_3$ instead of aluminum pans compared to standard DSC measurements. In general, the high thermal conductivity of the pan material enables optimal heat transition between the sample and the sample holder. In the conducted temperature range and with respect to critical reactions of platinum pans with the sample material, alumina crucibles represent a good compromise. The resulting measurements are shown in Figure 4.6.

In the DSC signal, an exothermic signal can be seen in the heating segment. With increasing temperature, this peak gets larger and broader. However, the material conversion process starts at 600 °C in either case. At 645 °C a distinct endothermic signal is visible, which represents the melting temperature of magnesium. The exothermal conversion is driven by the oxidation of Mg to MgO. No additional signal is found in the attached long isothermal segment at the final temperature. Interestingly, the mass loss signal shows a slight and steady decrease at the beginning of the heating segment and then an increase in weight of around 10 % for all different temperatures. The loss of weight can be explained by the release of water inclusions or residues. The increase in weight is in contrast to the expected possible side reactions. Gaseous carbon monoxide or carbon dioxide can be formed[212] and leave the system, which results in a decrease in weight. Shi et al.[213] reported an increase of weight in the TGA analysis of silicon carbide due to the oxidation of the material in air atmosphere. However, the displayed measurements were conducted in a nitrogen atmosphere. The rise of the mass signal is superimposed with the endothermic melting signal of magnesium. This can only be explained by an unwanted side reaction of the melted, metallic magnesium with the nitrogen gas at elevated temperatures.[214]

$$3\,\mathrm{Mg} + \mathrm{N_2} \longrightarrow \mathrm{Mg_3N_2} \tag{4.1}$$
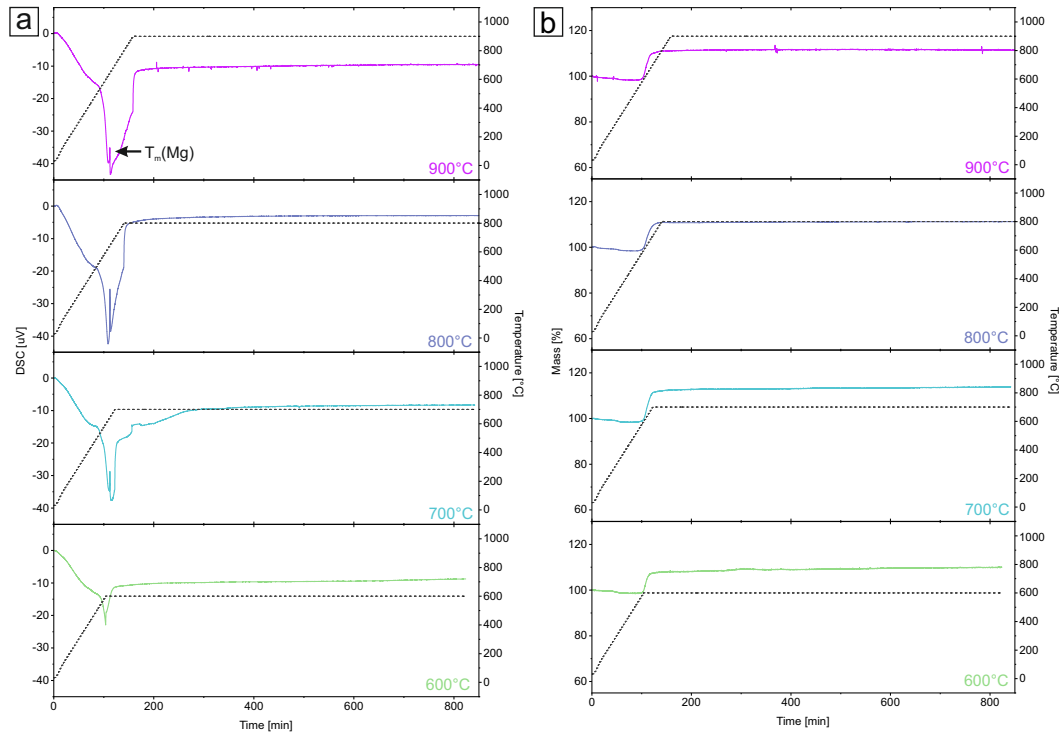
Figure 4.6.: DSC signals (a) and mass signals (b) of the magnesiothermic reductions from 600 °C to 900 °C (bottom to top).

The resulting powders were subsequently analyzed with XRD (Figure 4.7) to confirm these findings. As in the first magnesiothermic reduction test, most of the signals can only be assigned to pure silicon and MgO residues from the side reaction. Note, that these samples were not cleaned after the reaction due to the small amount of sample in the STA crucibles. Hence, the big signals at $2\theta = 37.0°, 43.1°, 62.6°, 74.8°$ and $78.9°$ match the crystalline information of MgO[209] and the signals at $2\theta = 28.5°, 47.7°$ and $56.5°$ are assigned to silicon.[215] Additionally, three small signals at $2\theta = 33.9°, 35.7°$ and $52.3°$ can be assigned to magnesium nitride.[216] This supports the data of the increasing weight signal in the STA measurements. Again, silicon carbide was not formed with the magnesiothermic reduction at different temperatures, even with the enhanced silica and carbon interface. However, these experiments showed that the nitrogen atmosphere clearly has a strong influence on the reaction outcome.

Liu and coworkers[217] showed the manipulation of the phase and microstructure of SiC in a molten salt synthesis. The salt acts as a liquid environment for the reactants to enhance the diffusion process and to suppress heating spots. SiO$_2$@C **B** particles were mixed with magnesium chips and NaCl in a weight ratio of 1:1:10. Furthermore, one sample batch with extra carbon powder (weight ratio CS particles:Mg:C = 1:1:1) was mixed. These batches were again analyzed with the STA at 800 °C
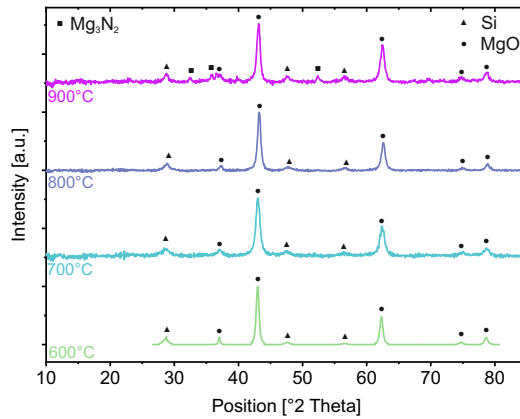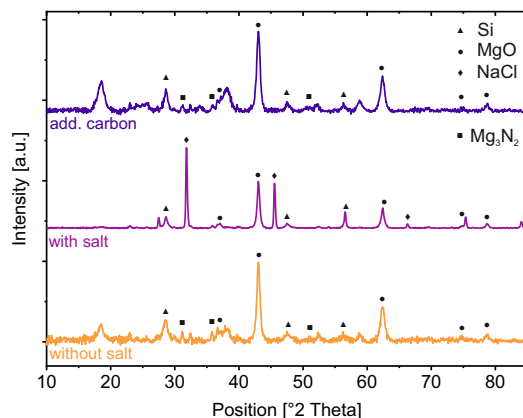
Figure 4.7.: XRD measurements of the particles after the heat treatment with magnesium. At all temperatures the peaks can be identified as silicon and MgO. For the sample, which was converted at 900 C, some small peaks can be assigned to Mg_3N_2.

with the same method parameters as already mentioned above. The results are shown in Figure 4.8 in comparison to the „standard"conversion without any added reactants.
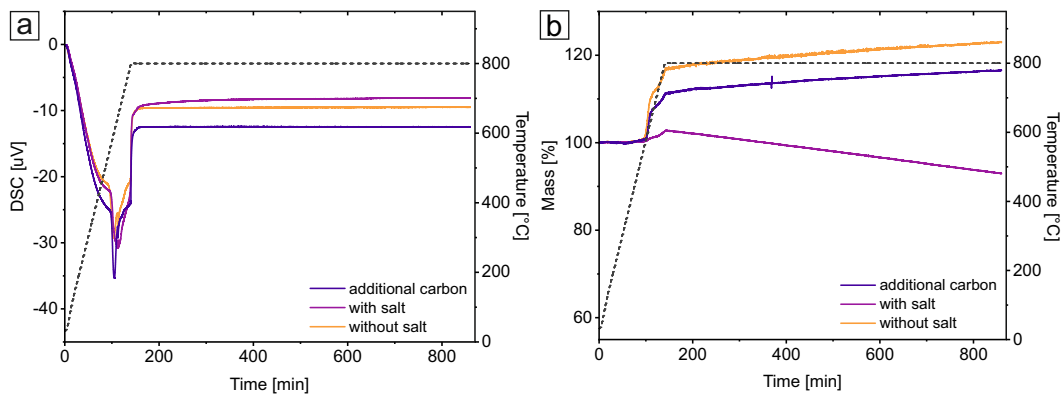
Figure 4.8.: DSC signals (a) and mass loss signals (b) of the magnesiothermic reduction of the CS particles at 800 °C with additional carbon, in a NaCl salt melt and for comparison the „standard"synthesis route without salt or additional carbon.

A similar shaped, exothermic transition can be seen for all variations of the magnesiothermic reduction in the heating step for the DSC signal. This is probably caused by the formation of magnesium oxide. In the reaction with additional carbon, the peak is more distinct than with the other two samples. In the isothermal segment, no other transition can be found. The mass signal shows again a behavior, which can only be explained by a reaction with the surrounding gas atmosphere. Starting at around 600°C and with further approaching the end temperature of 800°C, the mass steeply increases with up to 20 % more weight than the initial weighed portion

Figure 4.9.: XRD measurements of SiO$_2$@C **B** particles after the heat treatment with additional carbon, in a NaCl salt melt and without salt. The peak signals can be assigned to silicon, MgO, NaCl, and Mg$_3$N$_2$.

for the sample without salt. This hints once more to the formation of Mg$_3$N$_2$. The sample with additional salt is the only exception because, after a short increase, the mass decreases till the end of the measurement time. Maybe the sodium chloride suppresses the diffusion of N$_2$ to the Mg inside the crucible by forming a liquid salt environment and thus hinders the reaction to magnesium nitride.

The following XRD evaluation showed various signals for all three variations (see Figure 4.9). The samples consist of different materials, and not all signals could be evaluated. Also, due to the small sample weight for the reaction in the STA, the products were not cleaned, leading to possible superimpositions of the signals. Peaks at $2\theta = 37.1°, 43.0°, 62.4°, 74.8°$ and $78.8°$ can be assigned to MgO[209], whereas peaks at $2\theta = 28.7°, 47.5°$ and $56.5°$ match the signals of silicon.[215] In the reaction with the additional salt, signals at $2\theta = 31.9°, 45.5°$ and $66.4°$ can be assigned to NaCl. Small signals resulting from magnesium nitride at $2\theta = 31.1°, 35.8°$ and $51.6°$ can be found in the samples with additional carbon and without salt. This matches the inference from the STA evaluation. No match with silicon carbide was found.

Finally, the small core-shell particles SiO$_2$@C **A** were transformed at 800°C in the molten salt with the exact same parameters as already described above, but in a tube furnace in Ar atmosphere. Here, the general sample weight was much higher in comparison to the performed measurements with the STA - around 100 mg compared to ~5 mg, respectively. After the heat treatment and a cleaning step with hydrochloric acid and water, the sample was characterized with XRD and SEM (Figure 4.10).

The signals at $2\theta = 35.8°, 41.4°, 60.1°, 71.9°$ and $75.4°$ can be assigned to silicon carbide. The low-intensity peak at $\theta = 33°$ occurs due to stacking faults. Additionally,
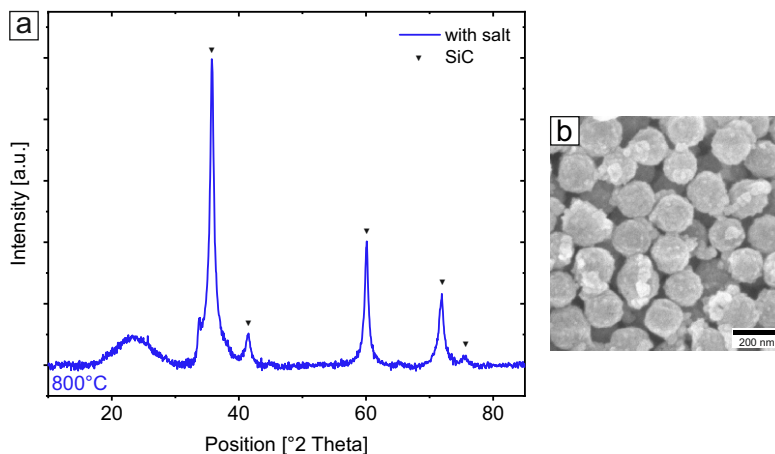
Figure 4.10.: a. XRD measurement of the small CS-particles in a NaCl salt melt The main peak signals can be identified as silicon carbide. b. Representative SEM image of the produced particles.

the signal at around $\theta = 22°$ represents an amorphous phase. Spherical particles with a rough surface and additional adhered small crystals are visible in the SEM image. The size analysis with ImageJ leads to an average diameter of $D = 160 \pm 12$ nm. Hence, the particles shrink by around 18 % compared to the original core-shell particles. This can be explained by the release of gaseous species (e.g. CO) and the transformation change of an amorphous to a crystalline material, leading to a higher density. The results show that the change of the inert gas (from N_2 to Ar) greatly influences the synthesis. Here, the reactant mixture resulted in the formation of SiC, whereas the same particles, which were converted with the exact same conditions in the STA, formed only silicon, MgO, or Mg_3N_2 from side reactions. Furthermore, the higher sample weight can also regulate the formation of the thermodynamically favored SiC by a higher encounter chance of Si intermediates and carbon.[117]

In conclusion, the magnesiothermic process showed many problems in producing submicron-sized SiC particles. With the realized experiments, especially with the focus on the last-mentioned successful conversion from SiO_2@C to SiC particles, some insights and conclusions can be made. The interface of silica and carbon is a very crucial point. The loosely mechanical mixtures did not lead to SiC, whereas this problem could be overcome with the core-shell particles. However, the unsuccessful experiments, where mainly silicon is formed, display the stoichiometry problem. It is mentioned in the literature that the ratio of Si and C is decisive whether silicon carbide is formed in the reaction or not. The ratio of silicon and carbon was approximately right with the small CS particle batch **A**, whereas with the bigger ones **B** the carbon shell was not thick enough. Another huge mismatch was found by using different furnaces with different inert gas atmospheres and sample volumes

(STA vs. tube furnace). This was kept in mind for the carbothermal approach as well. Overall, it was possible to synthesize SiC particles with a magnesiothermic reduction in a specific size range below 200 nm. This process could be optimized in the future.

4.1.2 Carbothermic reaction

At first, simple mixtures of silica particles and carbon powder were transformed with the carbothermal approach. The SiO_2 particles were again synthesized with the well known Stöber process[72] and had a diameter of D = 618 ± 75 nm (σ= 6.86 %). The particles were mixed with carbon in a molar ratio of 1:3 and 1:5, homogenized in a mortar, and heated to 1500 °C with a heating rate of 300 K h^{-1} in argon atmosphere for 10 h in open alumina crucibles. After the reaction, the powder was analyzed with XRD and SEM (see Figure 4.11).
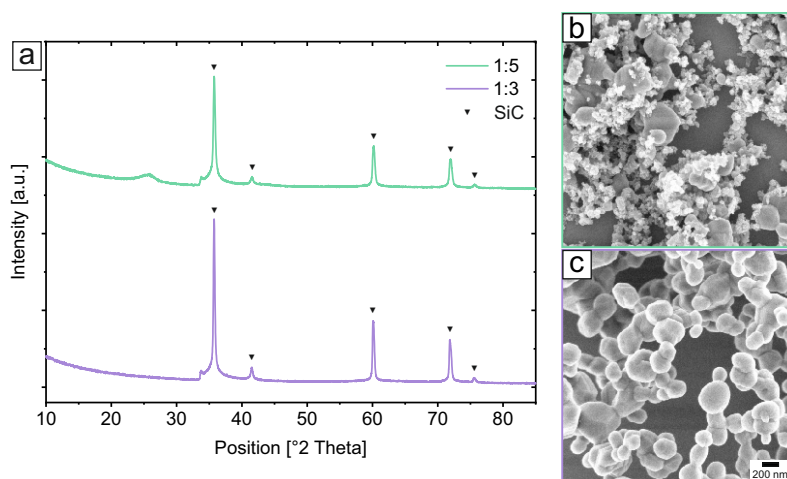
Figure 4.11.: XRD measurements (a) of the particles after the carbothermic reaction at 1500 °C with two different mixing ratios of silica particles to carbon powder. All signals can be assigned to silicon carbide. Representative SEM images of the samples with a mixing ratio of 1:5 (b) and 1:3 (c).

In both reaction variations the XRD signals at $2\theta = 35.8°, 41.5°, 60.2°, 71.9°$ and $75.6°$ can clearly be identified as SiC (β-SiC, cubic, Moissanite).[218] In the sample with the 1:5 silica/carbon ratio, a small amorphous peak at around 25 ° can be seen. This can be explained by an excess amount of amorphous carbon powder, as the silica/carbon ratio is probably too high for a stoichiometric conversion. This is also in accordance with the SEM images showing small crystalline grains and additional powders, which can be attributed to carbon. Otherwise, the spherical shape of the initial particles is completely lost in the transformation process. Overall, the reaction

transformed silica into SiC, but maintaining the spherical shape was not successful. Again, this underlines the importance of an intimate mixture of silica and carbon.

Synthesis of the SiO$_2$-precursor

With the knowledge gained from previous magnesiothermic experiments, it is necessary to enhance the silica/carbon interface since enough carbon must be near the silicon atoms to hinder the formation of other derivates like pure silicon. Accordingly, silica particles with covalently bonded phenyl groups were synthesized based on the work of Hatakeyama[114] and Seog.[115] Phenyltrimethoxysilane (PTMS) was used as an additional ingredient in the sol-gel reaction and hence integrated into the silica network. The phenyl groups later serve as the carbon source for the subsequent pyrolysis step. With the standard Stöber process, the resulting particle size can be adjusted by varying the TEOS concentration. The influence of the reactant concentrations was investigated with small reaction batches of 15 mL. Changing the TEOS concentration showed a strong influence on the resulting particle size. At c = $0.125 \, \mathrm{mol \, L^{-1}}$, a bimodal distribution with a significant difference in mean particle diameter (150 nm vs. 1000 nm) was obtained. Quite notably, however, an upper limit of particle evolution exists at about $c_{\mathrm{TEOS}} > 0.4 \, \mathrm{mol \, L^{-1}}$, beyond which gelation occurs. Size control in this reaction is hard to achieve: for low TEOS concentrations, particles with several 100 nm in diameter are obtained, at intermediate TEOS concentrations, small beads of a few 100 nm are accessible, and at high TEOS concentrations, no particle formation is observed. Besides this, the resulting particle size is relatively insensitive to changes of the other reactants. Changing the concentrations of water, PTMS, and ammonia does not influence the final particle size. The diameter variations of the precursor particles are shown in Figure 4.12.

PTMS clearly influences the particle condensation kinetics. A potential reason could be the different kinetics of the alkoxy- (TEOS) and organoalkoxysilane (PTMS) condensation during the sol-gel process[219,220]. The phenylic group of PTMS has a higher steric hindrance, affecting the nucleation time (longer nucleation time) and the formation of a three-dimensional silica network. The chemical structure of TEOS exhibits four equivalent side chains and is, therefore, expected to induce more nucleation sites (corresponding to a shorter nucleation time) compared to the former one. PTMS can also act as a surfactant in this process due to its hydrophilic silanol headgroup and its permanently attached hydrophobic phenyl group, which may affect the particle size and its porosity.

Changing the ammonia concentration in the synthesis from $0.25 \, \mathrm{mol \, L^{-1}}$ up to $2.0 \, \mathrm{mol \, L^{-1}}$ at a constant PTMS and TEOS concentration (at $0.25 \, \mathrm{mol \, L^{-1}}$ and
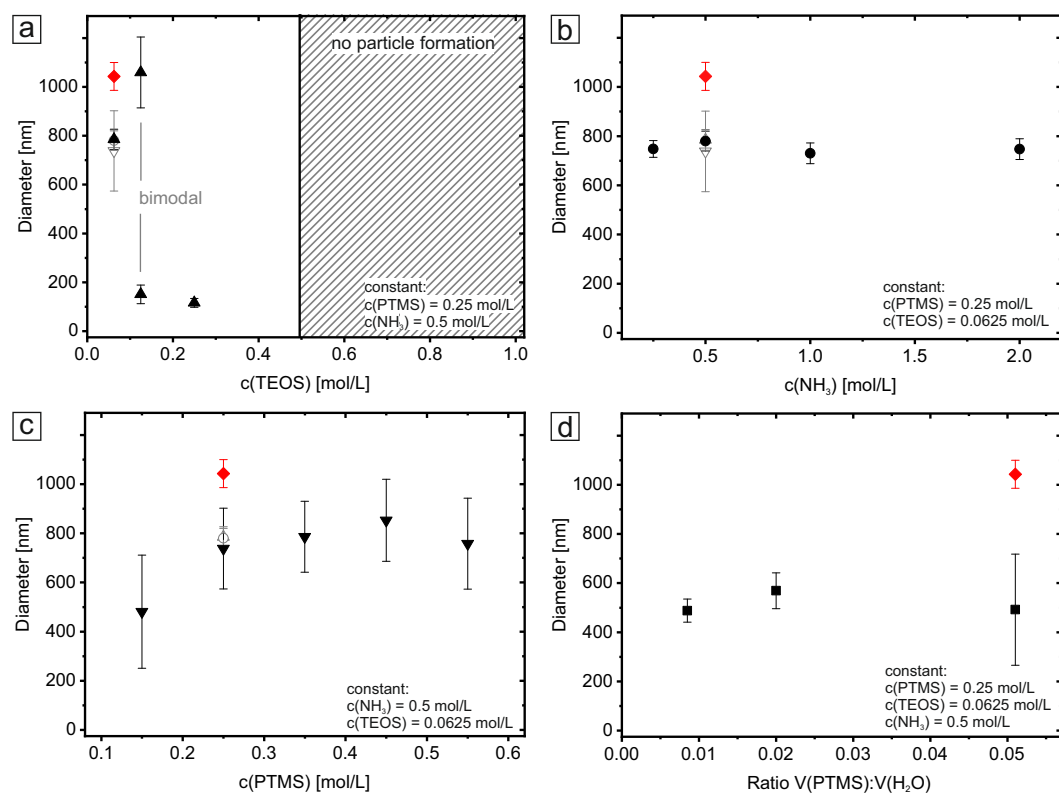
Figure 4.12.: Diameter variations of the particle dependent on the concentration of TEOS (a), ammonia (b), PTMS (c), and the volume ratio of PTMS and H_2O (d). The data points marked in red used a total volume of 150 mL; all other syntheses (black symbols) were conducted in small batches with mostly 15 mL. Error bars indicate the standard deviation of the particles. Reprinted with permission from „Carbothermal synthesis of micron-sized, uniform, spherical silicon carbide (SiC) particles", by Feller, T.; Rosenfeldt, S.; Retsch, M. *Journal of Inorganic and General Chemistry* **2021**, *647*, 22, 2172-2180.

$0.0625 \, \text{mol} \, \text{L}^{-1}$, respectively) did not influence the diameter of the particles. It resulted in diameters of about 750 nm for all particles. In literature opposing statements on the influence of ammonia can be found[114,115].

Also, the concentration of PTMS only marginally influences the resulting particle size. Beyond a concentration of $0.2 \, \text{mol} \, \text{L}^{-1}$, all samples range around 800 nm.

Changing the volume ratio of PTMS:H_2O as proposed by Segers et al.[221] to increase the particle diameter with a higher amount of water had no significant impact on the size but instead on the size distribution. The deviation of the particle diameter increased by around 35 % from low to high water content.

Hence, the optimum reactant concentrations from these screening reactions are c_{TEOS} = $0.0625 \, \text{mol} \, \text{L}^{-1}$, c_{PTMS} = $0.25 \, \text{mol} \, \text{L}^{-1}$ and c_{NH_3} = $0.5 \, \text{mol} \, \text{L}^{-1}$. In combination with a ten-fold upscaling of the reaction volume, the synthesized SiC-precursor particles had a size of 1043 ± 57 nm and narrow size distribution. The deviation from the small-batch screening syntheses is caused by subtle changes to the nucleation kinetics owing to the larger reaction vessel. The carbothermal reduction process and properties of these scaled-up precursor particles is outlined in the following paragraphs.

Carbothermal reduction to SiC

Then, the precursor particles were treated with a carbothermal heat process to obtain SiC particles. An excess of C relative to Si was introduced by the phenyl ring of PTMS. To convert the SiO_2 precursor into SiC, the powder samples were heated to $1500 \, °\text{C}$ (heating rate $20 \, \text{K} \, \text{min}^{-1}$) for 4 h in an Ar or N_2 atmosphere (flow rate $50 \, \text{mL} \, \text{min}^{-1}$, 1 bar). Subsequently, the SiC was purified from excess carbon species by post-thermal treatment (air, $800 \, °\text{C}$, 4 h) and characterized with SEM (see Figure 4.13).

The SiO_2-precursor ($SiO_2-\text{Ph}$) consists of spherical particles with smooth surface and a mean diameter of D = 1043 ± 57 nm, $\sigma = 5.4 \, \%$ (standard deviation of a Gaussian size distribution). The resulting particles in Ar and N_2 have a diameter of 710 ± 38 nm ($\sigma = 5.3 \, \%$) and 769 ± 41 nm ($\sigma = 5.3 \, \%$), respectively. After the carbothermal reduction, the spherical shape is well preserved. This contrasts with other studies[222], where it is pointed out that carbothermal reduction is a non-pseudomorphic transformation process. The particles showed a considerable shrinkage of about 30 % in size.

The shrinkage behavior of metal oxide precursors is already known; for example, Chen et al.[119] noticed shrinkage of 21 % after thermal conversion of C/SiO_2 to SiC aerogels, and Lechner et al.[223] determined a reduction of up to 18 % by calcination
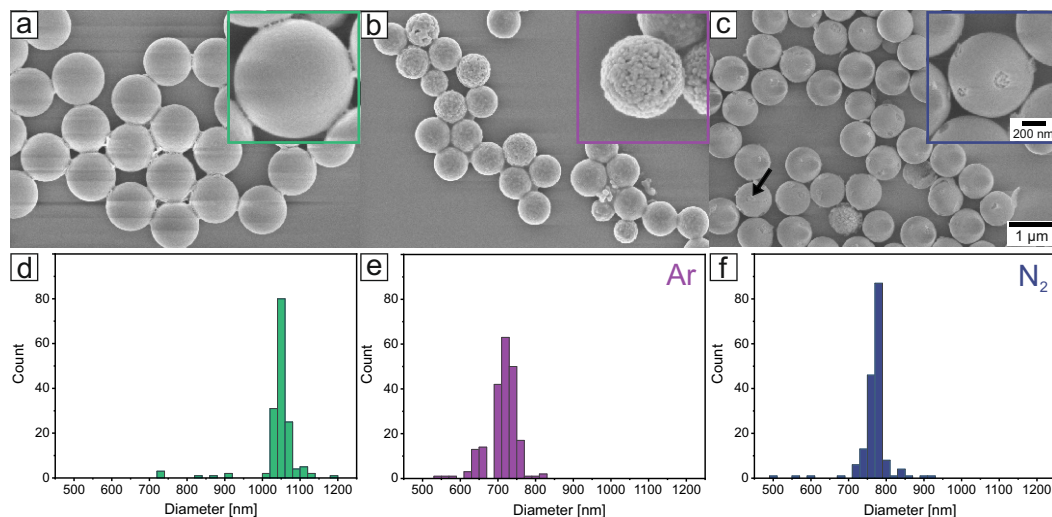
Figure 4.13.: SEM images of the precursor particles (a), the particles reacted in Ar (b), and N$_2$ (c) with a magnified image of one particle as inset. The corresponding size distributions (d-f) are below. Reprinted with permission from „Carbothermal synthesis of micron-sized, uniform, spherical silicon carbide (SiC) particles", by Feller, T.; Rosenfeldt, S.; Retsch, M. *Journal of Inorganic and General Chemistry* **2021**, *647*, 22, 2172-2180.

of TiO$_2$ to anatase. The size reduction is related to the release of gaseous species during the transformation process, particularly H$_2$O and CO, leading to a higher density and a considerable mass loss. Biernacki et al.[224] reported a two-step reaction pathway with gaseous CO(g) and SiO(g) as intermediates during the formation of SiC from SiO$_2$. For the possible intermediate Silicon (Si)[225], a shrinkage of the crystal lattice due to the formation of vacancies is known[226]. The variety of potential intermediates[227] also opens the possibility of side reactions and deviations from the targeted SiC composition. In this context, reactions with the atmosphere are possible; for example, at high temperatures from $1400 - 1450\,°C$, silicon dioxide can be converted to Si$_3$N$_4$ by a carbothermal reduction in N$_2$ atmosphere[228].

$$3\,SiO_2\,(s) + 6\,C + 2\,N_2 \rightarrow Si_3N_4\,(s) + 6\,CO\,(g) \tag{4.2}$$
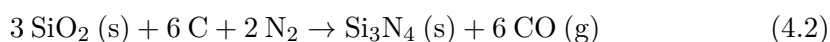
The particles exhibit different surface morphologies: rough (Figure 4.13.b, in Ar) and smooth (Figure 4.13.c, in N$_2$), demonstrating a significant influence of the atmosphere during the thermal treatment. Particles synthesized in an Ar environment seem to be coarsely grained, leading to a granular microstructure. The individual grains have approximately a size of 50 nm. These grains can be interpreted as crystallites of SiC. In contrast in nitrogen atmosphere, the surfaces of the particles are very smooth. No grain-like structures are detected due to the rather amorphous
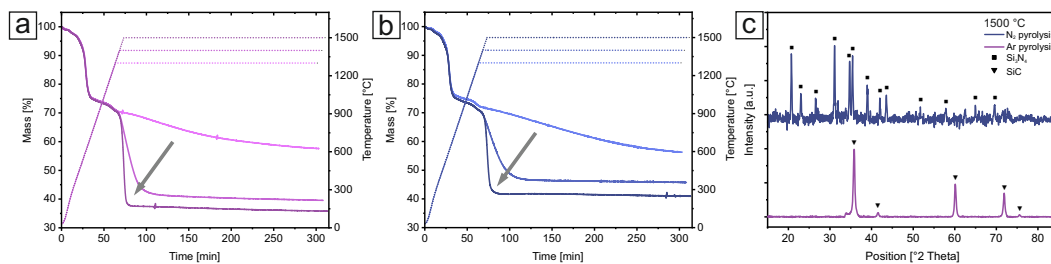
Figure 4.14.: STA measurements of the carbothermal reduction of SiO$_2$-PTMS precursor particles in Ar (a) and N$_2$ (b) atmosphere at three different temperatures (bright to dark). Results of XRD measurements (c) of the Ar and N$_2$ pyrolysis samples at 1500 °C. Reprinted with permission from „Carbothermal synthesis of micron-sized, uniform, spherical silicon carbide (SiC) particles", by Feller, T.; Rosenfeldt, S.; Retsch, M. *Journal of Inorganic and General Chemistry* **2021**, *647*, 22, 2172-2180.

microstructure even after pyrolysis. In rare cases, round areas or residuals from neighboring microparticles are visible. Such artifacts originate from the sinter processes among adjacent particles. N$_2$ adsorption isotherms (Figure A.1) of the precursor and pyrolyzed particles reveal strongly different BET surface areas and hystereses. Whereas the precursor, SiC commercial, and SiC Ar pyrolyzed can be regarded as non-porous materials, the pyrolysis under N$_2$ conditions results in an appreciable surface area of $\sim 270\,\mathrm{m^2\,g^{-1}}$. This large surface area is likely to be caused by the conical pores between clustered particles and by PTMS-templated pores in the mesoporous range.

To get a more profound insight into the atmospheric impact on the carbothermal process, STA measurements were performed in Ar and N$_2$ at 1300 °C, 1400 °C, and 1500 °C (see Figure 4.14). The general trend is similar in all samples: (a) The mass loss comprises two main steps. The first occurs right at the beginning of the heating ramp and reveals a mass loss of about 25 %. The second mass loss begins after 50 min at ca. 1000 °C. According to Seog et al.[115] the first step results from the loss of crystal water of SiO$_2$ and the second from the decomposition of the precursor phenyl groups. (b) It can be noticed that with increasing temperature, the second mass loss step is happening more abruptly. This second mass loss strongly depends on the pyrolysis temperature and requires > 1400 °C. The total mass loss depends on the atmosphere of the pyrolysis environment, with the Ar atmosphere leading to higher losses as compared to N$_2$. For 1500 °C, 1400 °C, and 1300 °C in Ar, the residual masses are 35.8 %, 39.6 %, and 57.6 %, respectively. In N$_2$, the residual masses are 40.9 %, 45.8 %, and 56.3 %, respectively.
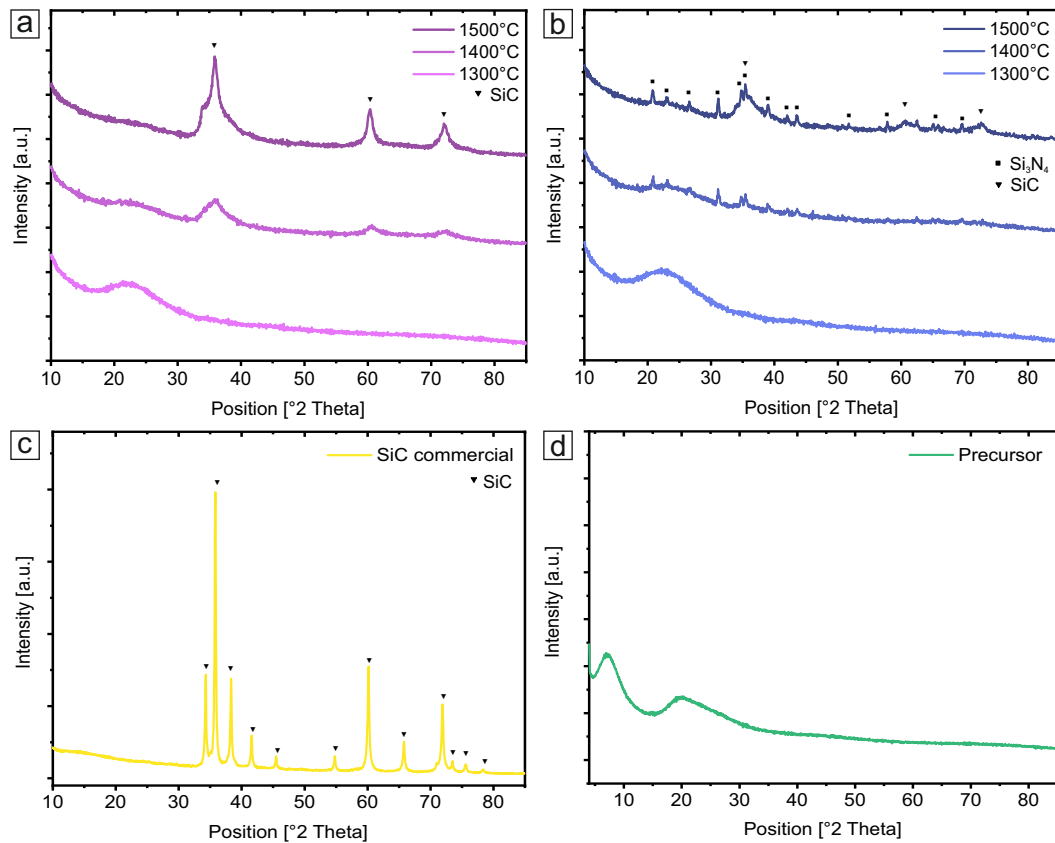
Figure 4.15.: XRD measurements without baseline correction of the carbothermal reductions in the STA at 1300 °C, 1400 °C, and 1500 °C from light to dark color in (a) an Ar atmosphere and (b) in a N_2 atmosphere. Reprinted with permission from „Carbothermal synthesis of micron-sized, uniform, spherical silicon carbide (SiC) particles", by Feller, T.; Rosenfeldt, S.; Retsch, M. *Journal of Inorganic and General Chemistry* **2021**, *647*, 22, 2172-2180.

The decrease in residual mass with increasing temperature suggests a more complete reaction at 1500 °C. A possible explanation for the lower values of the residual mass in the case of Ar atmosphere could be that (a) the conversion of SiO_2 to SiC in N_2 has a slower kinetic or (b) that a more complex reaction pathway inhibits the conversion in N_2 with the formation of side-products.

These assumptions were underlined by XRD data (see Figure 4.15). With increasing temperature, more and better-defined Bragg peaks are visible. Chu et al.[229] saw a similar influence on the reaction temperature. Compared to an industrial, non-spherical SiC powder, the crystallites are significantly smaller, which can be inferred by the broader peak width of the Bragg peaks. The XRD pattern of the industrially produced powder can be described by a mixture of hexagonal (71 %)[230] and cubic (29 %)[218] SiC.

The XRD data of samples prepared at 1300 °C shows no Bragg peaks, but a high monotonically increasing intensity for $2\theta > 10°$, and a broad shoulder at 2θ around 22°. The shoulder $\sim 22°$ is also present in the amorphous SiO_2-Ph precursor. Note that the peak seen in the pattern of SiO_2-Ph at $2\theta \approx 7°$ is missing, indicating the structural transformation of the precursor. This is in good accordance with the results of the STA, where the first mass loss occurred already around 570 °C. The peak positions of the sample prepared at 1500 °C in Ar are consistent with the expected positions of SiC[231], whereas the sample prepared at 1500 °C in N_2 hints at a mixture of SiC[232] and Si_3N_4[233]. The particles in Ar display five prominent peaks at $2\theta = 35.8°, 41.5°, 60.2°, 71.9°$, and $75.7°$, which can be identified as SiC. Stacking faults can explain the low-intensity peak at $2\theta = 33.2°$[234].

It is known that a huge number of SiC polymorphs exist and that during the transformation, intermediates of multiple different Si-species (SiC, SiO_2, SiO, Si) and side reactions can occur[227]. A precise assignment of the polytypes and their respective ratios in the obtained submicron-sized particles is impossible based on this XRD analysis. Nevertheless, the significant influence of the gaseous atmosphere on the structure of the particles is confirmed.
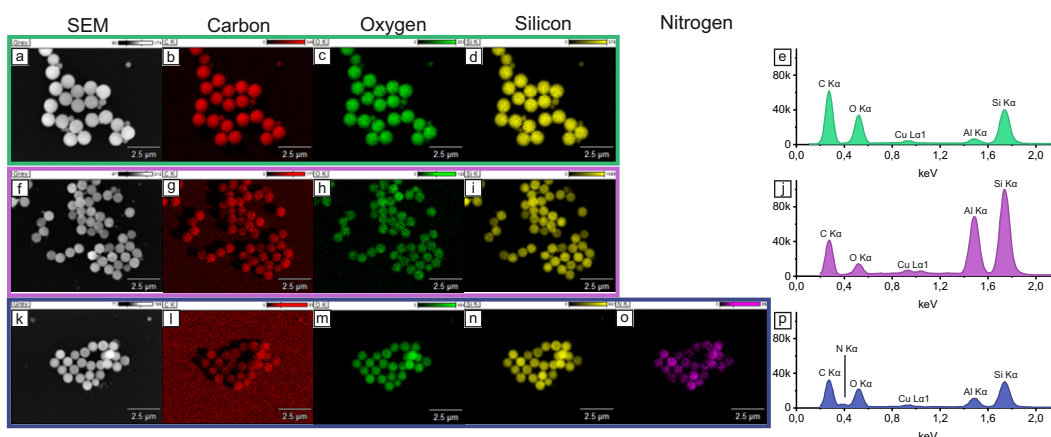
Figure 4.16.: EDS mapping images showing the precursor particles (a-d), the sample made in Ar (f-i), and the sample made in N_2 (k-o). Grey images showing SEM, red the carbon distribution, green the oxygen distribution, yellow the silicon distribution and pink the N_2 distribution on the particles. On the right side EDS spectra of the precursor particles (e), the sample produced in Ar (j), and the sample produced in N2 (p) are shown. In comparison to the other two samples, the N Kα line at around 0.4 keV is detected in (p). All spectra show Al Kα and Cu Lα1 lines because of the measurement setup with copper TEM grids and the STEM sample holder out of aluminium. Reprinted with permission from „Carbothermal synthesis of micron-sized, uniform, spherical silicon carbide (SiC) particles", by Feller, T.; Rosenfeldt, S.; Retsch, M. *Journal of Inorganic and General Chemistry* **2021**, *647*, 22, 2172-2180.

The formation of a sizeable amount of Si_3N_4 in the case of a carbothermal reaction in N_2 atmosphere is confirmed by SEM-EDS measurements (1500 °C, Ar or N_2, and precursor, Figure 4.16). Carbon, silicon, and oxygen species are the main compounds for the precursor and the samples transformed in Ar. Additionally, the sample converted in N_2 atmosphere, also shows a significant amount of nitrogen on the particle surface. In all cases, the elemental distribution is homogeneously spread across the particles, and no areas of distinct crystallites, enriched or depleted areas, can be discerned. A quantitative assessment of the elemental composition is hardly possible, particularly since a carbon-coated grid had to be used to immobilize the particles. However, in conclusion, under Ar atmosphere conditions, submicron-sized SiC particles of retained spherical shape could be accessed. In contrast, an N_2 atmosphere results in an incomplete transformation with a particular portion of Si_3N_4 as a side product. The successful conversion to SiC is additionally confirmed by the particle properties, which are outlined below.

The densities were investigated in a Helium pycnometer and are given in Table 4.1. In literature SiC has a density of about $\rho = 3.21\,\mathrm{g\,cm^{-3}}$.[235] Silicon nitride has a density of $3.17\,\mathrm{g\,cm^{-3}}$[236] and amorphous silica of $\rho = 2.12\,\mathrm{g\,cm^{-3}}$.[236]

Table 4.1.: Thermal properties and density of the particles.

	Effusivity	Thermal conductivity	Density
	$[\mathrm{W\,s^{1/2}\,m^{-2}\,K^{-1}}]$	$[\mathrm{W\,m^{-1}\,K^{-1}}]$	$[\mathrm{g\,cm^{-3}}]$
SiO_2-PTMS precursor	152.07	0.066	1.294 ± 0.003
SiC - Ar pyrolysis	136.56	0.063	2.894 ± 0.019
SiC - N_2 pyrolysis	102.62	0.055	2.258 ± 0.027
SiC - commercial	175.66	0.072	2.923 ± 0.013

The densities for the precursor (starting material), the samples in N_2 and Ar, and the industrial powder are $\rho = 1.3\,\mathrm{g\,cm^{-3}}, 2.3\,\mathrm{g\,cm^{-3}}, 2.9\,\mathrm{g\,cm^{-3}}$, and $2.9\,\mathrm{g\,cm^{-3}}$. Note that both pure SiC samples have comparable densities. The fact that the material obtained in N_2 has a lower density than pure SiC is consistent with the observation of a mixture of unreacted precursor, SiC, and Si_3N_4 (see results of XRD and STA). Next, the thermal properties of all samples were examined. The specific heat (c_p) (see Figure 4.17) is determined according to ASTM E 1269 and shows a continuous increase from around −30 °C to 250 °C. At ambient temperature, the synthesized SiC particles in Ar have $0.427\,\mathrm{J\,g^{-1}\,°C^{-1}}$, almost the same specific heat value as the

industry SiC powder ($c_p = 0.446 \, \text{J g}^{-1} \, {}^\circ\text{C}^{-1}$). In literature[235] for hexagonal SiC a value of $c_p = 0.69 \, \text{J g}^{-1} \, {}^\circ\text{C}^{-1}$ is reported. A possible reason for the discrepancy of these values could be the different SiC polymorphs in combination with different shapes and particle sizes. The silica precursor particles with phenyl groups have a distinctly higher heat capacity with $0.790 \, \text{J g}^{-1} \, {}^\circ\text{C}^{-1}$, comparable to silica literature values[237]. Furthermore, the sample synthesized in N_2 lies with $0.663 \, \text{J g}^{-1} \, {}^\circ\text{C}^{-1}$ in between and can be assigned to silicon nitride[238] or silicon[239].

The powders' effusivity and thermal conductivity were investigated with a modified transient plane source method (MTPS)[240] with a constant compressive force of 5 N. Here, the industry SiC powder has the highest value, followed by the precursor particles and the Ar sample, and finally, the N_2 sample with the lowest values (Table 4.1). The thermal conductivity at 300 K for bulk 3C-SiC in literature[235] is $k = 3.6 \, \text{W cm}^{-1} \, {}^\circ\text{C}^{-1}$, which is about a factor of 50 higher than the values obtained for this microstructured powder. In powders, such low values are often obtained and are a consequence of the constriction resistance at the interparticle contact area[241]. Considering the chemical variability of the samples, the obtained differences in effusivity and thermal conductivity for the industrial SiC, SiC in Ar, and for the precursor are negligible and in the same range. Differences among the samples have to be attributed to subtle differences in the interparticle contact area rather than the corresponding bulk material behavior.
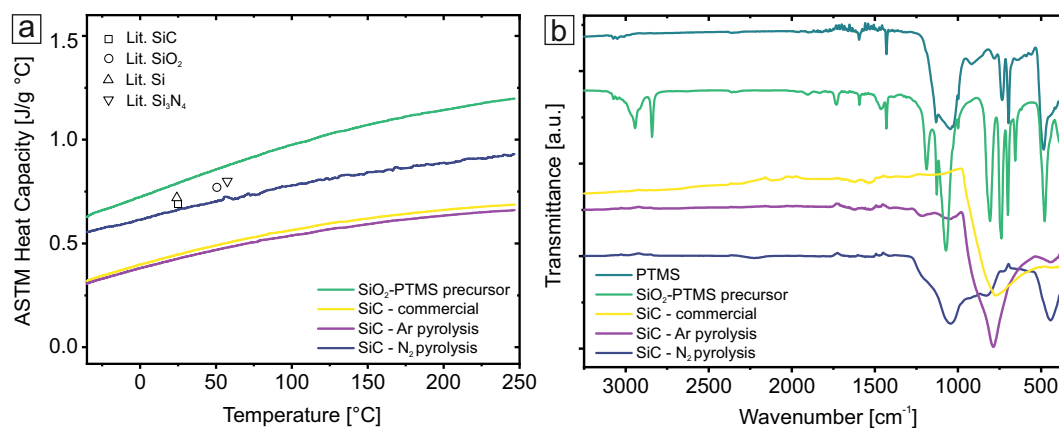
Figure 4.17.: Comparison of the specific heat data (a) and the transmission IR spectra plotted as offset (b) of the industry SiC powder, PTMS, precursor particles, particles fabricated in Ar, and in N_2. Reprinted with permission from „Carbothermal synthesis of micron-sized, uniform, spherical silicon carbide (SiC) particles", by Feller, T.; Rosenfeldt, S.; Retsch, M. *Journal of Inorganic and General Chemistry* **2021**, *647*, 22, 2172-2180.

The optical properties and, in particular, the suitability of these powders as efficient thermal emitters were investigated by Fourier transformation infra-red (FT-IR)

spectroscopy (Figure 4.17.b). The SiO_2–Ph precursor shows characteristic bands of both silica and pure PTMS. For example, the -C-O-H vibration at 1130 cm^{-1} and the phenyl ring deformation vibrations from 736 cm^{-1} to 698 cm^{-1} and 482 cm^{-1}[242]. In accordance with density, c_p, and XRD data, the precursor is confirmed as at least a mixture of the two constituents after their condensation reaction, TEOS and PTMS. The industrial SiC and SiC-rich samples (Ar, 1500 °C) exhibit a strong absorption band at $\nu = 785$ cm^{-1}, which is characteristic of the Si-C stretching mode[243]. The uniform spherical particles exhibit a more distinct peak at the Si-C stretching mode, which renders them particularly suitable for fabricating a selective emitter in this spectral range[8]. All other samples (N_2, precursor, and PTMS) show an absorption band at 1037 cm^{-1}, assigned to asymmetric Si-O vibration[244]. Additionally, the sample prepared in N_2 has small bands at $\nu = 831$ cm^{-1} and 441 cm^{-1}. According to literature[245], amorphous Si_3N_4 has a broad absorption band at around 840 cm^{-1}. The 441 cm^{-1} band can also be assigned to β-Si_3N_4[246]. These findings align with the previous measurements and corroborate that the sample prepared in N_2 is a mixture of the unreacted silica precursor and silicon nitride.

The complementary absorption properties of the Si_3N_4 compared to the SiC particles, may turn out to be particularly useful for passive cooling applications. As outlined above simple mixtures of these two particle powders would allow to design various emission properties in the sky window range and thereby access materials that can perform as selective or broadband emitting material.

Finally, the challenging task to produce SiC particles was successful with this method. The SiC production with the magnesiothermic reduction with a few variations was only successful with one particle batch with a diameter below 200 nm. Probably, the size of the silica particles is another crucial parameter and only small particle sizes can be converted with this technique. To produce submicron-sized SiC particles, the carbothermic route with evenly distributed carbon through the precursor particles, was the way to go.

4.2 Optical characterization of particle monolayers

Particles are often combined with polymer matrix materials for radiative cooling applications. Particle monolayers could be of particular interest because of the enhanced scattering properties in the UV/Vis region. Park et al.[153] presented a fast and easy method to produce particle monolayers. A particle powder is placed between two PDMS substrates and rubbed unidirectionally to form monolayers.

This was adapted with silica particles and the produced SiC and Si_3N_4 particles from the previous section. Additionally, PDMS is already an often used and well-characterized material for passive cooling, mostly combined with a back reflector.[27] Silica particle opals on PDMS were, for example, investigated as radiative coolers, combining colorization and thermal properties.[52] On the one side the thickness of the produced PDMS films was selected as thin as possible to see the influence of the particles within the sky window and not only characteristic bands of PDMS. On the other side, the film had to be thick enough to handle the freestanding films in the optical characterization. Hence, the films were spin-coated at 400 rpm onto a silicon wafer, the particles were put on top and rubbed for monolayer formation, and finally the PDMS film with the particles was removed. The samples were investigated with SEM, and representative pictures can be seen in Figure 4.18.
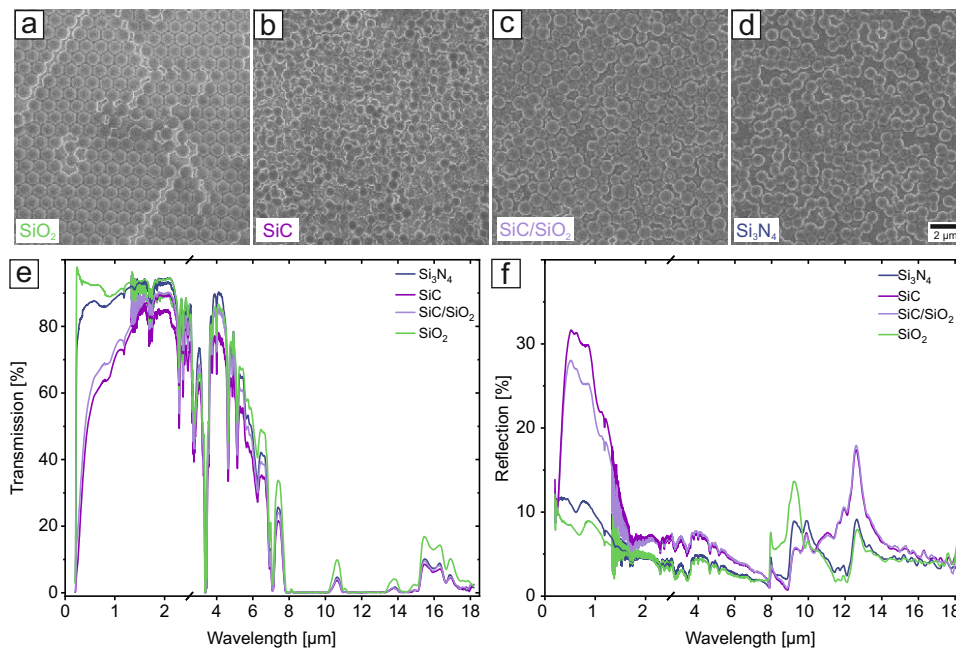
Figure 4.18.: Representative SEM images of the particle layers on a PDMS film with SiO_2 (a), SiC (b), a 50:50 mixture (wt.%) of SiO_2 and SiC (c) and Si_3N_4 (d). The transmission (e) and reflection (f) properties of the freestanding films were investigated in the UV/Vis and the IR region with an integrating sphere setup.

In all images, a slimy veil can be seen on the particles, due to the rubbing with the second PDMS substrate. The silica particles easily form a monolayer with medium-sized closed packed domaines. The other two particle samples and silica/SiC mixture form particle monolayers without particle clusters or stacked layers, but the particles are rather randomly distributed over the surface. The differences probably result from the different surface morphologies of the particles and thus different surface

adhesion energies to the substrate. Additional tests to improve the quality of the monolayer were carried out with different substrates, such as polyethylene- or polytetrafluoroethylene-foil. Furthermore, the rubbing conditions were altered, like the pressure or the rubbing direction. In any case no substantial improvement to the particle structures as shown in Figure 4.18.a-d have been observed. However, it was decided that the monolayers were sufficient for a first proof-of-concept.

The optical properties were measured for the UV/Vis and the IR region in transmission and reflection geometry with an integrating sphere setup. The resulting combined graphs are displayed in Figure 4.18.e and f. The transmission curve shows almost no transmission over the whole IR region. This can be attributed to the PDMS film, which superimposes any other material properties. For shorter wavelengths in the UV/Vis region, the high transmission is gradually decreasing at around 1.5 μm for the SiC and the mixed SiO_2/SiC sample. The other two samples show a transmission between 80 % and 96 % until ∼400 nm a rather sharp cutoff can be observed. The reflection values are, in general, comparably low. Nonetheless, the SiC and the mixed sample reach up to 30 % reflection in the UV/Vis region. In the sky window, bands originating from (back)scattering of the materials can be seen, for example, from the silica particles (Si-O-Si band) at 9.3 μm[244] or from the SiC particles (Si-C band) at 12.5 μm.[243] As already mentioned in the previous section, the Si_3N_4 sample shows bands from silica, silicon carbide, and silicon nitride[247] at 9.2 μm, 12.6 μm and 9.9 μm, respectively. Interestingly, the curve of the mixed SiC/SiO_2 sample resembles the curve of the SiC sample. This can be caused by an inhomogeneous distribution of both particle materials on the PDMS surface during the monolayer formation via rubbing.

Overall, the reflection in the UV/Vis range could be enhanced with SiC containing monolayers of the particle materials without an additional back reflector. In conclusion the application of a monolayer of colloidal particles to a support substrate represents a viable and interesting route to optimize a materials optical properties for passive cooling applications. In particular the diffuse reflectance introduced by the SiC particles is interesting to reduce the heat load caused by solar radiance. Clearly, further improvements needs to be conducted, for example with respect to the particle mixture and the monolayer application. Further steps to transform this material platform to actual passive cooling devices is their assessment of the cooling performance in field test and the evaluation and optimization of such granular coatings with respect to abrasion and mechanical impact. The optical characterization demonstrated here is encouraging to follow this material concept in future studies.

3D Structured Materials

<div style="text-align: right; font-size: large;">5</div>

Going beyond individual colloidal particles as outlined in the previous two chapters, I also investigated pathways to SiC materials with a three-dimensional structure. The 3D structured materials under consideration in my thesis can be grouped in two categories. First, 3D structures with a periodic mesostructure giving rise to a photonic stop-band. This have been investigated via inverse opal structures. Second, 3D structures without long-range order giving rise to scattering. These have been briefly outlined in approaches towards fiber-based ceramics.

Uniformely sized polymer particles can be assembled into closed packed colloidal crystals. These 3D structures were further processed as a hard template for inverse opals. The space in between the spheres were filled with metal-oxide and silicon carbide precursors. As in Chapter 4 the sections will be grouped according to the respective fabrication process. A magnesiothermic reduction was conducted with a polymer precursor and TEOS to produce SiC inverse opals. Second, an industrial silicon carbide matrix precursor comprising polycarbosilane was analyzed. And finally, carbothermic reactions were carried out with different metal-oxide precursors to compare inverse opals out of silica, titania, and SiC.
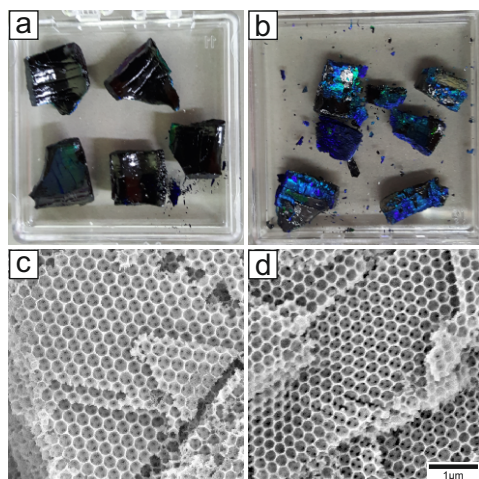
5.1 Inverse opal structures

The colloidal crystals used in this chapter were fabricated via centrifugation and evaporation-induced self-assembly of positively charged PS particles with diameter sizes between 144 nm and 712 nm. The latter is an easy and well-known assemble technique of particles in dispersion. After several days of drying, the colloidal crystals were usually cracked into small pieces of around or less than one square centimeter. The main disadvantages are the long fabrication time and the formation of cracks in the micro range due to internal stresses in the drying process. A centrifugation method was used to form many, highly ordered colloidal crystals in a shorter time frame. Here, the particles were assembled over night. The supernatant was then either removed by suction, and the colloidal crystal was dried for further use, or replaced with a ceramic precursor in multiple cycles. A photograph and a SEM image of the particle assembly *via* centrifugation is depicted in Figure 5.1.
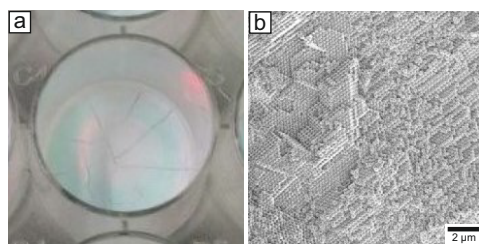
Figure 5.1.: a. Photograph of the shimmering colloidal crystal of the sample with 363 nm sized particles in a spot plate after centrifugation. b. Representative SEM image of the assembled particles.
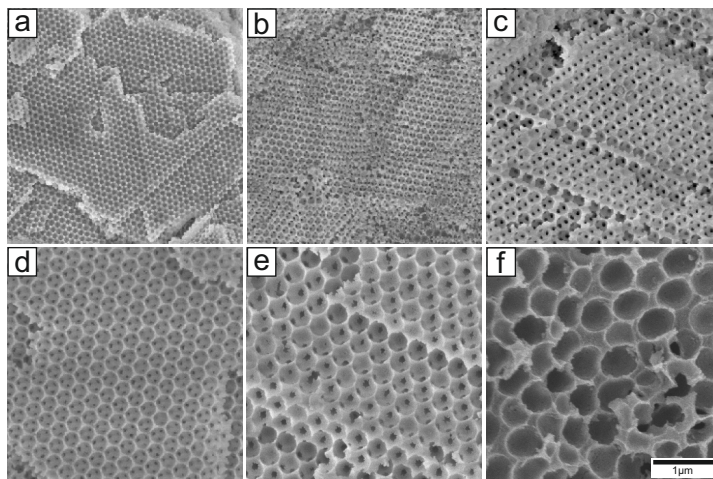
5.1.1 Magnesiothermic reduction

The magnesiothermic approach was carried out based on the work of Shi et al.[121] and Wang and Stein.[248] A mixture of the block copolymer Pluronic F-127 as a surfactant, a phenol-formaldehyde resin as the carbon source, and TEOS as a silicon source was used to infiltrate the colloidal crystals. The particle diameters of the PS sphere building blocks were 144 nm, 163 nm, 347 nm, 363 nm, 473 nm, and 712 nm (PS01-06). All samples in this section were produced with the evaporation-induced particle assembly strategy. After the infiltration process *via* capillary forces, a first heating step in argon atmosphere was conducted to pyrolyze the PF resin to carbon. Also, the polymer particles were burned away to form the inverse structure (see Figure 5.2).

Figure 5.2.: Photographs and the representative SEM images of the pyrolyzed inverse opal structure (a and c) and the resulting and cleaned SiO_2/SiC material after the magnesiothermic reduction (b and d) of a sample with 363 nm sized particles.

The composites were then mixed with magnesium chips, converted at $800\,°C$, and the MgO residues were cleaned with hydrochloric acid. The samples did maintain

their structure and also offer an iridescent color as a result of optical diffractions from the crystal lattice planes, which can be seen in Figure 5.2.b. All samples were analyzed with SEM to confirm the retaining of the inverse opal structure. Representative pictures can be seen in Figure 5.3.

Figure 5.3.: Representative SEM images after the magnesiothermic reduction of the inverse opals produced with different sized polymer particles as building blocks for the colloidal crystals: a) 144 nm, b) 163 nm, c) 347 nm, d) 363 nm, e) 473 nm and f) 712 nm.

All samples are arranged in a regular closed packed form, except the sample with the biggest particle diameter (712 nm), which has a more amorphous looking structure. Errors in the assembly process, due to the size of the particles or the surface charges, could be an explanation for this. Therefore, this sample was not further investigated and excluded for the following optical analysis. Furthermore, it can be noted that the highly ordered domains are increasing with increasing particle size. The arrangement of the colloidal crystal template, and thus their pores in the inorganic reverse replica, is mainly regarded as face-centered cubic (fcc).[249] This was suggested on the basis that the fcc arrangement of spherical particles is entropically more favored than the hexagonal closed packed (hcp) assembly.[250] However, most colloidal crystals comprise a mixture of fcc and hcp structures, which cannot be distinguished by the SEM analysis shown here. To gain more knowledge about the chemical composition, XRD measurements were performed (see Figure 5.4). Here, only for two samples (144 nm and 363 nm) small peaks at $2\theta = 35.8°, 60.1°$ and $72.0°$ are visible, which can be assigned to silicon carbide. In all other samples, no crystalline phases are detected (see Figure 5.4). This leads to the assumption that the conversion process was at least sometimes successful. The samples also could consist of a mixture of small crystalline domains and amorphous silicon carbide.
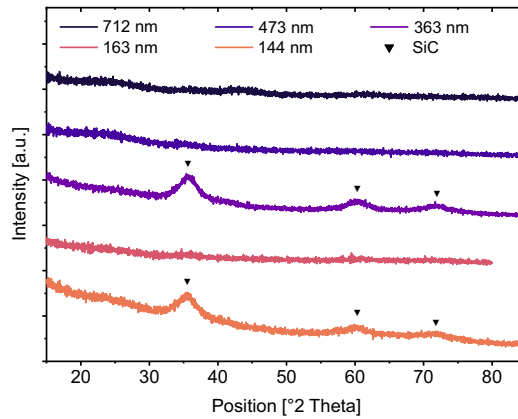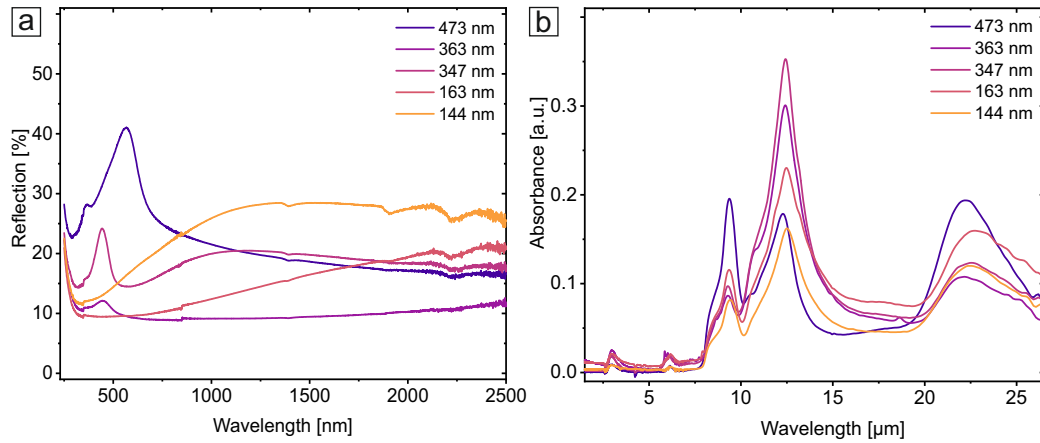
Figure 5.4.: XRD measurements of the inverse opals fabricated with different starting particles. Only two samples (144 nm and 363 nm) show very small peaks, which can be assigned to silicon carbide. For the other samples no crystalline phases are detected.

The optical properties of the inverse opal samples were analyzed with UV/Vis and IR measurements. The UV/Vis reflectance measurements were conducted with bulk samples and thus randomly oriented powders between two quartz glass slides. The powders were carefully grained beforehand to homogenize the samples. For specular reflection measurements it can be assumed that only Bragg peak positions from the 1st order from the 111 plane are visible, as merely the flakes with a proper orientation will be detected.

The analysis showed bands at 444 nm for the 163 nm sample, 448 nm for the 363 nm sample, and 566 nm for the 473 nm sample. The small dip at 360 nm is related to the change of the light source in the measurement. The 144 nm sample has no visible Bragg bands, but the reflection increases between 500 nm and 1000 nm and reaches a constant maximum of around 28 %. The 347 nm sample shows a similar behavior, but the increase in reflection takes place over a broader wavelength range. The most intense bands arise from first order Bragg diffraction from (111) planes of the fcc colloidal crystal lattice.[251] Additionally, a red shift of the band positions can be observed, which can be related to the increase in the average center-to-center distance between the pores on the (111) planes. A more profound analysis is not meaningful with this data.

Samples for the ATR-IR analysis were also carefully grained before the measurement to enhance the contact area between the powder and the ATR crystal. This was easy to achieve, as these samples are relatively brittle and form homogeneous powders. Three main absorption bands can be seen in the ATR-IR spectra for all samples. The peak at 9.4 μm with a small shoulder at 8.5 μm can be assigned to the transverse-optical (TO$_3$) mode from Si-O-Si and the antisymmetric stretching LO$_3$, which are

Figure 5.5.: a. UV/Vis measurements of the inverse opal samples. The material was placed between two quartz glass slides and analyzed in reflection mode. b. ATR-IR spectra of the same five inverse structure samples.

typical for silica sol-gel materials.[244] A silicon carbide peak at 12.5 μm, which represents the transverse optical phonon, with a shoulder at around 10.8 μm, is visible for all samples. The shoulder can either be explained by the longitudinal optical phonon[252] or an underlying Si-CH$_2$ wagging mode.[243] In general, the ATR-IR analysis confirmed that silicon carbide had been formed for all samples.

The broad peak between 20 μm and 25 μm can be assigned to the LO$_1$ rocking mode of silica glass. The small absorption band at around 3 μm results from stretching modes from hydroxyl groups at the silica surface. The samples consequently consist of a mixture of SiO$_2$ and SiC. This is also in good accordance with the XRD analysis and explains the amorphous properties. The ratio of the maximum intensities of the silica and the silicon carbide band is comparable for the samples with small hole sizes (144 nm and 163 nm) and the two middle ones (347 nm and 363 nm) with I$_{max}$(SiO$_2$)/I$_{max}$(SiC) around 0.5 and 0.29, respectively. Only for the 473 nm sample this ratio is reversed with a value of 1.11. Sadly, this ratio does not quite match up with the existence of crystalline SiC domains in the 144 nm and the 363 nm sample from the XRD measurements.

In summary, the production of SiO$_2$/SiC inverse opal composites with the magnesiothermic reduction was successful. The IR bands offer a combination of these two materials and cover the sky window range between 8 - 13 μm. However, a quantification of the reflected, transmitted, or diffused radiation was not achieved. The optical analysis confirmed the preservation of the photonic mesostructure for three specimen. An increased reflectivity in the visible range confirmed the concept to utilize structural colors to mitigate the impact of solar radiance, even with SiC containing materials. The IR absorption properties are also highly attractive

for potential passive cooling applications, since a highly selective absorption and emission profile could be realized by such mixed SiO_2/SiC inverse opals. What is missing is a full analysis of the absorption properties in the solar range, which is very likely to require further improvement to keep the thermal influx to a minimum. Further improvements to the synthesis procedure are also required to yield photonic powders of inverse opals with a better control on the SiC phase.

5.1.2 Polycarbosilane precursor

SMP-10 is a commercially available one-component liquid polycarbosilane precursor to silicon carbide ceramics. The chemical structure is depicted in Figure 5.6. Amorphous (glassy) SiC can be formed between $850 - 1200\,°C$ with a 72 - 78 % ceramic yield. In a subsequent heating step to $1250 - 1700\,°C$ nanocrystalline β-SiC can be formed with this material. This preceramic polymer was made for applications in a macroscopic size scale, like a large area repair kit for space shuttles.[253] However, research groups already used it, for example, to produce porous films for membrane applications[254] or for 3D printing of SiC/carbon fiber nanocomposites.[255]
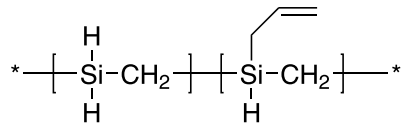
Figure 5.6.: Chemical structure of the silicon carbide matrix precursor SMP-10 from Starfire Systems.

Colloidal crystals out of particles with diameter sizes of 144 nm, 163 nm, 347 nm, and 473 nm were deposited into this viscous polymer fluid for several days while the air cavities were infiltrated by using capillary forces. The samples appear shimmering black after the one-step pyrolysis temperature profile to glassy SiC. In contrast, after the second heating step forming crystalline SiC, the fragments changed the color to silver metallic and are very hard. The latter hints at the successful forming of silicon carbide. The structure was again analyzed with SEM, and representative images of the 363 nm sample before and after the transformation can be seen in Figure 5.7.a and b.

After the first temperature step to amorphous SiC, the inverse opal structure remains intact. However, the conversion to polycrystalline SiC did destroy the structure completely. The material is sintered together, and only smooth material fragments are visible. This can be explained by the following: the manufacturer advises
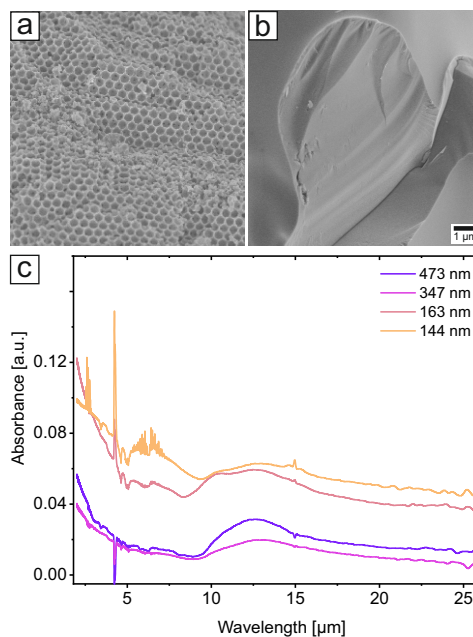
Figure 5.7.: Representative SEM images of the inverse opal sample with the particles PS03 produced with SMP-10 after the conversion to amorphous SiC (a) and after the subsequent heating step to polycrystalline SiC (b). ATR-IR spectra of the amorphous inverse opal samples.

infiltrating the polymer and doing the pyrolysis step multiple times to minimize the porosity and to form a dense composite. However, the colloidal crystal system makes this impossible because the polymer particle scaffold is burned away after the first cycle. Thus, the porosity of the material is too high, which results in fast escaping of gases generated during the process and crack formation. The ATR-IR spectra of all four samples after the first pyrolysis step (see Figure 5.7.c) do show a broad peak between 10 μm and 15 μm. This can be induced by the underlying Si-C vibration at around 12.7 μm.[243] The broadening of the peak can be caused by insufficient contact between the samples and the ATR crystal. Here, the samples could not be easily grained in a mortar into homogeneous powders, as in the previous section about the magnesiothermic reduction. The material was very stiff and only larger pieces of the material were placed onto the crystal. Hence the contact between the sample and the crystal was not good, and errors in reflection can occur. This is probably also the reason for the noise and the sharp peaks in the spectra. Towards smaller wavelengths, an increase in absorbance is noticeable.

In conclusion, the fabrication of amorphous SiC inverse opals was successful with the polycarbosilane polymer precursor. However, the conversion to the crystalline state included a simultaneous loss of structure. Future tests could contain colloidal crystals out of silica spheres to realize more infiltration steps as they withstand

higher processing temperatures, or to adjust the thermal treatment step to find milder conditions for the system.

5.1.3 Carbothermic reaction

The carbothermic approach was conducted with the same SiC precursor, which was already used in Chapter 4 and also extended to form inverse structures out of other metal oxide materials. In particular, TEOS was used to produce SiO_2 and $Ti(OBu)_4$ as a precursor for TiO_2.

The fabrication of silica inverse opals is a well-known process.[256] However, the widely used liquid-phase infiltration with additional suction through the colloidal crystals or the application of vacuum comes with some difficulties: unwanted nonporous overlayers can be formed, or the viscosity of the precursor solution has to be carefully adjusted. High viscosity solutions lead to an incomplete filling of the template. In contrast, in diluted precursors, the void space is not entirely filled, after the evaporation of the solvent.[86] Hence a new diffusion driven process was established here for silica inverse opal production. Here, the particles were centrifuged in spot plates, the supernatant was removed, and new solution with an increasing amount of TEOS was added over a few cycles. The colloidal assembly stayed in the wet state during the complete process. Resulting samples were analyzed with SEM (see Figure 5.8.a-d).

Overall, this method did lead to the inverse opal structure after the calcination in the tube furnace under Ar atmosphere. A few problems occurred in changing the liquid above the colloidal assembly after centrifugation. The removal of the supernatant was carried out with a vacuum aspiration system or small glass pipettes. The top particles layers were always either carried away or at least swirled around, leading to a loss in the colloidal crystal order. Additionally, the addition of new precursor liquid thereafter enhanced this phenomenon. This also can be verified with the SEM images. With increasing particle diameter, the inverse structure gets more amorphous (see Figure 5.8a-d). The attractive and repulsive forces, which affect the colloidal assembly, change with higher particle diameters. Thus, centrifugation parameters, like the centrifugal force or the temperature, need to be optimized for better results. This technique to infiltrate the colloidal structures with a diffusion process was also tested for PTMS and $Ti(OBu)_4$ precursor solutions for SiC and TiO_2, respectively. However, this approach was discarded after a few tests with concentration and solvent variations. These precursors have, for example, faster sol-gel reaction times, or an enhanced possibility of reaction with moist air, which
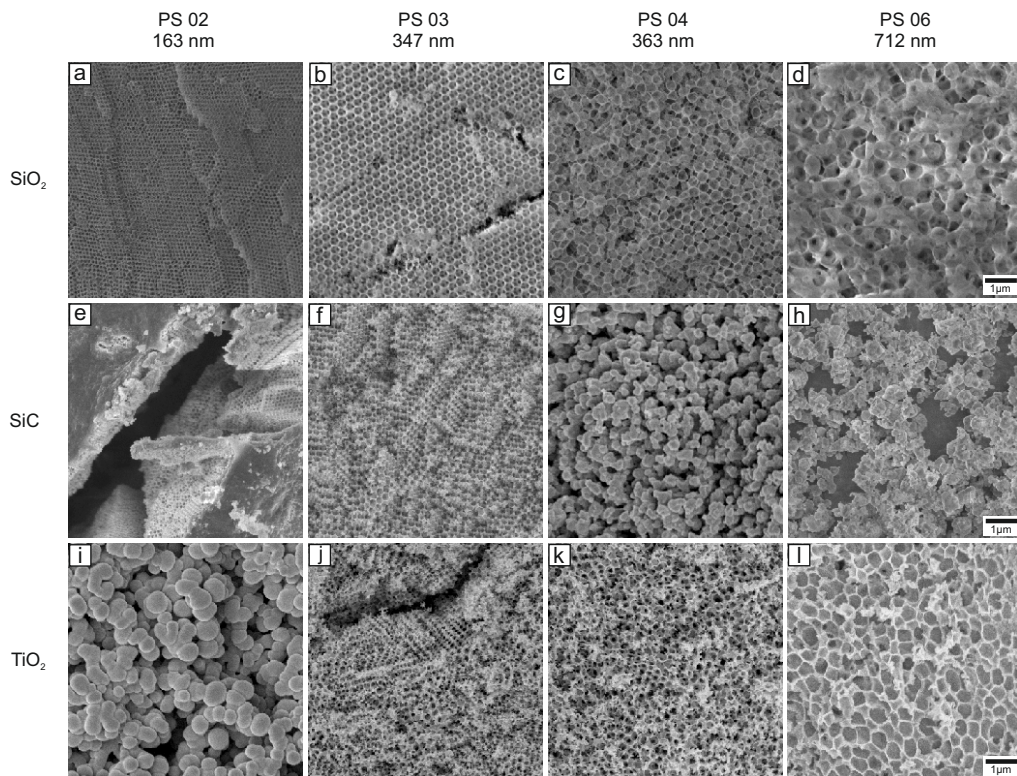
Figure 5.8.: Representative SEM images of SiO$_2$ (a, b, c, d), SiC (e, f, g, h) and TiO$_2$ (i, j, k, l) inverse opal samples fabricated out of colloidal crystals with particle sizes of 163 nm, 347 nm, 363 nm, and 712 nm in the respective rows and columns. The silica precursor was infiltrated with a stepwise diffusion process. The precursor solution for SiC and titania was infiltrated via vacuum suction. The scale bar for all images is equal to 1 μm.

led to gelling, particle formation in the precursor solution, or the loss of the colloidal crystal structure (see Figure 5.9).

Figure 5.9.: Agglomeration of the titania precursor solution with the assembled PS particles in spot plates after centrifugation.

A „classical" attempt to infiltrate these precursors with vacuum suction was carried out, to prevent the above mentioned problems. The colloidal crystals were still fabricated by centrifugation, dried, and broken into small pieces. Additionally, a more stable precursor solution with a 50:50 mixture of PTMS and TEOS was used for the production of SiC. The resulting structures after the pyrolysis method (Ar atmosphere, 1500 °C, 20 °C min^{-1}, 4 h isothermal holding) can be seen in Figure 5.8.e-h. Unfortunately, the structure could not be preserved for most SiC samples. Overlayers were formed (Figure 5.8.e), or the samples transform into powder like structures, due to the formation of SiC crystals (Figure 5.8.g/h). In the case of titania (see Figure 5.8.i-l), a different calcination method in air atmosphere was used: from ambient temperature to 300 °C with a heating rate of 2 °C min^{-1}, followed by an isothermal step for 2 h, a second heating step to 400 °C, again an isothermal step for 2 h before cooling down. The sample with the smallest particle template (163 nm, Figure 5.8.i) lead to particle formation, whereas the mesoscopic structure was retained for the other template particles. Next, ATR-IR analysis was conducted with all samples, and the spectra can be seen in Figure 5.10.
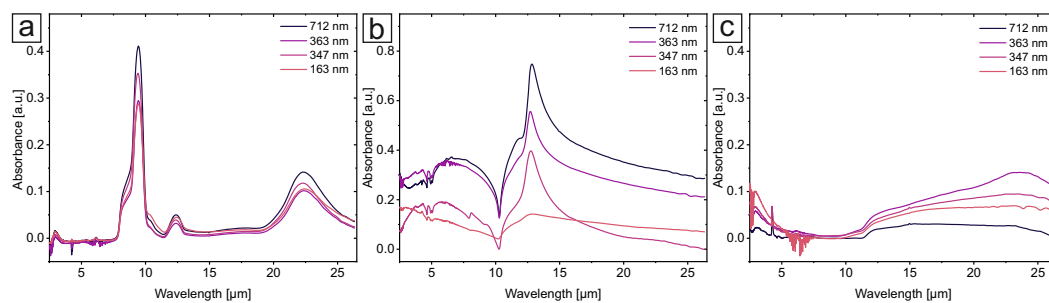

Figure 5.10.: ATR-IR spectra of all samples made out of silica (a), silicon carbide (b) and titania (c) regardless of the successful fabrication of the inverse opal structure.

The spectra of the silica samples showed the typical silica prominent peaks at 9.5 μm with a small shoulder at 8.4 μm. Absorption bands at 2.9 μm, 12.4 μm, and a broad peak between 20 μm and 25 μm can be assigned to the O-H stretching mode, symmetric stretching of LO_2-TO_2 and the LO_1 rocking mode of silica, respectively.[244] A silicon carbide peak at 12.8 μm can be found for all samples. However, the band is rather unpronounced for the 163 nm sample. Additionally, a reversed dip at 10.3 μm is visible. This can be attributed to a reflection of the SiC material. Unfortunately, the increase in the absorption band cannot directly be connected to the increasing size of macropores in the inverse opal structure (see SEM analysis), due to possible intensity changes of the peaks with varying surface contact between the sample and the ATR crystal. Titania samples show small absorbances at 3.0 μm, which can be attributed again to the O-H stretching mode. An increased absorbance over the whole range from 11.5 μm to 25 μm can be associated with the characteristic vibrational modes of Ti-O and Ti-O-Ti bonds.[257,258]

As seen above, a significant loss of structure was noticeable in the conversion process to SiC. One last attempt to enhance the stability of the colloidal assembly was realized by using PS@SiO$_2$ core-shell particles (PS04, 363 nm + 20 nm silica shell), instead of polystyrene particles. The SiO$_2$ shell should function as a mechanical reinforcement of the colloidal crystal during pyrolysis. The colloidal assemblies were infiltrated with both, a PTMS precursor and a PTMS/TEOS precursor mixture, via a vacuum suction technique. In addition to that, the one-step heating method to 1500 °C was separated into a pre-pyrolysis step at 550 °C and subsequent carbothermic conversions with different heating rates (10 K min^{-1}, 20 K min^{-1}, and 50 K min^{-1}). These pyrolysis steps were carried out with the STA in argon atmosphere with small sample amounts. The resulting structures were analyzed with SEM, and the images can be seen in Figure 5.11

After the first pyrolysis step in argon atmosphere, the PS core of the particles is carbonized. Now, the samples consist of a 3D assembly of silica hollow spheres, infiltrated with a precalcined SiO$_2$/SiC precursor, and the carbon residues from the polystyrene core. The samples in this state can be seen in Figure 5.11.a and e. After the second heating with different heating rates, the pieces were again analyzed with SEM. With increasing heating rate, the particle assembly structure gets more and more lost. In the samples infiltrated with the PTMS precursor and heated with 10 K min^{-1} and 20 K min^{-1} small areas with hollow spheres can still be seen, whereas the material got dense with even higher heating rates. This is in analogy to the synthesis of SiC particles in the literature. The formation of crystalline SiC is favored with high heating rates but normally accompanied with the loss of the
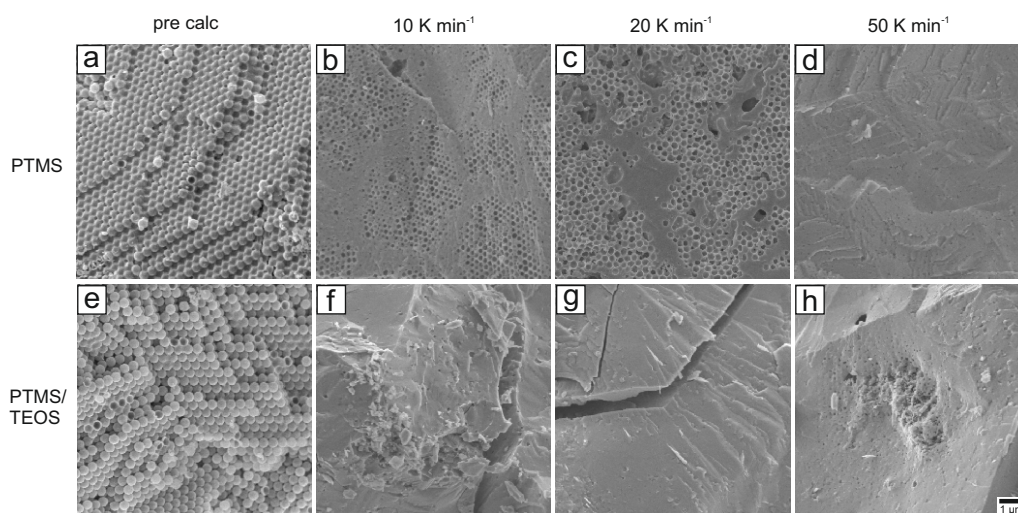
Figure 5.11.: Representative SEM images of inverse structures with PS@SiO$_2$ particles as templates infiltrated with a PTMS precursor solution (a-d) and a PTMS/-TEOS precursor mixture (e-h) after the pre pyrolysis step at 550 °C (a, e), and after the carbothermic reaction with a heating rate of 10 K min^{-1} (b, f), 20 K min^{-1} (c, g), and 50 K min^{-1} (d, h).

template structure. An ATR-IR measurement confirmed the conversion from SiO$_2$ to SiC (see Figure 5.12).

However, the samples infiltrated with a mixture of PTMS/TEOS lost their structure at all testet heating rates. One possible explanation is, that the infiltration of the colloidal crystal was not sufficient. The voids between the particles appear to be not filled in the SEM image after the first pre calcination step (Figure 5.11.e). Hence, the silica hollow spheres probably just melted at 1500 °C. Further IR analysis of these samples was not implemented, as the SEM analysis already showed the complete loss of inverse structure.

The TGA analysis of these samples of the second heating step does not show a trend (see Figure 5.13). In general, the curves all resemble the same shape. The samples infiltrated with the PTMS precursor have various residual masses: 65 %, 60 %, and 71 % with a heating rate of 10 K min^{-1}, 20 K min^{-1}, and 50 K min^{-1}, respectively (5.13.a). The other batch infiltrated with the a PTMS/TEOS precursor mixture, posses a residual mass at around 70 % with the two slower heating rates. Note, that the measurement conducted with 50 K min^{-1} was aborted before the isothermal step.

The last experiments showed, that it was not possible to fabricate SiC inverse opals with the carbothermic reaction in a reproducable way. It was not possible to find
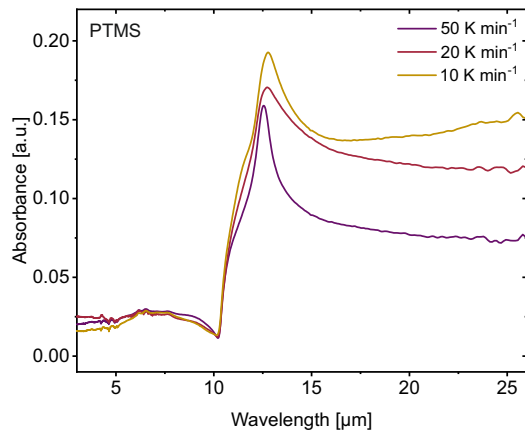
Figure 5.12.: ATR-IR spectrum of the structures after the carbothermic reaction with three different heating rates, which were fabricated with assembled silica CS particles infiltrated with PTMS precursor.
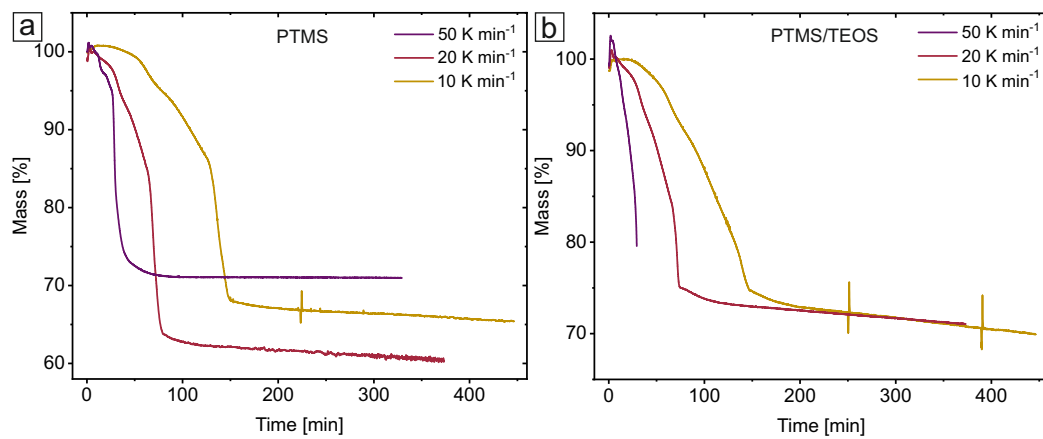
Figure 5.13.: TGA data of the carbothermic reaction to 1500 °C of the infiltrated samples with PTMS (a) and PTMS/TEOS (b) precursor solution with different heating rates.

a stable PTMS precursor solution, that did not gel, formed particles, or was too diluted. This lead to problems with the infiltration of the particle template so that it was not sufficient in all cases. However, the general formation of SiC was achieved, but mainly in combination with the loss of the specific structure. Enhancing the stability of the template by using PS@SiO_2 core-shell particles did not yield better results. The attempt to use two seperate pyrolysis steps probably lead to a lack of carbon in the system. Hence, the ratio of silicon to carbon atoms was not correct for the transition to SiC. Maybe this could be overcome in future experiments by adding additional carbon to the system, or by repeating the infiltration step several times.

An adaption of the system to TiO_2 was possible with some samples but titania precursors have much higher sol gel reaction kinetics than their silica counterpart, which lead to gelling, or even solidification prior to the calcination step. That should be addressed in upcoming work in a comprehensive way for better results.

The infiltration of particle templates *via* a diffusion process with a SiO_2 precursor solution worked out very well. This method could be used for large-scale (centimeter range) productions of inverse opals.

In conclusion, the formation of SiC inverse opals *via* magnesiothermic reduction lead to higher yields, than *via* carbothermic reaction. This is the opposite finding compared to the submicron-sized particle structures in chapter 4. Apparently the inverse opal skeleton is less resilient to the transition from amorphous to crystalline SiC. The carbothermal reduction, therefore, induces a higher mechanical stress and ultimately failure to the inverse opal skeleton compared to the magnesiothermic route.

5.2 Fibers

Fibers are an interesting 3D structure, which is not only used in biomedical engineering[259] or electronics[260] but have also enhanced scattering properties for passive cooling applications.[261] Polymer fibers have the advantage over photonic metamaterials that they can be easily fabricated over large scales. This also leads to research efforts to transfer the passive cooling theory to smart fabrics and personal thermal management.[41] Among other techniques, like the well-known electrospinning[262], the solution blow spinning (SBS) process recently gained more attention. The polymer jet is stabilized only by a high-pressure air flow that flows around the polymer solution. The resulting fibers are deposited in the direction of the gas flow.[263] Therefore, this method can be implemented and adjusted using inexpensive, transportable, and hand-held equipment, like commercially available airbrushes.[264] Therefore, I tried to transfer the knowledge gained from the previous chapters to get access to ceramic nanofibers with potentially suitable optical properties for passive cooling applications. Scattering properties of existing objects could be enhanced. For example, blinds of buildings could be spray-coated with a polymer or ceramic material to easily optimize the thermal properties in hindsight.

First tests were conducted to produce fibers with an airbrush using water-soluble PVA and PVP solutions. Based on literature,[265,266] the concentrations of the polymer solutions, the molecular weight, or the pressure were adjusted to find a reasonable optimum of parameters. The distance between the airbrush nozzle and the glass slide, which was used to collect the resulting fibers, was fixed to 20 cm for all conducted experiments. Microscopic images of fabricated PVP fibers ($\sim 1,300,000\,\mathrm{g\,mol^{-1}}$, 7 wt.% in EtOH) with variated pressure are depicted in Figure 5.14.
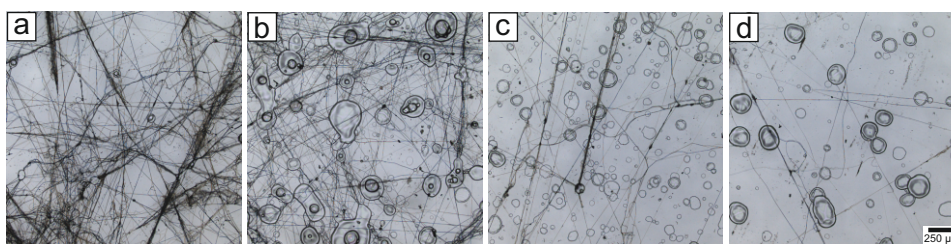
Figure 5.14.: Microscopic images of PVP fibers ($\sim 1,300,000\,\mathrm{g\,mol^{-1}}$, 7 wt.% in EtOH) fabricated with an airbrush with (a) 1.8 bar, (b) 1.4 bar, (c) 1.0 bar, and (d) 0.7 bar.

It can be seen that an increased amount of fibers are visible with increasing pressure. However, multiple drops of the polymer solution were sprayed onto the glass slides,

indicating a non-stable fiber stream from the nozzle. This also seems to decrease with higher pressure. A further increase of the polymer solution concentration only showed similar results with a pressure of 1.4 bar (see Figure 5.15). No fiber fabrication was possible with these samples and higher pressures. The polymer solution clogged the outlet of the airbrush.
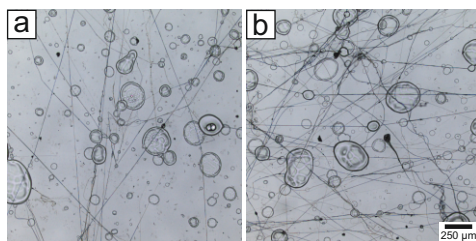
Figure 5.15.: Microscopic images of PVP fibers ($\sim 1,300,000\,\mathrm{g\,mol^{-1}}$) fabricated with an airbrush with 1.4 bar and (a) 10 wt.% or (b) 14 wt.% in EtOH.

Similar tests were conducted with PVA in water. For example, a variation of the concentration of the polymer solution can be seen in Figure 5.16. Here, overall fewer fibers are visible compared to the PVP experiments. Several solution drops occurred with the higher concentrated sample (see Figure 5.16.b). Solution blow spinning with water as the solvent is a bit more challenging than with ethanol. The evaporation rate of water is low and thus heat is applied at the SBS tip in comparable experiments in literature to get micro- and nanofibers.[265]
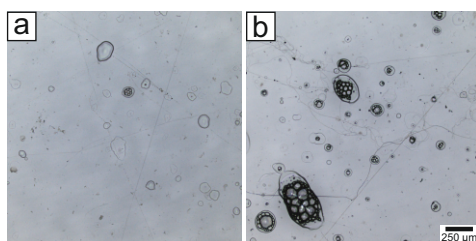
Figure 5.16.: Microscopic images of PVA fibers ($\sim 67,000\,\mathrm{g\,mol^{-1}}$) fabricated with an airbrush with 1.4 bar and (a) 14 wt.% and (b) 18 wt.% in H_2O.

The most reasonable parameters for the fiber formation out of PVP and PVA solutions are listed in Table 5.1.

Furthermore, a PVP solution with additional PS particles (202 nm in diameter), and a PVP/TEOS precursor solution were tested. The latter was calcined afterwards to form SiO_2 fibers towards high scattering materials for passive cooling applications. These fiber structures were additionally analyzed with SEM, and the images are depicted in Figure 5.17. Here, a few of the PS particles which are incorporated in the fibers can be seen (see Figure 5.17.c). Also silica fibers were successfully produced.

Table 5.1.: Successful parameters for fiber fabrication with the airbrush.

Polymer	M_w $g\,mol^{-1}$	Concentration $wt.\%$	Solvent	Pressure
PVP	1,300,000	7	EtOH	1.4
PVA	67,000	14	H_2O	1.4

However, beads in the fiber structure are visible, which can be caused by altering the polymer solution parameters due to the addition of the silica precursor.
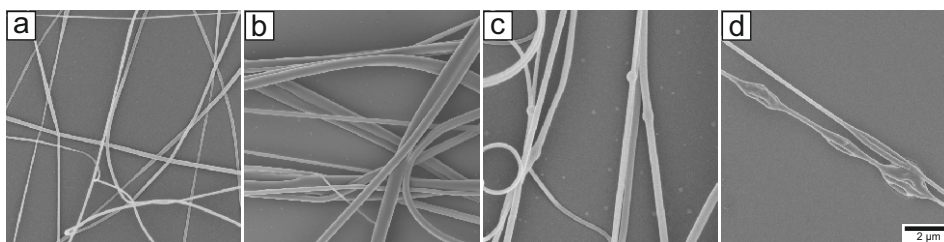
Figure 5.17.: SEM images of the fabricated fibers out of (a) PVA, (b) PVP, (c) PVP with 200 nm sized PS particles and (d) SiO_2 (after calcination) with a solution blow spinning process conducted with an airbrush.

It was possible to fabricate fibers with all polymer solutions. It can be seen that the diameter of the fibers is not highly uniform. Branching and bead formation can also occur. Using an airbrush makes the fiber fabrication easily accessible but otherwise lacks parameter control. A considerable drawback was the clogging of the airbrush nozzle, especially with the silica precursor mixture. This can be attributed to various known problems, like fast evaporation of the solvent, the missing of a constant polymer solution flow, or the nozzle design.

A 3D printed setup was fabricated to gain more parameter control. The fabrication of customized nozzles can be challenging. One possibility to form SBS setups is to utilize well-established soft lithographic techniques used in the fabrication of microfluidic devices.[267] With the latest innovations in 3D printing technology to fabricate structures to the submicrometer scale, it could be used as an alternative to lithographic methods.[268] The design setup was adjusted from the work of Hofmann et al.[269] Especially, the air channel was improved with a conical design reducing to the outlet nozzle. The CAD image and the resulting setup in the lab are depicted in Figure 5.18.

In theory, the solution channel had a diameter of 0.2 mm and was coaxially surrounded by the air channels with a targeted diameter of 0.3 mm. Microscopy analysis
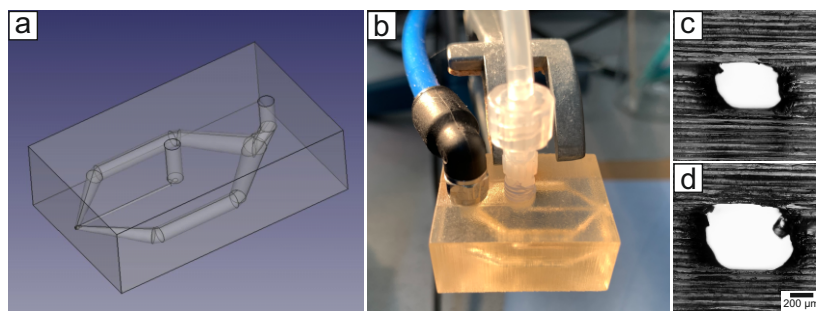
Figure 5.18.: CAD image of the block geometry with channels for the polymer solution and the air flow (a) and a photograph of the resulting 3D printed setup. Microscopy images of 3D printed channels with a theoretical diameter of 0.2 mm (c) and 0.3 mm (d).

showed, however, that the diameter is larger and appears not perfectly round in the experimental setup. The thin channel is rather around 420 μm in height and 700 μm in width, and the thick channel has dimensions of $\sim$570 μm height and 870 μm width. The polymer channel was connected to a syringe pump to adjust the solution flow rate. Tests with pure PVP solution according to the parameters in Table 5.1 and a flow rate of 2 mL h^{-1} were successful, leading to a first proof-of-concept design. PVP fiber accumulations which were fabricated with the airbrush system and the 3D printed setup after around 3 min spraying time are shown in Figure 5.19.
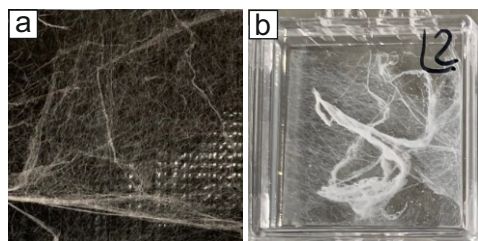
Figure 5.19.: PVP fiber accumulations fabricated with the airbrush (a) and the 3D printed setup (b).

This technique can be transferred and applied to multiple materials and composites to form random structured fibers. Organic polymer fibers, as well as ceramic fibers, could be produced and analyzed for passive cooling applications. Recently, researchers already showed the possibility to fabricate SiO$_2$,[270] TiO$_2$,[271] or Al$_2$O$_3$-stabilized ZrO$_2$[272] fibers. With a sol-gel precursor like PTMS or a suitable polycarbosilane, silicon carbide fibers could be produced. Adding extra particles opens up a variety of material combinations leading to enhanced scattering and material properties, which could be used in the future.

Conclusion and Outlook 6

In this thesis, polymer and ceramic particles and particle-based structures were prepared and analyzed for radiative cooling applications. The following key results were achieved:

1. Particle size distribution, clustering and zeta-potential analysis of multiple particle systems with field flow fractionation.

2. Synthesis of submicron-sized spherical silicon carbide particles with a carbothermic approach.

3. Fabrication of silica/silicon carbide inverse opals in different size ranges with magnesiothermic reduction.

4. Revealing the differences in the manufacturing techniques of the carbothermic reaction and the magnesiothermic reduction and offering new knowledge in the conversion process from silica to silicon carbide.

Field flow fractionation was used to study different particle systems to show this method's versatility and mainly analyze particle size distributions with MALS. The elution diagrams of batches of poly(methyl methacrylate)/n-butyl acrylate particles, which were synthesized with a special emulsifier-free emulsion polymerization, showed the gradient character of the particles. The different sizes in diameter could, however, still be distinguished. Ellipsoidal PS particles with three different aspect ratios (2:1, 3:1, and 4:1) were analyzed. The broadening of the elution peak could directly be related to the increasing aspect ratio of the particles. Additionally, the elugrams revealed cluster formation, and hence the fabrication and cleaning procedure of the ellipsoids could be optimized. Finally, polystyrene@silica core-shell particles and their resulting hollow spheres were tested. It was shown that the zeta potential measurement of the CS particles was comparable to a standard method. Silica hollow spheres with different shell thicknesses were redispersed in water *via* ultrasonication. The analysis showed a shift in elution time and changes in the autocorrelation function, which could be linked to the destructive ultrasonication power of newly formed particle clusters. Additional SEM evaluation gave an insight into the stability of these hollow spheres.

Spherical submicron-sized silicon carbide particles from 700 nm to 1 μm were successfully produced from silica precursor spheres in a carbothermal process. The key component was the usage of phenyltrimethoxysilicate in the sol-gel synthesis. Thereby, phenyl groups were covalently bonded to the silica network, which later acts as the carbon source during the conversion. An expanded parameter investigation of the sol-gel reaction with PTMS has to be conducted to cover a wider size range. The carbothermal reduction proceeds in an isomorphic manner and results in uniformly shrunk ($\sim$30%) microparticles. Argon as the inert atmosphere is paramount to drive the SiC conversion to completion. A nitrogen environment during carbothermal reduction, in contrast, inhibits the silicon carbide formation and leads to a mixture of silica and silicon nitride as side reactions. The established protocol for well-defined silicon carbide beads is of high relevance to building nanophotonic structures with controllable properties in the mid-infrared range. The monolayer assembly of these particles onto a PDMS film showed its potential as a radiative cooling material. Future work should highlight the quantitative analysis of scattering and absorption fractions for the particles in the UV/Vis and IR range by specialized powder measurements.

Amorphous SiO_2/SiC inverse opals with various pore sizes were fabricated with a magnesiothermic reduction. Hexagonally close-packed polystyrene colloidal crystals were infiltrated with a mixture of phenol-formaldehyde resin and silica sol-gel precursor solution. The magnesiothermic conversion led to iridescent powders, which showed enhanced reflection and Bragg reflexes in the UV/Vis range and absorption peaks in the sky window range. The precursor system based on PTMS, which was already used for the particles, was applied in a carbothermic approach to fabricate inverse opals. However, problems in terms of the precursor stability and the preservation of the mesostructure occurred and could not be overcome by adjustments in the calcination step or by using PS@SiO_2 core-shell template particles. Furthermore, a diffusion-based infiltration method *via* centrifugation was demonstrated for silica inverse opals. The advantage over classical methods is the combination of colloidal assembly and precursor infiltration to form large-scale sample pieces in a shorter time frame. The fabrication of SiC inverse opals should be focused on the magnesiothermic approach in the future. The cycled infiltration technique *via* diffusion in the centrifuge could be applied to this system to produce large sample sizes. With this, the optical properties and the photonic band gaps can be investigated in more detail to understand the fundamental physical processes for further optimizations.

It was shown that for producing different SiC structures from silica precursors, distinct conversion techniques are favored. Particles were synthesized with the

carbothermic reaction, whereas the magnesiothermic approach is preferable for inverse opals. Hence, the macroporous or bulk character of the samples results in different reaction outputs. In addition, it can be concluded that not only the stoichiometry of this reaction is crucial but also the sample weight, and the interface between silicon and carbon atoms. Especially the nitrogen inert gas atmosphere, lead to silicon and magnesium oxide instead of silicon carbide in the magnesiothermic transition. A mass increase of the resulting material was visible in the STA measurements, indicating a reaction between the gas and the sample to magnesium nitride. This contributes to understanding these reactions, which are still discussed in the research community.

Most importantly, the radiative cooling properties of the particles and powders should be tested in in- or outdoor measurement setups. Additionally, further processing into composite films is required. Moreover, polymer or ceramic fibers by a spray-on method are especially interesting as an easily accessible material class to improve the cooling properties of already existing buildings or objects.

The presented results contain a good foundation for the fabrication of silicon carbide particle structures. The idea to use these materials for radiative cooling applications, can still be improved, for example, by further size variations and the following implementation in composite materials. Also, a number of challenges for future work have to be solved, like the proper optical evaluation of powders in the UV/Vis and IR range. Nevertheless, this work extended the possibilites to produce ceramic colloidal structures and also highlighted important reaction parameters, like the inert gas atmosphere, for the successful conversion of silica to silicon carbide materials.

Experimental section

7.1 Materials

The following reagents and solvents were used as received:

2-Azobis(isobutyramidine)hydrochloride (AIBA, SigmaAldrich GmbH, 97 %),

2-Methacryloxyethyltrimethylammoniumchloride (MTC, Polyscience, 70 % solution in water),

3-Styrenesulfonic acid sodium salt hydrate (NaSS, Sigma-Aldrich GmbH, >99 %),

Acrylic acid (AA, SigmaAldrich GmbH, 99 %),

Ammonia (NH_4OH, Sigma-Aldrich GmbH, 25 % solution in water),

Ammonia (NH_4OH, Honeywell Chemicals, 30 - 33 % solution in water),

Carbon powder (Sigma-Aldrich GmbH),

Ethanol (SigmaAldrich GmbH, 99.8 %),

Formaldehyde (Sigma-Aldrich GmbH, 37 wt.% solution in water, 10 - 15 % methanol as stabilizer),

Hydrochloric acid (HCl, 2 N, Merck KGaA),

Isopropanol (Sigma-Aldrich GmbH, 99.7 %),

Magnesium (Sigma-Aldrich GmbH, turnings, for Grignard reactions, >99.5 %),

Pluronic® F-127 (Sigma-Aldrich GmbH, powder),

Poly(vinyl alcohol) (PVA, SigmaAldrich GmbH, Mowiol® 8-88, $\sim 67,000 \text{ g mol}^{-1}$),

Polyvinylpyrrolidone K30 (PVP, Alfa Aesar, $50,000 \text{ g mol}^{-1}$),

Polyvinylpyrrolidone (PVP, SigmaAldrich GmbH, $40,000 \text{ g mol}^{-1}$, $360,000 \text{ g mol}^{-1}$ and $1,300,000 \text{ g mol}^{-1}$),

Potassium persulfate (KPS, 99 %),

Silicon carbide powder (ESK-SIC GmbH),

StarPCS™SMP-10 (Starfire Systems)

Styrene (SigmaAldrich GmbH, >99 %),

Tetraethyl orthosilicate (TEOS, Sigma-Aldrich GmbH, for synthesis),

Titanium butoxide ($Ti(OBu)_4$, Sigma-Aldrich GmbH, 97 %),

Trimethoxyphenylsilane (PTMS, Sigma-Aldrich GmbH, 97 %).

Millipore water was taken from a Millipore Direct Q3UV unit (Merck Millipore) for synthesis and purification.

2,2-Azobis(isobutyronitril) (AIBN, SigmaAldrich GmbH) was recrystallized before use. 80 g of AIBN was dissolved in 600 mL of pure methanol at 45 °C. The solution is slowly cooled to room temperature and the resulting crystals were filtrated through a Büchner funnel and washed with methanol. Finally, it was dried under vacuum at room temperature.

Methyl methacrylate (MMA, SigmaAldrich GmbH, 99 %), and *n*-butyl acrylate (nBA, SigmaAldrich GmbH, 99 %) were purified by filtration over an alumina column (activated, basic, Brockmann I).

7.2 Synthesis

7.2.1 Synthesis of polymer materials

Positively charged PS particles in the size range up to 500 nm diameter. The general synthesis was performed according to Ruckdeschel et al.[130] First, a 500 mL three-neck flask was equipped with a gas inlet and a reflux condenser. 1.8 g PVP ($55,000 \, \mathrm{g \, mol^{-1}}$) was dissolved in 10 mL water and added to the flask. 225 mL water, 26 mL styrene and 50 μL MTC was mixed and also added. After that, the mixture was heated to 70 °C under a slight argon flow with a stirring speed of 850 rpm. 0.6 g AIBA was dissolved in 5 mL water and was added to initiate the polymerization after 60 min. The stirring speed was reduced to 450 rpm, when the particle precipitation starts and the color of the mixture turns to white, and the reaction was allowed to continue over night. By exposing the dispersion to ambient air the polymerization was stopped. The PS particles were filtrated with a 125 μm nylon sieve to remove particle clusters. The size of the particles can be adjusted by changing the amount of MTC.

Positively charged PS particles in the size range above 600 nm diameter. The original method of this dispersion polymerization was published by Cheng et al.[273] and further advanced for different particle sizes by Lechner et al.[223]. Initially, 3 g PVP ($40,000 \, \mathrm{g \, mol^{-1}}$) was dissolved in 10 mL ethanol via ultrasonication. After adding the PVP solution, 46 mL EtOH, 10 mL MilliQ water, 11 mL styrene and 300 mg AIBN into a 250 mL three-necked flask equipped with a reflux condenser and a gas inlet, the solution was degassed while stirring with 150 rpm. After 30 min the reaction temperature was set to 70 °C. Meanwhile, 56 mL EtOH, 11 mL

styrene and 300 μL MTC were mixed in an Erlenmeyer flask and then added after 90 min to the reaction. Under a slight argon flow the reaction was carried out over night. The polymerization was stopped by exposing the dispersion to ambient air and filtered with a 125 μm nylon sieve. By decreasing the amount of styrene, the particle size can also be decreased.

Negatively charged PMMA particles. Monodisperse PMMA particles were synthesized with an emulsion polymerization. The size of the seed particles was then later gradually increased during a semibatch process. The special setup for this synthesis has to be prepared beforehand. A 100 mL three-necked flask with an oval stir bar is equipped with a reflux condenser, a septum and a second septum with a 3 mm hole. In the latter, a 20 mL syringe is attached to 2 m of silicone tubing (2 mm inner diameter). Both are washed and subsequently filled to the 5 mL mark with MilliQ water. A long cannula is inserted through the septum and bent in an U-shape at the end. Initially, 48 mL MilliQ water is loaded to the flask and heated to 80 °C with a stirring speed of 650 rpm and the nitrogen flow is turned on. At the same time, MMA was degassed seperately with nitrogen at room temperature. Both systems were equilibrated for around 75 min. Then, 2 mg of NaSS dissolved in 1 mL water was added quickly to the flask. A 5 mL syringe with the perfusor tube is equipped with 5.5 mL of MMA. After 5 min 1.7 mL MMA was added with a syringe pump at 290 mL h^{-1}. Again after 5 min, 40 mg KPS dissolved in 1 mL water was added. The reaction of the seed particles is complete after 30 min. The size of the particles can now be increased as initiator is still present in the system and the reaction is not quenched yet. More monomer is added gradually, while the fractions are simultaneously extracted and stored in the tube. The syringe pumps have the following parameters:

- Extraction: 5.0 mL with 5.0 mL h^{-1} (syringe diameter: 20 mm)

- Air fractions: 0.016 mL with 31 mL h^{-1} (syringe diameter: 12.5 mm), 30 s pause

- Monomer feed: 2.9 mL with 2.9 mL h^{-1} (syringe diameter: 12.5 mm)

The reactions proceeds over one hour and the extracted batches form gradient PMMA particles.

Ellipsoidal PS particles. Negatively charged monodisperse PS particles with an average diameter of 326 nm (SEM image evaluation, dispersity < 5 %) were synthesized by an emulsifier-free emulsion polymerisation with AA as co-monomer according to Goodwin et al.[129] After extensive washing with water, the spherical particles were dispersed in a poly(vinyl alcohol) solution via a SpeedMixer (Hauschild

DAC 400.2 VAC-P)(20 % w/w PVA and up to 4 % w/w PS of the final dispersion; up to 24 % w/w solid content in dispersion). A gas-free suspension was obtained by application of vacuum ($\sim$ 50 mbar) during speed-mixing at 2500 rpm for 10 min. The resulting dispersion was doctor bladed into films of up to 20 x 37 cm on a glass plate (wet film height 1 mm; blading speed 8 mm/s; Film applicator Zehntner ZAA 2300). After drying for 2 days at room temperature, foil pieces of up to 9 x 4 cm were mounted onto a self-built uniaxial stretching device, heated in a convection oven to 150 °C for 30 min and then stretched to the desired aspect ratio in multiple steps, depending on the targeted aspect ratio. The homogeneous middle pieces of the stretched foils were cut out and dissolved in an isopropanol:water mixture (3:7 v/v) at 60 °C (hot wash). Centrifugation and redispersion in hot isopropanol:water was repeated two times, followed by three times of centrifugation and redispersion in ultrapure water.

Phenol formaldehyde resin. The synthesis was conducted according to Meng and coworkers.[274] 15.267 g phenol and 3.25 g NaOH solution (20 wt.%) were added to a 100 mL three-necked flask equipped with a reflux condenser and dissolved at 42 °C with a stirring speed of 500 rpm. After ca. 10 min 26.25 g formalin was added, the reaction mixture was heated to 75 °C and stirred for 1 h. After 30 min the color changes to rose. When the solution is cooled down to room temperature, the pH value was adjusted to $\sim$ 7 with 1 M HCl. The resulting NaCl was removed by filtration and the water was removed in a rotary evaporator under reduced pressure. Finally, the resin was redissolved in ethanol and a final concentration of 35.8 wt.% is achieved.

7.2.2 Synthesis of inorganic materials

Silica particles. A Stöber process[72] was used for the synthesis of silica particles. In a typical reaction, ethanol, water ($c_{H_2O} = 7.4\,\mathrm{mol\,L^{-1}}$) and ammonia ($c_{NH_4OH} = 0.51\,\mathrm{mol\,L^{-1}}$) were initially mixed in a 50 mL round-bottom flask and equilibrated for 2 h with 550 rpm. Then, $0.5\,\mathrm{mol\,L^{-1}}$ TEOS was added. The total volume of the synthesis was 30.3 mL. The reaction was stirred over night at room temperature. Finally, the particles were cleaned one time with ethanol and three times with water and freeze dried for two days.

SiO$_2$@C core-shell particles. Small silica particles with a resorcinol formaldehyde shell were synthesized in a one-pot synthesis according to Fuertes et al.[210] Here, 32 mL ethanol, 8 mL H$_2$O and 1.25 mL ammonia was mixed in a 100 mL three-neck flask equipped with a reflux condenser and stirred with 300 rpm at 30 °C. After

Table 7.1.: Synthesized SiO$_2$@C core-shell particles with the according diameters.

Sample	Diameter core [nm]	Diameter shell [nm]
SiO$_2$@C **A**	198 ± 22	30
SiO$_2$@C **B**	370 ± 17	40

30 min, 1.28 mL TEOS was added. 10 minutes later, 203.4 mg resorcinol and another 10 min later 0.28 mL formalin was added. Then, the mixture was stirred for 24 h at 30 °C and finally heated to 100 °C and reacted for another 24 h. Another synthesis route was conducted according to Guan et al.[211] 10 mL of a silica particle dispersion (8 wt.%, D = 370 ± 17 nm, $\sigma = 4.37\,\%$) was mixed with 324.25 mg CTAB, 47.11 mg resorcinol, 4.05 mL EtOH, 14.2 μL ammonia in a 25 mL round-bottom flask and stirred with 300 rpm at 35 °C. After 30 min, 71 μL formalin was added and stirred for another 6 h. Finally, the reaction was cooled down to room temperature and was allowed to react over night without stirring. For both routes, the resulting particles were washed one time with ethanol and three times with water. Afterwards, they were freeze dried for two days. The resorcinol-formaldehyde shell of the particles was then calcinated in a muffle furnace at 550 °C for 5 h to get silica carbon core-shell particles.

Silica hollow spheres. PS particles with a diameter of 264 ± 10 nm ($\sigma = 3.66\,\%$) were synthesized via emulsifier free emulsion polymerization as described above. These particles were coated with silica with a modified Stöber process to get PS@SiO$_2$ core-shell particles. For the synthesis, 40 mL PS dispersion was diluted in 280 mL EtOH and 1/10 of the TEOS volume and stirred at 500 rpm at room temperature. The exact TEOS volumes are given in Table 7.2.

Table 7.2.: Parameters for the synthesis of PS@SiO$_2$ particles with different shell thicknesses.

Sample	c$_{PS}$ [wt.%]	V$_{TEOS}$ [mL]	expected shell thickness [nm]
PS@SiO$_2$ **A**	9.15	6.6	15
PS@SiO$_2$ **B**	9.15	14.2	25
PS@SiO$_2$ **C**	9.15	22.9	35

After equilibrating for 20 min, 20.8 mL ammonia was added. The remaining TEOS was added in nine steps in time intervals of 15 min and the reaction was stirred over night. The particles were centrifuged and washed one time with ethanol and three times with water for purification. The freeze dried particles were then calcined at 550 °C for 5 h to get silica hollow spheres.

SiO$_2$-Ph precursor particles. Silica precursor particles with a covalently bonded phenylic group distributed inside the particle structure were synthesized with a modified instruction of Hatakeyama et al.[114] and Seog et al.[115] Ammonia was mixed with water and stirred at room temperature for 20 min to equilibrate the solution. Then, the desired amount of PTMS and TEOS were added quickly, one after the other. The reaction was stirred at 550 rpm for 10 minutes. Afterwards, the stirring was shut off, and the mixture was allowed to ripen overnight. The resulting particles were washed two times with H$_2$O and then dried on a heating plate. In Table 7.3 all concentrations and volumes of the reagents are shown.

For the carbothermal reaction, the particles were placed in an alumina boat in a tube furnace. They were heated to 1500 °C with 20 K min^{-1} in a N$_2$ or Ar atmosphere with a continuous gas flow of 50 mL min^{-1}. After cooling down, the particles were heated again to 800 °C for 4 h in air to burn most of the excess carbon away.

7.3 Sample preparation

Particle assembly. Highly ordered colloidal particle assemblies (colloidal crystals) were prepared by two different methods. First, an evaporation induced process was used to self-assemble polymer particles.[154] For this, small Teflon™beakers were filled with 5 mL of 10 wt.% polymer dispersion and placed in the fume hood for several days until the water was evaporated and a closed packed colloidal crystal was formed. Second, a centrifugation assisted assemble technique[86,155] was applied. The cavaties of spot plates were filled with 1.5 mL polymer dispersion and centrifuged with 1500 rpm for 18 h. The supernatant solvent was removed and the colloidal crystals were dried in the fume hood over night. The used particle sizes are depicted in Table 7.4.

Infiltration process. The solution for the SiO$_2$/C precursor was mixed according to Wang and Stein.[248] For a typical procedure, 1.25 g Pluronic® F-127 was mixed with 0.5 g phenol formaldehyde resin, 2.77 mL TEOS and 0.51 g 0.2 M hydrochloric acid and dissolved via ultrasonication. Small pieces of colloidal crystals were then deposited in this solution for 24 h. After impregnation, the fragments were carefully

Table 7.3.: Concentrations and volumes of the educts in the performed syntheses.

Experiment	V_{total} [mL]	c_{NH_3} [mol L^{-1}]	c_{TEOS} [mol L^{-1}]	c_{PTMS} [mol L^{-1}]	c_{H_2O} [mol L^{-1}]
A	15	0.25	0.0625	0.25	55.5
B	15	0.5	0.0625	0.25	55.5
C	15	1.0	0.0625	0.25	55.5
D	15	2.0	0.0625	0.25	55.5
E	15	0.5	0.125	0.25	55.5
F	15	0.5	0.25	0.25	55.5
G	15	0.5	0.5	0.25	55.5
H	15	0.5	1.0	0.25	55.5
I	15	0.5	0.0625	0.15	55.5
J	15	0.5	0.0625	0.25	55.5
K	15	0.5	0.0625	0.35	55.5
L	15	0.5	0.0625	0.45	55.5
M	15	0.5	0.0625	0.55	55.5
N	14.55	0.5	0.0625	0.25	55.5
O	38.5	0.5	0.0625	0.25	55.5
P	90.8	0.5	0.0625	0.25	55.5
Q	150	0.5	0.0625	0.25	55.5

removed and dried for 12 h at room temperature and 24 h at 80 °C in a drying closet. For pyrolysis, the samples were heated to 700 °C for 2 h with a heating rate of 60 °C h^{-1} in argon. In this process, the PS spheres and the triblock copolymer F127 was removed and the resin was transformed to carbon.

Magnesiothermic conversion of the precursor to SiC. The SiO$_2$/C precursor inverse opals were weighed and mixed with magnesium[121] turnings, which have 0.9 x the weight of the inverse opals, in an alumina boat. The boat was then loaded into a tube furnace and heated up to 700 °C for 12 h with a constant argon flow at a heating rate of 300 °C h^{-1} for magnesiothermic reduction. The resulting samples were washed with 0.1 M HCl to remove Mg residues or the byproduct MgO and with acetone for purification.

Table 7.4.: Diameters of the positively charged polystyrene particles used for colloidal crystal assembly.

Sample	Particle diameter [nm]	σ [%]
PS01	144 ± 4	2.64
PS02	163 ± 8	4.62
PS03	347 ± 7	3.74
PS04	363 ± 5	3.32
PS05	473 ± 22	6.71
PS06	712 ± 20	2.84
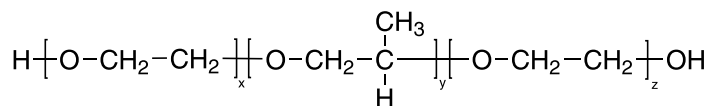
Figure 7.1.: Chemical structure of Pluronic®F-127.

SMP-10. Colloidal crystals were infiltrated with the preceramic precursor polymer SMP-10 from Starfire Systems by deposting small pieces of the colloidal material into the liquid polymer for several days. The fragments were removed and the redundant material was carefully removed with a tissue. For pyrolysis to amorphous SiC, the samples were heated with a constant argon flow in alumina boats to $650\,°C$ with a heating rate of $1\,\mathrm{K\,min^{-1}}$, holded at this temperature for 1 h, then heated to $850\,°C$ with $3\,\mathrm{K\,min^{-1}}$ and finally cooled down again. The second step to polycrystalline SiC was conducted with a heating rate $3\,\mathrm{K\,min^{-1}}$ from room temperature to $1600\,°C$. After reaching the end temperature an isothermal step for 2 h was applied, before a subsequent cool down.

Diffusion process. PS colloidal dispersion were centrifuged at 1500 rpm for 18 h. The supernantant solution was removed and the spots were carefully filled again with 1.5 mL of an ethanol/water mixture in a volume ratio of 4:3 and centrifuged again for 2 h. The next cycles were performed with a mixture of TEOS/ethanol/water (6:4:3) and a mixture of TEOS/ethanol/water/0.2 M HCl (6:4:3:1). After removing of the supernantant the samples were dried in air over night. The PS template was removed by calcination in air with heating segments from RT to $300\,°C$ with a heating rate of $2\,°\mathrm{C\,min^{-1}}$, an isothermal step for 2 h, an increase to $550\,°C$ with $2\,°\mathrm{C\,min^{-1}}$, followed by an isothermal step for 10 h, and then cooling down to ambient again. The SiC precursor consist out of a mixture of PTMS/TEOS/ethanol/water/0.2 M HCl

(6:4:4:3:1). The pyrolysis was carried out in argon atmosphere. The temperature was increased to 1500 °C with a heating rate of 20 °C min^{-1} and holded there for 4 h, before cooling down again. The precursor mixture for TiO$_2$ was composed out of Ti(OBu)$_4$ and EtOH in a volume ratio of 1:1. Calcination was carried out in air from ambient temperature to 300 °C with a heating rate of 2 °C min^{-1}, followed by an isothermal step for 2 h, a second heating step to 400 °C, again an isothermal step for 2 h, and then cooled down again.

Infiltration of colloidal crystals using vacuum suction. Dried pieces of colloidal crystals were placed in a Büchner funnel. The same ceramic precursor solutions already mentioned in the paragraph above, were added dropwise onto the pieces. The applied vacuum suction helps to infiltrate the colloidal crystals with the respective solution.

Fiber fabrication. Fibers were produced with a commercial available BD-130 airbrush from Fengda. 5 mL of the following polymer solutions were prepared for the solution blow spinning with the respective pressure applied in the process: a) 14 wt.% PVA ($\sim$ 67000 g mol^{-1}) in H$_2$O, 1.4 bar; b) 7 wt.% PVP ($\sim$ 1300000 g mol^{-1}) in EtOH, 1.4 bar; c) same as b) plus additional 0.5 mL of PS particle dispersion in water (0.202 μm, 5 % w/v, Microparticles GmbH), 1.4 bar; d) a mixture of b) and a silica precursor solution (4 mL EtOH, 2 mL 0.1 M HCl, 2 mL TEOS) in a volume ratio of 4:1, 1.0 bar. All fibers were sprayed onto glass slides in around 20 cm distance to the nozzle of the airbrush. The sample with the silica precursor was later calcined in a muffle furnace 550 °C for 5 h in air. A second setup with a self-made channel system according to a published microfluidic device[269] was 3D printed. The channel diameter for the polymer solution had a diameter of 500 μm. The air channel was adjusted to a conical shape, which reduces towards the outlet.

7.4 Methods

Simultaneous thermal analysis. A Netzsch model STA 449 F3 coupled with a Bruker Alpha II FT-IR spectrometer was used for thermal characterization. The measurements were performed in Al$_2$O$_3$ crucibles to 1300 °C, 1400 °C, and 1500 °C with a heating rate of 20 K min^{-1} in N$_2$ and Ar atmosphere.

Scanning electron microscopy. Images were taken with a Zeiss Ultra plus (Carl Zeiss AG) at an operating voltage of 3 kV and with in-lens or secondary electron detection after sputtering with 2 nm of platinum. For EDS analysis, the

particles were prepared onto TEM Cu grids (Plano GmbH) with a carbon film and investigated with an operating voltage of 10 kV with a STEM sample holder to reduce the background. A Thermo Scientific$^{\text{TM}}$ UltraDry$^{\text{TM}}$ EDS X-ray detector was used.

Field flow fractionation. The AF4 experiments were carried out with the EAF2000 electrical flow FFF (Postnova). The channel length was 28 cm, and the spacer was 350 μm. A regenerated cellulose membrane with 10 kDa molecular weight cutoff was used. Flow rates were regulated with PN1130 isocratic pumps equipped with a vacuum degasser. All injections were performed with an autosampler. The elution was monitored at 254 nm by a PN3211 UV detector, a multi angle light scattering detector (PN3621) and a Malvern Zetasizer Nano Series$^{\text{®}}$ for continuous DLS measurements. An overview of all measurement parameters is given in Table 7.5. The cross flow type in the elution step can be either constant (const.) or decreases with an exponential decay over a certain amount of time (power exponent).

Between the measurements a rinsing step was included, to wash off any sort of residue on the membrane.

For size determination the light scattering detector was calibrated with a latex particle standard mixture (60 nm, 125 nm and 350 nm geometric diameter) and the particle scattering function was calculated by the software. The elugrams were shifted to the start of the void peak to highlight differences in elution time.

Density analysis. The measurements were carried out with a Quantachrome Ultrapyc 1200e in Helium gas.

Differential scanning calorimetry. Measurements were performed with a DSC 2500 from TA Instruments, and the specific heat was calculated according to ASTM E 1269.

X-ray powder diffraction. Patterns were recorded in Bragg-Brentano geometry on an Empyrean diffractometer (PANalytical B.V.; Netherlands) using Cu-Kα radiation ($\lambda = 1.54187$ Å). If needed, the data were corrected for amorphous background and indexed with the software provided on the instrument.

Thermal conductivity and effusivity. The data was determined with the C-Term TCi Thermal Conductivity Analyzer. Samples were tested with 5 N compression.

Fourier transform infrared spectroscopy. Standard measurements were conducted on the dried samples in attenuated total reflectance (ATR) mode on a Bruker Vertex70 Spectrometer from $7500\,\text{cm}^{-1}$ to $380\,\text{cm}^{-1}$. For each spectrum, 64 scans were averaged, and a spectral resolution of $4\,\text{cm}^{-1}$ was used. Additionally, a

Table 7.5.: Specific measurement parameters for all performed FFF analysis of the gradient particles, the ellipsoidal particles, PS@SiO$_2$ core-shell particles and the SiO$_2$ hollow spheres.

		Gradient	Ellipsoids	PS@SiO$_2$	SiO$_2$-HS
General					
Injection volume [μL]		20	20	20	20
Concentration [% w/w]		0.1	0.05/0.1	0.01	—
Detector flow [mL min^{-1}]		0.5	0.5	0.5	0.5
Eluent		H$_2$O	0.2 % v/v Novachem in H$_2$O	1 mM KNO$_3$ in H$_2$O	H$_2$O
Focus step					
Delay time [min]		1.5	3	3	1
Injection flow [mL min^{-1}]		0.2	0.1	0.2	0.2
Injection time [min]		3	5	6	5
Cross flow [mL min^{-1}]		1.0	0.7	0.8	1.5
Focus flow [mL min^{-1}]		1.3	1.1	1.1	1.8
Transition time [min]		0.2	0.2	0.5	0.5
Elution step					
1	Time [min]	0.2	1	0.2	0.2
	Cross flow [mL min^{-1}]	1.0	0.7	0.8	1.5
	Type	const.	const.	const.	const.
2	Time [min]	40	45	10	30
	Cross flow [mL min^{-1}]	1.0	0.7	0.8	1.5
	Type	Power 0.2	Power 0.2	Power 0.1	Power 0.1
3	Time [min]	10	5	65	10
	Cross flow [mL min^{-1}]	0.1	0.1	0.2	0.1
	Type	const.	const.	const.	const.
	Current [mA]	—	—	0/0.5/1/1.5	—

gold-coated integrating sphere accessory (A562, Bruker) was used for reflection and transmission measurements.

UV/Vis spectroscopy. Measurements were done with a Cary 5000 (Agilent Technologies) UV/Vis spectrometer equipped with an integrating sphere accessory (Labspheres) at the reflection or transmission port. As a reflection reference, a Spectralon diffuse reflectance standard (Labspheres) was used.

Small angle x-ray scattering. SAXS measurements were performed on freeze-dried samples in 1 mm glass capillaries at room temperature in a transmission geometry using a Double Ganesha AIR system (SAXSLAB). The X-ray source in this system is a rotating anode (copper, MicoMax 007HF, Rigaku Corporation). Data was recorded using a position-sensitive detector (PILATUS 300 K, Dectris). Different detector positions were used to cover scattering vectors q between 0.0024 and 0.5 $Å^1$. The radially averaged data were normalized to the incident beam and sample thickness and the fitting was performed using the software Scatter.

Transmission electron microscopy. Measurements were performed with a JEOL JEM-1400 Plus at an operating voltage of 120 kV. Samples were prepared by dropping 10 μL of a diluted colloidal dispersion of redispersed silica hollow nanoparticles onto carbon coated copper grids. After 10 s, the excess solution was blotted with filter paper.

Nitrogen sorption. Measurements were carried out on a Quantachrome Autosorb AS-1 pore analyzer at 77 K. Prior to the measurements, all samples were preconditioned in a vacuum at 120 °C for 12 h. For the analysis, the Quantachrome ASiQ v3.0 software was used. The specific surface areas were calculated using the BET method.

Thermal treatment. The reactions were performed in an alumina boat inside a Nabertherm RHTC-50-150/17 tube furnace with a heating rate of 20 K min-1 in N_2 and Ar atmosphere at 1500 °C.

Particle diameter evaluation. The diameter of the particles was evaluated using a MATLAB circle detection function of at least 150 particles. The search parameters were optimized manually.

3D printing. A Keyence AGILISTA-3110W was used to print the solution blow spinning setup. AR-M2 was used as the polymer and the water soluble AR-S1 was used as support material.

Bibliography

[1] T. Feller, S. Rosenfeldt, M. Retsch, "Carbothermal synthesis of micron-sized, uniform, spherical silicon carbide (SiC) particles", *Zeitschrift für anorganische und allgemeine Chemie* **2021**, *647*, 2172–2180.

[2] M. Santamouris, *Energy and Climate in the Urban Built Environment*, Routledge, London, **2013**.

[3] OECD/IEA, *The Future of Cooling: Opportunities for energy-efficient air conditioning*, International Energy Agency, **2018**.

[4] M. O. McLinden, M. L. Huber, "(R)Evolution of Refrigerants", *Journal of Chemical & Engineering Data* **2020**, *65*, 4176–4193.

[5] H. Zhang, K. C. S. Ly, X. Liu, Z. Chen, M. Yan, Z. Wu, X. Wang, Y. Zheng, H. Zhou, T. Fan, "Biologically inspired flexible photonic films for efficient passive radiative cooling", *Proceedings of the National Academy of Sciences* **2020**, *117*, 14657–14666.

[6] N. N. Shi, C. C. Tsai, F. Camino, G. D. Bernard, N. Yu, R. Wehner, "Keeping cool: Enhanced optical reflection and radiative heat dissipation in Saharan silver ants", *Science* **2015**, *349*, 298–301.

[7] A. Didari, M. P. Menguc, "A biomimicry design for nanoscale radiative cooling applications inspired by Morpho didius butterfly", *Scientific Reports* **2018**, *8*, 16891.

[8] X. Yu, J. Chan, C. Chen, "Review of radiative cooling materials: Performance evaluation and design approaches", *Nano Energy* **2021**, *88*, 106259.

[9] C. Rockstuhl, M. G. Salt, H. P. Herzig, "Analysis of the phonon-polariton response of silicon carbide microparticles and nanoparticles by use of the boundary element method", *Journal of the Optical Society of America B - Optical Physics* **2005**, *22*, 481–487.

[10] C. Kittel, *Einführung in die Festkörperphysik*, De Gruyter Oldenbourg, **1980**.

[11] M. F. Modest, *Radiative Heat Transfer*, Academic Press Elsevier, **2013**.

[12] S. Catalanotti, V. Cuomo, G. Piro, D. Ruggi, V. Silvestrini, G. Troise, "The radiative cooling of selective surfaces", *Solar Energy* **1975**, *17*, 83–89.

[13] B. Bartoli, S. Catalanotti, B. Coluzzi, V. Cuomo, V. Silvestrini, G. Troise, "Nocturnal and diurnal performances of selective radiators", *Applied Energy* **1977**, *3*, 267–286.

[14] M. M. Hossain, M. Gu, "Radiative Cooling: Principles, Progress, and Potentials", *Advanced Science* **2016**, *3*, 1500360.

[15] B. Zhao, M. Hu, X. Ao, N. Chen, G. Pei, "Radiative cooling: A review of fundamentals, materials, applications, and prospects", *Applied Energy* **2019**, *236*, 489–513.

[16] A. Berk, P. Conforti, R. Kennett, T. Perkins, F. Hawes, J. van den Bosch in 2014 6th Workshop on Hyperspectral Image and Signal Processing: Evolution in Remote Sensing (WHISPERS), IEEE, **2014**.

[17] C. G. Granqvist, "Radiative heating and cooling with spectrally selective surfaces", *Applied Optics* **1981**, *20*, 2606–2615.

[18] A. P. Raman, M. A. Anoma, L. Zhu, E. Rephaeli, S. Fan, "Passive radiative cooling below ambient air temperature under direct sunlight", *Nature* **2014**, *515*, 540–544.

[19] B. Bhatia, A. Leroy, Y. Shen, L. Zhao, M. Gianello, D. Li, T. Gu, J. Hu, M. Soljai, E. N. Wang, "Passive directional sub-ambient daytime radiative cooling", *Nature Communications* **2018**, *9*.

[20] S. Fan, W. Li, "Photonics and thermodynamics concepts in radiative cooling", *Nature Photonics* **2022**, *16*, 182–190.

[21] Z. Chen, L. Zhu, A. Raman, S. Fan, "Radiative cooling to deep sub-freezing temperatures through a 24-h day-night cycle", *Nature Communications* **2016**, *7*, 13729.

[22] L. Fan, W. Li, W. Jin, M. Orenstein, S. Fan, "Maximal nighttime electrical power generation via optimal radiative cooling", *Optics Express* **2020**, *28*, 25460.

[23] K.-T. Lin, J. Han, K. Li, C. Guo, H. Lin, B. Jia, "Radiative cooling: Fundamental physics, atmospheric influences, materials and structural engineering, applications and beyond", *Nano Energy* **2021**, *80*, 105517.

[24] K. Herrmann, T. Lauster, Q. Song, M. Retsch, "Homogeneous Polymer Films for Passive Daytime Cooling: Optimized Thickness for Maximized Cooling Performance", *Advanced Energy and Sustainability Research* **2021**, *3*, 2100166.

[25] J. Mandal, S. Du, M. Dontigny, K. Zaghib, N. Yu, Y. Yang, "$Li_4Ti_5O_{12}$: A Visible-to-Infrared Broadband Electrochromic Material for Optical and Thermal Management", *Advanced Functional Materials* **2018**, *28*.

[26] P. C. Hsu, C. Liu, A. Y. Song, Z. Zhang, Y. Peng, J. Xie, K. Liu, C. L. Wu, P. B. Catrysse, L. Cai, S. Zhai, A. Majumdar, S. Fan, Y. Cui, "A dual-mode textile for human body radiative heating and cooling", *Science Advances* **2017**, *3*, e1700895.

[27] J. Song, J. Seo, J. Han, J. Lee, B. J. Lee, "Ultrahigh emissivity of grating-patterned PDMS film from 8 to 13 micrometer wavelength regime", *Applied Physics Letters* **2020**, *117*, 094101.

[28] H. Zhao, Q. Sun, J. Zhou, X. Deng, J. Cui, "Switchable Cavitation in Silicone Coatings for Energy-Saving Cooling and Heating", *Advanced Materials* **2020**, *32*, 2000870.

[29] D. Chae, M. Kim, P. H. Jung, S. Son, J. Seo, Y. Liu, B. J. Lee, H. Lee, "Spectrally Selective Inorganic-Based Multilayer Emitter for Daytime Radiative Cooling", *ACS Applied Materials & Interfaces* **2020**, *12*, 8073–8081.

[30] G. J. Lee, Y. J. Kim, H. M. Kim, Y. J. Yoo, Y. M. Song, "Colored, Daytime Radiative Coolers with Thin-Film Resonators for Aesthetic Purposes", *Advanced Optical Materials* **2018**, *6*.

[31] W. J. M. Kort-Kamp, S. Kramadhati, A. K. Azad, M. T. Reiten, D. A. R. Dalvit, "Passive Radiative Thermostat Enabled by Phase-Change Photonic Nanostructures", *ACS Photonics* **2018**, *5*, 4554–4560.

[32] Y. Huang, L. Liu, M. Pu, X. Li, X. Ma, X. Luo, "A refractory metamaterial absorber for ultra-broadband, omnidirectional and polarization-independent absorption in the UV-NIR spectrum", *Nanoscale* **2018**, *10*, 8298–8303.

[33] N. Lee, B. Yoon, T. Kim, J. Y. Bae, J. S. Lim, I. Chang, H. H. Cho, "Multiple Resonance Metamaterial Emitter for Deception of Infrared Emission with Enhanced Energy Dissipation", *ACS Applied Materials & Interfaces* **2020**, *12*, 8862–8869.

[34] K. Sun, C. A. Riedel, Y. Wang, A. Urbani, M. Simeoni, S. Mengali, M. Zalkovskij, B. Bilenberg, C. H. de Groot, O. L. Muskens, "Metasurface Optical Solar Reflectors Using AZO Transparent Conducting Oxides for Radiative Cooling of Spacecraft", *ACS Photonics* **2017**, *5*, 495–501.

[35] N. W. Pech-May, T. Lauster, M. Retsch, "Design of Multimodal Absorption in the Mid-IR: A Metal Dielectric Metal Approach", *ACS Applied Materials & Interfaces* **2021**, *13*, 1921–1929.

[36] D. Xie, Z. Yang, X. Liu, S. Cui, H. Zhou, T. Fan, "Broadband omnidirectional light reflection and radiative heat dissipation in white beetles Goliathus goliatus", *Soft Matter* **2019**, *15*, 4294–4300.

[37] S. Wang, Y. Wang, Y. Zou, G. Chen, J. Ouyang, D. Jia, Y. Zhou, "Biologically Inspired Scalable-Manufactured Dual-layer Coating with a Hierarchical Micropattern for Highly Efficient Passive Radiative Cooling and Robust Superhydrophobicity", *ACS Applied Materials & Interfaces* **2021**, *13*, 21888–21897.

[38] L. Cai, A. Y. Song, P. Wu, P. C. Hsu, Y. Peng, J. Chen, C. Liu, P. B. Catrysse, Y. Liu, A. Yang, C. Zhou, C. Zhou, S. Fan, Y. Cui, "Warming up human body by nanoporous metallized polyethylene textile", *Nature Communications* **2017**, *8*, 496.

[39] L. Cai, A. Y. Song, W. Li, P. C. Hsu, D. Lin, P. B. Catrysse, Y. Liu, Y. Peng, J. Chen, H. Wang, J. Xu, A. Yang, S. Fan, Y. Cui, "Spectrally Selective Nanocomposite Textile for Outdoor Personal Cooling", *Advanced Materials* **2018**, *30*, e1802152.

[40] J. Tabor, K. Chatterjee, T. K. Ghosh, "Smart Textile-Based Personal Thermal Comfort Systems: Current Status and Potential Solutions", *Advanced Materials Technologies* **2020**, *5*.

[41] R. Hu, Y. Liu, S. Shin, S. Huang, X. Ren, W. Shu, J. Cheng, G. Tao, W. Xu, R. Chen, X. Luo, "Emerging Materials and Strategies for Personal Thermal Management", *Advanced Energy Materials* **2020**, *10*, 1903921.

[42] M. Muselli, "Passive cooling for air-conditioning energy savings with new radiative low-cost coatings", *Energy and Buildings* **2010**, *42*, 945–954.

[43] Q.-F. Guan, H.-B. Yang, C.-H. Yin, Z.-M. Han, K.-P. Yang, Z.-C. Ling, S.-H. Yu, "Nacre-Inspired Sustainable Coatings with Remarkable Fire-Retardant and Energy-Saving Cooling Performance", *ACS Materials Letters* **2021**, *3*, 243–248.

[44] J. Mandal, Y. Yang, N. Yu, A. P. Raman, "Paints as a Scalable and Effective Radiative Cooling Technology for Buildings", *Joule* **2020**, *4*, 1350–1356.

[45] L. Zhu, A. Raman, K. X. Wang, M. A. Anoma, S. Fan, "Radiative cooling of solar cells", *Optica* **2014**, *1*, 32.

[46] B. Zhao, M. Hu, X. Ao, Q. Xuan, G. Pei, "Spectrally selective approaches for passive cooling of solar cells: A review", *Applied Energy* **2020**, *262*, 114548.

[47] W. Li, M. Dong, L. Fan, J. J. John, Z. Chen, S. Fan, "Nighttime Radiative Cooling for Water Harvesting from Solar Panels", *ACS Photonics* **2020**, *8*, 269–275.

[48] E. A. Goldstein, A. P. Raman, S. Fan, "Sub-ambient non-evaporative fluid cooling with the sky", *Nature Energy* **2017**, *2*.

[49] D. Zhao, C. E. Martini, S. Jiang, Y. Ma, Y. Zhai, G. Tan, X. Yin, R. Yang, "Development of a single-phase thermosiphon for cold collection and storage of radiative cooling", *Applied Energy* **2017**, *205*, 1260–1269.

[50] D. Zhao, A. Aili, Y. Zhai, J. Lu, D. Kidd, G. Tan, X. Yin, R. Yang, "Subambient Cooling of Water: Toward Real-World Applications of Daytime Radiative Cooling", *Joule* **2019**, *3*, 111–123.

[51] S. Atiganyanun, J. B. Plumley, S. J. Han, K. Hsu, J. Cytrynbaum, T. L. Peng, S. M. Han, S. E. Han, "Effective Radiative Cooling by Paint-Format Microsphere-Based Photonic Random Media", *ACS Photonics* **2018**, *5*, 1181–1187.

[52] H. H. Kim, E. Im, S. Lee, "Colloidal Photonic Assemblies for Colorful Radiative Cooling", *Langmuir* **2020**, *36*, 6589–6596.

[53] Y. Zhai, Y. Ma, S. N. David, D. Zhao, R. Lou, G. Tan, R. Yang, X. Yin, "Scalable-manufactured randomized glass-polymer hybrid metamaterial for daytime radiative cooling", *Science* **2017**, *355*, 1062–1066.

[54] Y. Liu, A. Bai, Z. Fang, Y. Ni, C. Lu, Z. Xu, "A Pragmatic Bilayer Selective Emitter for Efficient Radiative Cooling under Direct Sunlight", *Materials* **2019**, *12*, 1208.

[55] J. Jaramillo-Fernandez, G. L. Whitworth, J. A. Pariente, A. Blanco, P. D. Garcia, C. Lopez, C. M. Sotomayor-Torres, "A Self-Assembled 2D Thermofunctional Material for Radiative Cooling", *Small* **2019**, *15*, e1905290.

[56] E. Rephaeli, A. Raman, S. Fan, "Ultrabroadband photonic structures to achieve high-performance daytime radiative cooling", *Nano Letters* **2013**, *13*, 1457–1461.

[57] A. R. Gentle, G. B. Smith, "Radiative heat pumping from the Earth using surface phonon resonant nanoparticles", *Nano Letters* **2010**, *10*, 373–379.

[58] H. Bao, C. Yan, B. Wang, X. Fang, C. Y. Zhao, X. Ruan, "Double-layer nanoparticle-based coatings for efficient terrestrial radiative cooling", *Solar Energy Materials and Solar Cells* **2017**, *168*, 78–84.

[59] T. Suichi, A. Ishikawa, T. Tanaka, Y. Hayashi, K. Tsuruta, "Whitish daytime radiative cooling using diffuse reflection of non-resonant silica nanoshells", *Scientific Reports* **2020**, *10*, 6486.

[60] S. K. Andersson, G. A. Niklasson, "Influence of surface roughness on the infrared reststrahlen band", *Journal of Physics: Condensed Matter* **1995**, *7*, 7173–7184.

[61] S. Dai, Z. Fei, Q. Ma, A. S. Rodin, M. Wagner, A. S. McLeod, M. K. Liu, W. Gannett, W. Regan, K. Watanabe, T. Taniguchi, M. Thiemens, G. Dominguez, A. H. C. Neto, A. Zettl, F. Keilmann, P. Jarillo-Herrero, M. M. Fogler, D. N. Basov, "Tunable Phonon Polaritons in Atomically Thin van der Waals Crystals of Boron Nitride", *Science* **2014**, *343*, 1125–1129.

[62] J. D. Caldwell, O. J. Glembocki, Y. Francescato, N. Sharac, V. Giannini, F. J. Bezares, J. P. Long, J. C. Owrutsky, I. Vurgaftman, J. G. Tischler, V. D. Wheeler, N. D. Bassim, L. M. Shirey, R. Kasica, S. A. Maier, "Low-loss, extreme subdiffraction photon confinement via silicon carbide localized surface phonon polariton resonators", *Nano Letters* **2013**, *13*, 3690–3697.

[63] M. Haraguchi, M. Fukui, S. Muto, "Experimental observation of attenuated-total-reflection spectra of GaAs/AlAs superlattice", *Physical Review B* **1990**, *41*, 1254–1257.

[64] J. D. Caldwell, L. Lindsay, V. Giannini, I. Vurgaftman, T. L. Reinecke, S. A. Maier, O. J. Glembocki, "Low-loss, infrared and terahertz nanophotonics using surface phonon polaritons", *Nanophotonics* **2015**, *4*, 44–68.

[65] A. D. Boardman, *Electromagnetic Surface Modes*, John Wiley & Sons Ltd, **1982**.

[66] R. Hillenbrand, T. Taubner, F. Keilmann, "Phonon-enhanced light-matter interaction at the nanometre scale", *Nature* **2002**, *418*, 159–162.

[67] J. J. Greffet, R. Carminati, K. Joulain, J. P. Mulet, S. Mainguy, Y. Chen, "Coherent emission of light by thermal sources", *Nature* **2002**, *416*, 61–64.

[68] J. Le Gall, M. Olivier, J. J. Greffet, "Experimental and theoretical study of reflection and coherent thermal emissionby a SiC grating supporting a surface-phonon polariton", *Physical Review B* **1997**, *55*, 10105–10114.

[69] D.-Z. A. Chen, G. Chen, "Measurement of silicon dioxide surface phonon-polariton propagation length by attenuated total reflection", *Applied Physics Letters* **2007**, *91*, 121906.

[70] Q. Zhao, J. Zhou, F. Zhang, D. Lippens, "Mie resonance-based dielectric metamaterials", *Materials Today* **2009**, *12*, 60–69.

[71] H. Mutschke, A. C. Andersen, D. Clement, T. Henning, G. Peiter, "Infrared properties of SiC particles", *Astronomy & Astrophysics* **1999**, *345*, 187–202.

[72] W. Stöber, A. Fink, E. Bohn, "Controlled growth of monodisperse silica spheres in the micron size range", *Journal of Colloid and Interface Science* **1968**, *26*, 62–69.

[73] U. Schubert in *The Sol-Gel Handbook*, Wiley-VCH Verlag GmbH & Co. KGaA, **2015**, pp. 1–28.

[74] Z. Wen, G. Lu, S. Cui, H. Kim, S. Ci, J. Jiang, P. T. Hurley, J. Chen, "Rational design of carbon network cross-linked SiSiC hollow nanosphere as anode of lithium-ion batteries", *Nanoscale* **2014**, *6*, 342–351.

[75] F. Tang, L. Li, D. Chen, "Mesoporous silica nanoparticles: synthesis, biocompatibility and drug delivery", *Advanced Materials* **2012**, *24*, 1504–1534.

[76] M. Yoshida, P. N. Prasad, "Sol-Gel-Processed SiO_2/TiO_2/Poly(vinylpyrrolidone) Composite Materials for Optical Waveguides", *Chemistry of Materials* **1996**, *8*, 235–241.

[77] K. Nakanishi, N. Tanaka, "Sol-Gel with Phase Separation. Hierarchically Porous Materials Optimized for High-Performance Liquid Chromatography Separations", *Accounts of Chemical Research* **2007**, *40*, 863–873.

[78] A. A. Issa, A. S. Luyt, "Kinetics of Alkoxysilanes and Organoalkoxysilanes Polymerization: A Review", *Polymers* **2019**, *11*, 537.

[79] S.-L. Chen, P. Dong, G.-H. Yang, J.-J. Yang, "Kinetics of Formation of Monodisperse Colloidal Silica Particles through the Hydrolysis and Condensation of Tetraethylorthosilicate", *Industrial & Engineering Chemistry Research* **1996**, *35*, 4487–4493.

[80] G. H. Bogush, M. A. Tracy, C. F. Zukoski, "Preparation of monodisperse silica particles: Control of size and mass fraction", *Journal of Non-Crystalline Solids* **1988**, *104*, 95–106.

[81] H. Giesche, "Synthesis of monodispersed silica powders I. Particle properties and reaction kinetics", *Journal of the European Ceramic Society* **1994**, *14*, 189–204.

[82] A. V. Helden, J. Jansen, A. Vrij, "Preparation and characterization of spherical monodisperse silica dispersions in nonaqueous solvents", *Journal of Colloid and Interface Science* **1981**, *81*, 354–368.

[83] D. Niu, Z. Ma, Y. Li, J. Shi, "Synthesis of Core-Shell Structured Dual-Mesoporous Silica Spheres with Tunable Pore Size and Controllable Shell Thickness", *Journal of the American Chemical Society* **2010**, *132*, 15144–15147.

[84] R. Vacassy, R. Flatt, H. Hofmann, K. Choi, R. Singh, "Synthesis of Microporous Silica Spheres", *Journal of Colloid and Interface Science* **2000**, *227*, 302–315.

[85] C. Graf, D. L. J. Vossen, A. Imhof, A. van Blaaderen, "A General Method To Coat Colloidal Particles with Silica", *Langmuir* **2003**, *19*, 6693–6700.

[86] A. Stein, B. E. Wilson, S. G. Rudisill, "Design and functionality of colloidal-crystal-templated materials–chemical applications of inverse opals", *Chemical Society Reviews* **2013**, *42*, 2763–2803.

[87] K. R. Phillips, *Sol-Gel Chemistry of Inverse Opals*, Harvard University, **2016**.

[88] C. I. Aguirre, E. Reguera, A. Stein, "Tunable Colors in Opals and Inverse Opal Photonic Crystals", *Advanced Functional Materials* **2010**, *20*, 2565–2578.

[89] C. Fenzl, T. Hirsch, O. S. Wolfbeis, "Photonic Crystals for Chemical Sensing and Biosensing", *Angewandte Chemie International Edition* **2014**, *53*, 3318–3335.

[90] K. R. Phillips, T. Shirman, M. Aizenberg, G. T. England, N. Vogel, J. Aizenberg, "Silica-titania hybrids for structurally robust inverse opals with controllable refractive index", *Journal of Materials Chemistry C* **2020**, *8*, 109–116.

[91] J. Bauer, J. Fiala, R. Hichová, "Natural α-silicon carbide", *American Mineralogist: Journal of Earth and Planetary Materials* **1963**, *48*, 620–634.

[92] S. E. Saddow, A. K. Agarwal, *Advances in Silicon Carbide Processing and Applications*, Artech House, Boston, **2004**.

[93] R. Gerhardt, *Properties and Applications of Silicon Carbide*, InTech, Rijeka, **2011**.

[94] N. G. Wright, A. B. Horsfall, K. Vassilevski, "Prospects for SiC electronics and sensors", *Materials Today* **2008**, *11*, 16–21.

[95] H.-K. Seong, H.-J. Choi, S.-K. Lee, J.-I. Lee, D.-J. Choi, "Optical and electrical transport properties in silicon carbide nanowires", *Applied Physics Letters* **2004**, *85*, 1256–1258.

[96] L. Gu, Y. Wang, Y. Fang, R. Lu, J. Sha, "Performance characteristics of supercapacitor electrodes made of silicon carbide nanowires grown on carbon fabric", *Journal of Power Sources* **2013**, *243*, 648–653.

[97] A. F. Holleman, E. Wiberg, N. Wiberg, G. Fischer, *Lehrbuch der Anorganischen Chemie*, 102nd ed., De Gruyter, **2008**.

[98] J. A. Lely, *US Pat.*, US2854364A, **1955**.

[99] G. T. Burns, R. B. Taylor, Y. R. Xu, A. Zangvil, G. A. Zank, "High-Temperature Chemistry of the Conversion of Siloxanes to Silicon-Carbide", *Chemistry of Materials* **1992**, *4*, 1313–1323.

[100] R. M. Laine, F. Babonneau, "Preceramic Polymer Routes to Silicon-Carbide", *Chemistry of Materials* **1993**, *5*, 260–279.

[101] L. V. Interrante, C. W. Whitmarsh, W. Sherwood, H. J. Wu, R. Lewis, G. Maciel, "High Yield Polycarbosilane Precursors to Stoichiometric SiC. Synthesis, Pyrolysis and Application", *MRS Proceedings* **2011**, *346*.

[102] L. He, Z. Zhang, X. Yang, L. Jiao, Y. Li, C. Xu, "Liquid polycarbosilanes: synthesis and evaluation as precursors for SiC ceramic", *Polymer International* **2015**, *64*, 979–985.

[103] M. O. de Vries, S.-i. Sato, T. Ohshima, B. C. Gibson, J.-M. Bluet, S. Castelletto, B. C. Johnson, P. Reineck, "Fluorescent Silicon Carbide Nanoparticles", *Advanced Optical Materials* **2021**, *9*, 1–20.

[104] S. Yang, B. Kiraly, W. Y. Wang, S. Shang, B. Cao, H. Zeng, Y. Zhao, W. Li, Z.-K. Liu, W. Cai, T. J. Huang, "Fabrication and Characterization of Beaded SiC Quantum Rings with Anomalous Red Spectral Shift", *Advanced Materials* **2012**, *24*, 5598–5603.

[105]   H. Lin, J. A. Gerbec, M. Sushchikh, E. W. McFarland, "Synthesis of amorphous silicon carbide nanoparticles in a low temperature low pressure plasma reactor", *Nanotechnology* **2008**, *19*, 325601.

[106]   Y. Zakharko, T. Serdiuk, T. Nychyporuk, A. Géloën, M. Lemiti, V. Lysenko, "Plasmon-Enhanced Photoluminescence of SiC Quantum Dots for Cell Imaging Applications", *Plasmonics* **2012**, *7*, 725–732.

[107]   X. L. Wu, J. Y. Fan, T. Qiu, X. Yang, G. G. Siu, P. K. Chu, "Experimental Evidence for the Quantum Confinement Effect in 3C-SiC Nanocrystallites", *Physical Review Letters* **2005**, *94*, 026102.

[108]   B. M. Madhusudan, H. P. Raju, S. Ghanaraja, G. N. Sudhakar, "Study of Microstructure and Mechanical Properties of Ball milled Nano-SiC Reinforced Aluminium Matrix Composites", *Journal of The Institution of Engineers (India): Series D* **2021**, *102*, 167–172.

[109]   R. A. Cutler, K. M. Rigtrup, A. V. Virkar, "Synthesis, Sintering, Microstructure, and Mechanical Properties of Ceramics Made by Exothermic Reactions", *Journal of the American Ceramic Society* **1992**, *75*, 36–43.

[110]   C. J. Brinker, G. W. Scherer, *Sol-Gel Science : The Physics and Chemistry of Sol-Gel Processing*, Academic Press, Boston, **1990**.

[111]   V. Raman, O. P. Bahl, U. Dhawan, "Synthesis of silicon carbide through the sol-gel process from different precursors", *Journal of Materials Science* **1995**, *30*, 2686–2693.

[112]   Y. Zheng, Y. Zheng, L.-X. Lin, J. Ni, K.-M. Wei, "Synthesis of a novel mesoporous silicon carbide with a thorn-ball-like shape", *Scripta Materialia* **2006**, *55*, 883–886.

[113]   R. Z. Liu, M. L. Liu, J. X. Chang, "Large-scale synthesis of monodisperse SiC nanoparticles with adjustable size, stoichiometric ratio and properties by fluidized bed chemical vapor deposition", *Journal of Nanoparticle Research* **2017**, *19*.

[114]   F. Hatakeyama, S. Kanzaki, "Synthesis of Monodispersed Spherical β-Silicon Carbide Powder by a Sol-Gel Process", *Journal of the American Ceramic Society* **1990**, *73*, 2107–2110.

[115]   I. S. Seog, C. H. Kim, "Preparation of monodispersed spherical silicon carbide by the sol-gel method", *Journal of Materials Science* **1993**, *28*, 3277–3282.

[116]   Z. Bao, M. R. Weatherspoon, S. Shian, Y. Cai, P. D. Graham, S. M. Allan, G. Ahmad, M. B. Dickerson, B. C. Church, Z. Kang, 3. Abernathy, H. W., C. J. Summers, M. Liu, K. H. Sandhage, "Chemical reduction of three-dimensional silica micro-assemblies into microporous silicon replicas", *Nature* **2007**, *446*, 172–175.

[117]   J. Ahn, H. S. Kim, J. Pyo, J.-K. Lee, W. C. Yoo, "Variation in Crystalline Phases: Controlling the Selectivity between Silicon and Silicon Carbide via Magnesiothermic Reduction using Silica/Carbon Composites", *Chemistry of Materials* **2016**, *28*, 1526–1536.

[118]   B. Zhao, H. Zhang, H. Tao, Z. Tan, Z. Jiao, M. Wu, "Low temperature synthesis of mesoporous silicon carbide via magnesiothermic reduction", *Materials Letters* **2011**, *65*, 1552–1555.

[119] K. Chen, Z. Bao, A. Du, X. Zhu, G. Wu, J. Shen, B. Zhou, "Synthesis of resor-cinolformaldehyde/silica composite aerogels and their low-temperature conversion to mesoporous silicon carbide", *Microporous and Mesoporous Materials* **2012**, *149*, 16–24.

[120] T.-D. Nguyen, J. A. Kelly, W. Y. Hamad, M. J. MacLachlan, "Magnesiothermic Reduction of Thin Films: Towards Semiconducting Chiral Nematic Mesoporous Silicon Carbide and Silicon Structures", *Advanced Functional Materials* **2015**, *25*, 2175–2181.

[121] Y. Shi, F. Zhang, Y. S. Hu, X. Sun, Y. Zhang, H. I. Lee, L. Chen, G. D. Stucky, "Low-temperature pseudomorphic transformation of ordered hierarchical macro-mesoporous SiO_2/C nanocomposite to SiC via magnesiothermic reduction", *Journal of the American Chemical Society* **2010**, *132*, 5552–5553.

[122] M. Dasog, L. F. Smith, T. K. Purkait, J. G. Veinot, "Low temperature synthesis of silicon carbide nanomaterials using a solid-state method", *Chemical Communications* **2013**, *49*, 7004–7006.

[123] W. An, J. Su, Z. Chen, B. Gao, X. Zhang, X. Peng, S. Peng, J. Fu, P. K. Chu, F. Golestani-Fard, "Low-Temperature Synthesis of Mesoporous SiC Hollow Spheres by Magnesiothermic Reduction", *Journal of the American Ceramic Society* **2016**, *99*, 1859–1861.

[124] R. Cheung, *Silicon Carbide Microelectromechanical Systems for Harsh Environments*, Imperial College Press, London, **2006**.

[125] K. Momma, F. Izumi, "VESTA 3 for three-dimensional visualization of crystal, volumetric and morphology data", *Journal of Applied Crystallography* **2011**, *44*, 1272–1276.

[126] S. Janz, *Amorphous silicon carbide for photovoltaic applications*, Universität Konstanz, **2006**.

[127] W. A. Nevin, H. Yamagishi, M. Yamaguchi, Y. Tawada, "Emission of blue light from hydrogenated amorphous silicon carbide", *Nature* **1994**, *368*, 529–531.

[128] G. L. Harris, *Properties of Silicon Carbide*, Institute of Electrical Engineers of Japan, **1995**.

[129] J. W. Goodwin, J. Hearn, C. C. Ho, R. H. Ottewill, "Studies on the preparation and characterisation of monodisperse polystyrene laticee", *Colloid and Polymer Science* **1974**, *252*, 464–471.

[130] P. Ruckdeschel, *Transport Phenomena in Silica Hollow Spheres and Hybrid Materials*, Universität Bayreuth, **2018**.

[131] F. A. Nutz, M. Retsch, "Tailor-made temperature-dependent thermal conductivity via interparticle constriction", *Science Advances* **2017**, *3*.

[132] P. A. Lovell, F. J. Schork, "Fundamentals of Emulsion Polymerization", *Biomacromolecules*, *21*, 4396–4441.

[133] P. J. Feeney, D. H. Napper, R. G. Gilbert, "The determinants of latex monodispersity in emulsion polymerizations", *Journal of Colloid and Interface Science* **1987**, *118*, 493–505.

[134] M. S.-D. Juang, I. M. Krieger, "Emulsifier-free emulsion polymerization with ionic comonomer", *Journal of Polymer Science: Polymer Chemistry Edition* **1976**, *14*, 2089–2107.

[135] F. K. Hansen, J. Ugelstad, "Particle nucleation in emulsion polymerization. I. A theory for homogeneous nucleation", *Journal of Polymer Science: Polymer Chemistry Edition* **1978**, *16*, 1953–1979.

[136] K. E. J. Barrett, "Dispersion polymerisation in organic media", *British Polymer Journal* **1973**, *5*, 259–271.

[137] R. Arshady, "Suspension, emulsion, and dispersion polymerization: A methodological survey", *Colloid and Polymer Science* **1992**, *270*, 717–732.

[138] J.-H. Lee, J. P. Singer, E. L. Thomas, "Micro-/Nanostructured Mechanical Metamaterials", *Advanced Materials* **2012**, *24*, 4782–4810.

[139] P. Ruckdeschel, T. W. Kemnitzer, F. A. Nutz, J. Senker, M. Retsch, "Hollow silica sphere colloidal crystals: insights into calcination dependent thermal transport", *Nanoscale* **2015**, *7*, 10059–10070.

[140] Y. Xie, D. Kocaefe, C. Chen, Y. Kocaefe, "Review of Research on Template Methods in Preparation of Nanomaterials", *Journal of Nanomaterials* **2016**, *2016*, 1–10.

[141] P. Pieranski, "Two-Dimensional Interfacial Colloidal Crystals", *Physical Review Letters* **1980**, *45*, 569–572.

[142] H.-J. Butt, K. Graf, M. Kappl, *Physics and Chemistry of Interfaces*, Wiley, **2003**.

[143] B. Vincent, J. Edwards, S. Emmett, A. Jones, "Depletion flocculation in dispersions of sterically-stabilised particles (soft spheres)", *Colloids and Surfaces* **1986**, *18*, 261–281.

[144] X. Meng, D. Qiu, "Gas-Flow-Induced Reorientation to Centimeter-Sized Two-Dimensional Colloidal Single Crystal of Polystyrene Particle", *Langmuir* **2014**, *30*, 3019–3023.

[145] J. N. Israelachvili, *Intermolecular and Surface Forces*, 3rd ed., Academic Press Elsevier, **2011**.

[146] E. Dokou, M. A. Barteau, N. J. Wagner, A. M. Lenhoff, "Effect of Gravity on Colloidal Deposition Studied by Atomic Force Microscopy", *Journal of Colloid and Interface Science* **2001**, *240*, 9–16.

[147] E. Armstrong, W. Khunsin, M. Osiak, M. Blömker, C. M. S. Torres, C. O'Dwyer, "Ordered 2D Colloidal Photonic Crystals on Gold Substrates by Surfactant-Assisted Fast-Rate Dip Coating", *Small* **2014**, *10*, 1895–1901.

[148]   M. Retsch, Z. Zhou, S. Rivera, M. Kappl, X. S. Zhao, U. Jonas, Q. Li, "Fabrication of Large-Area, Transferable Colloidal Monolayers Utilizing Self-Assembly at the Air/Water Interface", *Macromolecular Chemistry and Physics* **2009**, *210*, 230–241.

[149]   A. Mihi, M. Ocaña, H. Míguez, "Oriented Colloidal-Crystal Thin Films by Spin-Coating Microspheres Dispersed in Volatile Media", *Advanced Materials* **2006**, *18*, 2244–2249.

[150]   J. Park, J. Moon, "Control of Colloidal Particle Deposit Patterns within Picoliter Droplets Ejected by Ink-Jet Printing", *Langmuir* **2006**, *22*, 3506–3513.

[151]   L. Cui, Y. Zhang, J. Wang, Y. Ren, Y. Song, L. Jiang, "Ultra-Fast Fabrication of Colloidal Photonic Crystals by Spray Coating", *Macromolecular Rapid Communications* **2009**, *30*, 598–603.

[152]   B. T. Holland, C. F. Blanford, A. Stein, "Synthesis of Macroporous Minerals with Highly Ordered Three-Dimensional Arrays of Spheroidal Voids", *Science* **1998**, *281*, 538–540.

[153]   C. Park, T. Lee, Y. Xia, T. J. Shin, J. Myoung, U. Jeong, "Quick, large-area assembly of a single-crystal monolayer of spherical particles by unidirectional rubbing", *Advanced Materials* **2014**, *26*, 4633–4638.

[154]   W. Guo, M. Wang, W. Xia, L. Dai, "Evaporation-induced self-assembly of capillary cylindrical colloidal crystal in a face-centered cubic structure with controllable thickness", *Journal of Materials Research* **2012**, *27*, 1663–1671.

[155]   M. Chen, H. Cölfen, S. Polarz, "Centrifugal Field-Induced Colloidal Assembly: From Chaos to Order", *ACS Nano* **2015**, *9*, 6944–6950.

[156]   G. Lozano, H. Míguez, "Relation between growth dynamics and the spatial distribution of intrinsic defects in self-assembled colloidal crystal films", *Applied Physics Letters* **2008**, *92*, 091904.

[157]   S. Gaisford, V. Kett, P. Haines, *Principles of Thermal Analysis and Calorimetry*, 2nd ed., Royal Society of Chemistry, **2016**.

[158]   A. Frick, C. Stern, *DSC-Prüfung in der Anwendung*, 2nd ed., Carl Hanser Verlag GmbH & Co. KG, **2013**.

[159]   P. Haines, *Principles of Thermal Analysis and Calorimetry*, Royal Society of Chemistry, **2002**.

[160]   H. Cölfen, M. Antonietti in *New Developments in Polymer Analytics I*, Springer Berlin Heidelberg, **2000**, pp. 67–187.

[161]   J. C. Giddings, "A New Separation Concept Based on a Coupling of Concentration and Flow Nonuniformities", *Separation Science* **1966**, *1*, 123–125.

[162]   J. C. Giddings, F. J. F. Yang, M. N. Myers, "Flow-Field-Flow Fractionation: A Versatile New Separation Method", *Science* **1976**, *193*, 1244–1245.

[163]   M. Schimpf, K. Caldwell, J. Giddings, *Field-Flow Fractionation Handbook*, 1st ed., Wiley & Sons Ltd, **2000**.

[164] J. Lohrke, A. Briel, K. Mäder, "Characterization of superparamagnetic iron oxide nanoparticles by asymmetrical flow-field-flow-fractionation", *Nanomedicine* **2008**, *3*, 437–452.

[165] A. Einstein, "Über die von der molekularkinetischen Theorie der Wärme geforderte Bewegung von in ruhenden Flüssigkeiten suspendierten Teilchen", *Annalen der Physik* **1905**, *322*, 549–560.

[166] M. von Smoluchowski, "Zur kinetischen Theorie der Brownschen Molekularbewegung und der Suspensionen", *Annalen der Physik* **1906**, *326*, 756–780.

[167] E. Abbe, "Beiträge zur Theorie des Mikroskops und der mikroskopischen Wahrnehmung", *Archiv für Mikroskopische Anatomie* **1873**, *9*, 413–468.

[168] P. W. Atkins, J. de Paula, *Physikalische Chemie*, 5th ed., Wiley-VCH, Weinheim, **2013**.

[169] G. H. Michler, *Electron Microscopy of Polymers*, Springer, Berlin, **2010**.

[170] J. I. Goldstein, D. E. Newbury, J. R. Michael, N. W. Ritchie, J. H. J. Scott, D. C. Joy, *Scanning Electron Microscopy and X-Ray Microanalysis*, 4th ed., Springer New York, **2018**.

[171] M. E. J. Hummel, C. Stelling, B. A. F. Kopera, F. A. Nutz, M. Karg, M. Retsch, S. Förster, "Ordered Particle Arrays via a Langmuir Transfer Process: Access to Any Two-Dimensional Bravais Lattice", *Langmuir* **2018**, *35*, 973–979.

[172] T. Honold, K. Volk, M. Retsch, M. Karg, "Binary plasmonic honeycomb structures: High-resolution EDX mapping and optical properties", *Colloids and Surfaces A: Physicochemical and Engineering Aspects* **2016**, *510*, 198–204.

[173] B. Schrader, *Infrared and Raman Spectroscopy: Methods and Applications*, Wiley-VCH, **1995**.

[174] R. Mecke, "Valenz- und Deformationsschwingungen einfacher Moleküle I. Allgemeine Theorie", *Zeitschrift für physikalische Chemie* **1932**, *16*, 409–420.

[175] P. R. Griffiths, J. A. De Haseth, J. D. Winefordner, *Fourier Transform Infrared Spectrometry*, 2nd ed., Wiley, **2007**.

[176] H.-H. Perkampus, *UV-Vis-Spektroskopie und ihre Anwendungen*, Springer, Berlin, **2012**.

[177] L. M. Hanssen, K. A. Snail, *Integrating Spheres for Mid- and Near-Infrared Reflection Spectroscopy*, (Ed.: P. R. Griffiths), John Wiley & Sons, Ltd, **2001**.

[178] M. Fox, *Optical Properties of Solids*, 2nd ed., Oxford University Press, **2010**, 416 pp.

[179] Z. Huang, X. Ruan, "Nanoparticle embedded double-layer coating for daytime radiative cooling", *International Journal of Heat and Mass Transfer* **2017**, *104*, 890–896.

[180] Z. Cheng, F. Wang, H. Wang, H. Liang, L. Ma, "Effect of embedded polydisperse glass microspheres on radiative cooling of a coating", *International Journal of Thermal Sciences* **2019**, *140*, 358–367.

[181] X. He, Y. Li, L. Wang, Y. Sun, S. Zhang, "High emissivity coatings for high temperature application: Progress and prospect", *Thin Solid Films* **2009**, *517*, 5120–5129.

[182] Z.-X. Jia, Y. Shuai, M. Li, Y. Guo, H.-p. Tan, "Enhancement radiative cooling performance of nanoparticle crystal via oxidation", *Journal of Quantitative Spectroscopy and Radiative Transfer* **2018**, *207*, 23–31.

[183] M. Schöttle, T. Tran, T. Feller, M. Retsch, "Time-Temperature Integrating Optical Sensors Based on Gradient Colloidal Crystals", *Advanced Materials* **2021**, *33*, 2101948.

[184] S. Jia, Z. Tang, Y. Guan, Y. Zhang, "Order-Disorder Transition in Doped Microgel Colloidal Crystals and Its Application for Optical Sensing", *ACS Applied Materials & Interfaces* **2018**, *10*, 14254–14258.

[185] M. Tsuchiya, Y. Kurashina, H. Onoe, "Eye-recognizable and repeatable biochemical flexible sensors using low angle-dependent photonic colloidal crystal hydrogel microbeads", *Scientific Reports* **2019**, *9*.

[186] L. Zhou, J. Rada, H. Song, B. Ooi, Z. Yu, Q. Gan, "Colorful surfaces for radiative cooling", *Journal of Photonics for Energy* **2021**, *11*, 042107.

[187] R. C. Nagarwal, S. Kant, P. Singh, P. Maiti, J. Pandit, "Polymeric nanoparticulate system: A potential approach for ocular drug delivery", *Journal of Controlled Release* **2009**, *136*, 2–13.

[188] C. Grosse, A. Delgado, "Dielectric dispersion in aqueous colloidal systems", *Current Opinion in Colloid & Interface Science* **2010**, *15*, 145–159.

[189] V. Wood, M. J. Panzer, J.-M. Caruge, J. E. Halpert, M. G. Bawendi, V. Bulovi, "Air-Stable Operation of Transparent, Colloidal Quantum Dot Based LEDs with a Unipolar Device Architecture", *Nano Letters* **2009**, *10*, 24–29.

[190] S. Barua, S. Mitragotri, "Synergistic Targeting of Cell Membrane, Cytoplasm, and Nucleus of Cancer Cells Using Rod-Shaped Nanoparticles", *ACS Nano* **2013**, *7*, 9558–9570.

[191] G. Jacucci, B. W. Longbottom, C. C. Parkins, S. A. F. Bon, S. Vignolini, "Anisotropic silica colloids for light scattering", *Journal of Materials Chemistry C* **2021**, *9*, 2695–2700.

[192] H. L. Leertouwer, B. D. Wilts, D. G. Stavenga, "Refractive index and dispersion of butterfly chitin and bird keratin measured by polarizing interference microscopy", *Optics Express* **2011**, *19*, 24061.

[193] F. Utel, L. Cortese, D. S. Wiersma, L. Pattelli, "Optimized White Reflectance in Photonic-Network Structures", *Advanced Optical Materials* **2019**, *7*, 1900043.

[194] R. Beckett, J. Giddings, "Entropic Contribution to the Retention of Nonspherical Particles in Field-Flow Fractionation", *Journal of Colloid and Interface Science* **1997**, *186*, 53–59.

[195] M. Alfi, J. Park, "Theoretical analysis of the local orientation effect and the lift-hyperlayer mode of rodlike particles in field-flow fractionation", *Journal of Separation Science* **2014**, *37*, 876–883.

[196] J. Chun, J. A. Fagan, E. K. Hobbie, B. J. Bauer, "Size separation of single-wall carbon nanotubes by flow-field flow fractionation", *Analytical Chemistry* **2008**, *80*, 2514–2523.

[197] S. Monjezi, M. Schneier, J. Choi, S. Lee, J. Park, "The shape effect on the retention behaviors of ellipsoidal particles in field-flow fractionation: Theoretical model derivation considering the steric-entropic mode", *Journal of Chromatography A* **2019**, *1587*, 189–196.

[198] S. Boye, F. Ennen, L. Scharfenberg, D. Appelhans, L. Nilsson, A. Lederer, "From 1D Rods to 3D Networks: A Biohybrid Topological Diversity Investigated by Asymmetrical Flow Field-Flow Fractionation", *Macromolecules* **2015**, *48*, 4607–4619.

[199] J. Satterly, "Formulae for Volumes, Surface Areas and Radii of Gyration of Spheres, Ellipsoids and Spheroids", *The Mathematical Gazette* **1960**, *44*, 15–19.

[200] L. A. Feigin, D. I. Svergun, *Structure Analysis by Small-Angle X-Ray and Neutron Scattering*, (Ed.: G. W. Taylor), Springer New York, **2013**, 352 pp.

[201] D. Hanaor, M. Michelazzi, C. Leonelli, C. C. Sorrell, "The effects of carboxylic acids on the aqueous dispersion and electrophoretic deposition of ZrO_2", *Journal of the European Ceramic Society* **2012**, *32*, 235–244.

[202] A. Kumar, C. K. Dixit in *Advances in Nanomedicine for the Delivery of Therapeutic Nucleic Acids*, Elsevier, **2017**, pp. 43–58.

[203] T. Lang, K. A. Eslahian, M. Maskos, "Ion Effects in Field-Flow Fractionation of Aqueous Colloidal Polystyrene", *Macromolecular Chemistry and Physics* **2012**, *213*, 2353–2361.

[204] J. Bertling, J. Blömer, R. Kümmel, "Hollow Microspheres", *Chemical Engineering & Technology* **2004**, *27*, 829–837.

[205] P. Ruckdeschel, M. Dulle, T. Honold, S. Förster, M. Karg, M. Retsch, "Monodisperse hollow silica spheres: An in-depth scattering analysis", *Nano Research* **2016**, *9*, 1366–1376.

[206] G. Xi, Y. Liu, X. Liu, X. Wang, Y. Qian, "Mg-Catalyzed Autoclave Synthesis of Aligned Silicon Carbide Nanostructures", *The Journal of Physical Chemistry B* **2006**, *110*, 14172–14178.

[207] H. Zhang, W. Ding, K. He, M. Li, "Synthesis and Characterization of Crystalline Silicon Carbide Nanoribbons", *Nanoscale Research Letters* **2010**, *5*, 1264–1271.

[208] D. N. Batchelder, R. O. Simmons, "Lattice Constants and Thermal Expansivities of Silicon and of Calcium Fluoride between 6 and 322 K", *The Journal of Chemical Physics* **1964**, *41*, 2324–2329.

[209] A. Jay, K. Andrews, *The Journal of the Iron and Steel Institute* **1946**, *152*, 15–18.

[210] A. B. Fuertes, P. Valle-Vigon, M. Sevilla, "One-step synthesis of silica@resorcinol-formaldehyde spheres and their application for the fabrication of polymer and carbon capsules", *Chemical Communications* **2012**, *48*, 6124–6126.

[211] B. Guan, X. Wang, Y. Xiao, Y. Liu, Q. Huo, "A versatile cooperative template-directed coating method to construct uniform microporous carbon shells for multifunctional core-shell nanocomposites", *Nanoscale* **2013**, *5*, 2469–2475.

[212] D. H. Filsinger, D. B. Bourrie, "Silica to Silicon: Key Carbothermic Reactions and Kinetics", *Journal of the American Ceramic Society* **1990**, *73*, 1726–1732.

[213] Y. Shi, Y. Meng, D. Chen, S. Cheng, P. Chen, H. Yang, Y. Wan, D. Zhao, "Highly Ordered Mesoporous Silicon Carbide Ceramics with Large Surface Areas and High Stability", *Advanced Functional Materials* **2006**, *16*, 561–567.

[214] F. Zong, C. Meng, Z. Guo, F. Ji, H. Xiao, X. Zhang, J. Ma, H. Ma, "Synthesis and characterization of magnesium nitride powder formed by Mg direct reaction with N_2", *Journal of Alloys and Compounds* **2010**, *508*, 172–176.

[215] J. D. Hanawalt, H. W. Rinn, L. K. Frevel, "Chemical Analysis by X-Ray Diffraction", *Industrial & Engineering Chemistry Analytical Edition* **1938**, *10*, 457–512.

[216] Y. Uenaka, T. Uchino, "Excitonic and Defect-Related Photoluminescence in Mg_3N_2", *The Journal of Physical Chemistry C* **2014**, *118*, 11895–11901.

[217] X. Liu, M. Antonietti, C. Giordano, "Manipulation of Phase and Microstructure at Nanoscale for SiC in Molten Salt Synthesis", *Chemistry of Materials* **2013**, *25*, 2021–2027.

[218] H. Brækken, "Ein Universal-Röntgenapparat für Kristallstrukturuntersuchungen", *Zeitschrift für Kristallographie - Crystalline Materials* **1932**, *81*, 309–313.

[219] T. Jermouni, M. Smaihi, N. Hovnanian, "Hydrolysis and Initial Polycondensation of Phenyltrimethoxysilane and Diphenyldimethoxysilane", *Journal of Materials Chemistry* **1995**, *5*, 1203–1208.

[220] C. Wu, Y. Wu, T. Xu, W. Yang, "Study of Sol-gel reaction of organically modified alkoxysilanes. Part I: Investigation of hydrolysis and polycondensation of phenylaminomethyl triethoxysilane and tetraethoxysilane", *Journal of Non-Crystalline Solids* **2006**, *352*, 5642–5651.

[221] M. Segers, N. Arfsten, P. Buskens, M. Möller, "A facile route for the synthesis of sub-micron sized hollow and multiporous organosilica spheres", *RSC Advances* **2014**, *4*, 20673–20676.

[222] J. Su, B. Gao, Z. Chen, J. Fu, W. An, X. Peng, X. Zhang, L. Wang, K. Huo, P. K. Chu, "Large-Scale Synthesis and Mechanism of β-SiC Nanoparticles from Rice Husks by Low-Temperature Magnesiothermic Reduction", *ACS Sustainable Chemistry & Engineering* **2016**, *4*, 6600–6607.

[223] A. M. Lechner, T. Feller, Q. Song, B. A. F. Kopera, L. Heindl, M. Drechsler, S. Rosenfeldt, M. Retsch, "Scalable synthesis of smooth $PS@TiO_2$ core-shell and TiO_2 hollow spheres in the (sub) micron size range: understanding synthesis and calcination parameters", *Colloid and Polymer Science* **2020**, *298*, 867–878.

[224] J. J. Biernacki, G. P. Wotzak, "Stoichiometry of the C + SiO$_2$ Reaction", *Journal of the American Ceramic Society* **1989**, *72*, 122–129.

[225] V. D. Krstic, "Production of Fine, High-Purity Beta Silicon Carbide Powders", *Journal of the American Ceramic Society* **1992**, *75*, 170–174.

[226] B. Zhang, J. Li, J. Sun, S. Zhang, H. Zhai, Z. Du, "Nanometer silicon carbide powder synthesis and its dielectric behavior in the GHz range", *Journal of the European Ceramic Society* **2002**, *22*, 93–99.

[227] B. Abolpour, R. Shamsoddini, "Mechanism of reaction of silica and carbon for producing silicon carbide", *Progress in Reaction Kinetics and Mechanism* **2019**, *45*, 1–14.

[228] F. L. Riley, "Silicon Nitride and Related Materials", *Journal of the American Ceramic Society* **2004**, *83*, 245–265.

[229] A. Chu, M. Qin, D. Li, H. Wu, Z. Cao, X. Qu, "Preparation of SiC nanopowder using low-temperature combustion synthesized precursor", *Materials Chemistry and Physics* **2014**, *144*, 560–567.

[230] N. W. Thibault, "Morphological and structural crystallography and optical properties of silicon carbide (SiC)", *American Mineralogist* **1944**, *29*, 327–362.

[231] A. L. Hannam, P. T. B. Shaffer, "Revised X-ray diffraction line intensities for silicon carbide polytypes", *Journal of Applied Crystallography* **1969**, *2*, 45–48.

[232] P. Krishna, A. R. Verma, "A new polytype of silicon carbide, 57R. Its structure and growth", *Acta Crystallographica* **1962**, *15*, 383–387.

[233] D. A. Norris, M. A. Rodriguez, S. K. Fukuda, R. L. Snyder, "X-Ray Powder Data for α-Si$_3$N$_4$", *Powder Diffraction* **1990**, *5*, 225–226.

[234] K. Koumoto, S. Takeda, C. H. Pai, T. Sato, H. Yanagida, "High-Resolution Electron Microscopy Observations of Stacking Faults in βSiC", *Journal of the American Ceramic Society* **1989**, *72*, 1985–1987.

[235] M. E. Levinshtein, S. L. Rumyantsev, M. Shur, *Properties of advanced semiconductor materials: GaN, AlN, InN, BN, SiC, SiGe*, Wiley, New York, **2001**.

[236] W. M. Haynes, D. R. Lide, *CRC Handbook of Chemistry and Physics*, 92nd ed., CRC Press, Boca Raton, Fl., **2011**.

[237] H. Moser, "Messung der wahren spezifischen Wärme von Silber, Nickel, beta-Messing, Quarzkrystall und Quarzglas zwischen +50 und 700 C nach einer verfeinerten Methode", *Physikalische Zeitschrift* **1937**, *37*, 737–753.

[238] K.-P. Jen, R. Warzoha, J. Guo, M. Tang, S. Santhanam, "Processing and Characterization of Silicon Nitride Nanofiber Paper", *Journal of Nanomaterials* **2013**, *2013*, 7.

[239] J. P. Dismukes, L. Ekstrom, E. F. Steigmeier, I. Kudman, D. S. Beers, "Thermal and Electrical Properties of Heavily Doped GeSi Alloys up to 1300 K", *Journal of Applied Physics* **1964**, *35*, 2899–2907.

[240] N. Mathis, "Transient thermal conductivity measurements: comparison of destructive and nondestructive techniques", *High Temperatures-High Pressures* **2000**, *32*, 321–327.

[241] D. J. Cumberland, R. J. Crawford, *The packing of particles*, Elsevier, Amsterdam, **1987**.

[242] G. Socrates, *Infrared and Raman Characteristic Group Frequencies: Tables and Charts*, 3rd, Wiley, **2004**.

[243] A. Kleinová, J. Huran, V. Sasinková, M. Perný, V. Sály, J. Packa, "FTIR spectroscopy of silicon carbide thin films prepared by PECVD technology for solar cell application", *Proceedings SPIE 9563*, Reliability of Photovoltaic Cells, Modules, Components, and Systems VIII, 95630U **2015**, (Eds.: N. G. Dhere, J. H. Wohlgemuth, R. Jones-Albertus).

[244] P. Innocenzi, "Infrared spectroscopy of solgel derived silica-based films: a spectra-microstructure overview", *Journal of Non-Crystalline Solids* **2003**, *316*, 309–319.

[245] P. J. Launer, B. Arkles in *Silicon Compounds: Silanes and Silicones*, Gelest Inc., Morrisville, PA, USA, **2013**, pp. 175–178.

[246] V. N. Antsiferov, V. G. Gilev, V. I. Karmanov, "Infrared Spectra and Structure of Si_3N_4, Si_2ON_2 and Sialons", *Refractories and Industrial Ceramics* **2003**, *44*, 108–114.

[247] N. Sun, X. Meng, Z. Xiao, "Functionalized Si_3N_4 nanoparticles modified with hydrophobic polymer chains by surface-initiated atom transfer radical polymerization (ATRP)", *Ceramics International* **2015**, *41*, 13830–13835.

[248] Z. Wang, A. Stein, "Morphology Control of Carbon, Silica, and Carbon/Silica Nanocomposites: From 3D Ordered Macro-/Mesoporous Monoliths to Shaped Mesoporous Particles", *Chemistry of Materials* **2007**, *20*, 1029–1040.

[249] Y. Xia, B. Gates, Y. Yin, Y. Lu, "Monodispersed Colloidal Spheres: Old Materials with New Applications", *Advanced Materials* **2000**, *12*, 693–713.

[250] P. G. Bolhuis, D. Frenkel, S.-C. Mau, D. A. Huse, "Entropy difference between crystal phases", *Nature* **1997**, *388*, 235–236.

[251] G. I. Waterhouse, M. R. Waterland, "Opal and inverse opal photonic crystals: Fabrication and characterization", *Polyhedron* **2007**, *26*, 356–368.

[252] T. E. Tiwald, J. A. Woollam, S. Zollner, J. Christiansen, R. B. Gregory, T. Wetteroth, S. R. Wilson, A. R. Powell, "Carrier concentration and lattice absorption in bulk and epitaxial silicon carbide determined using infrared ellipsometry", *Physical Review B* **1999**, *60*, 11464–11474.

[253] P. Colombo, R. Riedel, G. Soraru, H.-J. Kleebe, *Polymer Derived Ceramics: From Nano-Structure to Applications*, DEStech Publications, Inc, **2009**.

[254] S. Vowinkel, A. Boehm, T. Schäfer, T. Gutmann, E. Ionescu, M. Gallei, "Preceramic core-shell particles for the preparation of hybrid colloidal crystal films by melt-shear organization and conversion into porous ceramics", *Materials & Design* **2018**, *160*, 926–935.

[255] S. M. N. Al-Ajrash, C. Browning, R. Eckerle, L. Cao, "Innovative procedure for 3D printing of hybrid silicon carbide/carbon fiber nanocomposites", *Nano Select* **2021**, *2*, 2201–2208.

[256] R. C. Schroden, M. Al-Daous, C. F. Blanford, A. Stein, "Optical Properties of Inverse Opal Photonic Crystals", *Chemistry of Materials* **2002**, *14*, 3305–3315.

[257] Y. Qi, B. Xiang, J. Zhang, "Effect of titanium dioxide TiO_2 with different crystal forms and surface modifications on cooling property and surface wettability of cool roofing materials", *Solar Energy Materials and Solar Cells* **2017**, *172*, 34–43.

[258] Y. Zhao, C. Li, X. Liu, F. Gu, H. Jiang, W. Shao, L. Zhang, Y. He, "Synthesis and optical properties of TiO_2 nanoparticles", *Materials Letters* **2007**, *61*, 79–83.

[259] R. Vasita, D. S. Katti, "Nanofibers and their applications in tissue engineering", *International Journal of Nanomedicine* **2006**, *1*, 15–30.

[260] Kenry, C. T. Lim, "Nanofiber technology: current status and emerging developments", *Progress in Polymer Science* **2017**, *70*, 1–17.

[261] H. Kim, S. McSherry, B. Brown, A. Lenert, "Selectively Enhancing Solar Scattering for Direct Radiative Cooling through Control of Polymer Nanofiber Morphology", *ACS Applied Materials & Interfaces* **2020**, *12*, 43553–43559.

[262] J. Xue, T. Wu, Y. Dai, Y. Xia, "Electrospinning and Electrospun Nanofibers: Methods, Materials, and Applications", *Chemical Reviews* **2019**, *119*, 5298–5415.

[263] J. L. Daristotle, A. M. Behrens, A. D. Sandler, P. Kofinas, "A Review of the Fundamental Principles and Applications of Solution Blow Spinning", *ACS Applied Materials & Interfaces* **2016**, *8*, 34951–34963.

[264] G. C. Dias, T. S. P. Cellet, M. C. Santos, A. O. Sanches, L. F. Malmonge, "PVDF nanofibers obtained by solution blow spinning with use of a commercial airbrush", *Journal of Polymer Research* **2019**, *26*.

[265] A. M. C. Santos, E. L. G. Medeiros, J. J. Blaker, E. S. Medeiros, "Aqueous solution blow spinning of poly(vinyl alcohol) micro- and nanofibers", *Materials Letters* **2016**, *176*, 122–126.

[266] D. L. Costa, R. S. Leite, G. A. Neves, L. N. d. L. Santana, E. S. Medeiros, R. R. Menezes, "Synthesis of TiO_2 and ZnO nano and submicrometric fibers by solution blow spinning", *Materials Letters* **2016**, *183*, 109–113.

[267] E. Hofmann, M. Dulle, X. Liao, A. Greiner, S. Förster, "Controlling Polymer Microfiber Structure by Micro Solution Blow Spinning", *Macromolecular Chemistry and Physics* **2019**, *221*, 1900453.

[268] H. Y. Jeong, S.-C. An, Y. C. Jun, "Light activation of 3D-printed structures: from millimeter to sub-micrometer scale", *Nanophotonics* **2022**, *11*, 461–486.

[269]   E. Hofmann, K. Kruger, C. Haynl, T. Scheibel, M. Trebbin, S. Forster, "Microfluidic nozzle device for ultrafine fiber solution blow spinning with precise diameter control", *Lab on a Chip* **2018**, *18*, 2225–2234.

[270]   M. D. Calisir, A. Kilic, "A comparative study on SiO_2 nanofiber production via two novel non-electrospinning methods: Centrifugal spinning vs solution blowing", *Materials Letters* **2020**, *258*, 126751.

[271]   H. Wang, X. Zhang, N. Wang, Y. Li, X. Feng, Y. Huang, C. Zhao, Z. Liu, M. Fang, G. Ou, H. Gao, X. Li, H. Wu, "Ultralight, scalable, and high-temperatureresilient ceramic nanofiber sponges", *Science Advances* **2017**, *3*, e1603170.

[272]   C. Jia, Y. Liu, L. Li, J. Song, H. Wang, Z. Liu, Z. Li, B. Li, M. Fang, H. Wu, "A Foldable All-Ceramic Air Filter Paper with High Efficiency and High-Temperature Resistance", *Nano Letters* **2020**, *20*, 4993–5000.

[273]   X. Cheng, M. Chen, L. Wu, G. Gu, "Novel and Facile Method for the Preparation of Monodispersed Titania Hollow Spheres", *Langmuir* **2006**, *22*, 3858–3863.

[274]   Y. Meng, D. Gu, F. Zhang, Y. Shi, H. Yang, Z. Li, C. Yu, B. Tu, D. Zhao, "Ordered mesoporous polymers and homologous carbon frameworks: amphiphilic surfactant templating and direct transformation", *Angewandte Chemie International Edition* **2005**, *44*, 7053–7059.

Appendix

A.1 Silicon carbide particles
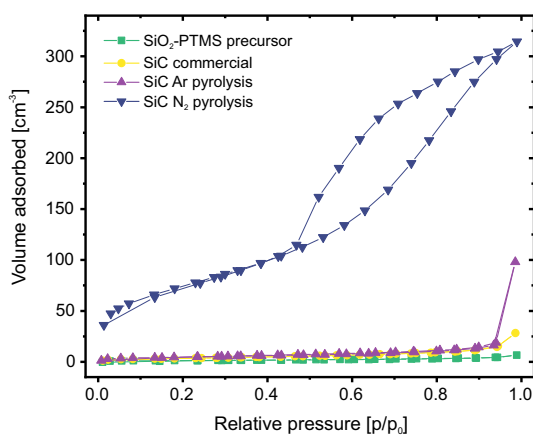
Figure A.1.: Nitrogen sorption measurements of the SiO$_2$-PTMS precursor, SiC commercial, SiC Ar pyrolysis and SiC N$_2$ pyrolysis. Except for the N$_2$ pyrolyzed sample all particles can be considered non-porous. The pyrolysis under N$_2$ conditions results in an appreciable surface area of $\sim 270 \, \mathrm{m^2 \, g^{-1}}$. This large surface area is likely to be caused by the conical pores between clustered particles and by PTMS-templated pores in the mesoporous range. Reprinted with permission from „Carbothermal synthesis of micron-sized, uniform, spherical silicon carbide (SiC) particles", by Feller, T.; Rosenfeldt, S.; Retsch, M. *Journal of Inorganic and General Chemistry* **2021**, *647*, 22, 2172-2180.

Acknowledgement

Colophon

This thesis was typeset with $\text{\LaTeX}\,2_\varepsilon$. It uses the *Clean Thesis* style developed by Ricardo Langner. The design of the *Clean Thesis* style is inspired by user guide documents from Apple Inc.

Download the *Clean Thesis* style at `http://cleanthesis.der-ric.de/`.

Versicherungen und Erklärungen

(§8 Satz 2 Nr. 3 PromO Fakultät)

Hiermit versichere ich eidesstattlich, dass ich die Arbeit selbstständig verfasst und keine anderen als die von mir angegebenen Quellen und Hilfsmittel benutzt habe (vgl. Art. 64 Abs. 1 Satz 6 BayHSchG).

(§8 Satz 2 Nr. 3 PromO Fakultät)

Hiermit erkläre ich, dass ich die Dissertation nicht bereits zur Erlangung eines akademischen Grades eingereicht habe und dass ich nicht bereits diese oder eine gleichartige Doktorprüfung endgültig nicht bestanden habe.

(§8 Satz 2 Nr. 4 PromO Fakultät)

Hiermit erkläre ich, dass ich Hilfe von gewerblichen Promotionsberatern bzw. -vermittlern oder ähnlichen Dienstleistern weder bisher in Anspruch genommen habe noch künftig in Anspruch nehmen werde.

(§8 Satz 2 Nr. 7 PromO Fakultät)

Hiermit erkläre ich mein Einverständnis, dass die elektronische Fassung der Dissertation unter Wahrung meiner Urheberrechte und des Datenschutzes einer gesonderten Überprüfung unterzogen werden kann.

(§8 Satz 2 Nr. 8 PromO Fakultät)

Hiermit erkläre ich mein Einverständnis, dass bei Verdacht wissenschaftlichen Fehlverhaltens Ermittlungen durch universitätsinterne Organe der wissenschaftlichen Selbstkontrolle stattfinden können.

Bayreuth, Datum

_____

Tanja Feller